Spring 5-31-2016

Oxidation kinetics of metallic powders

Hongqi Nie
New Jersey Institute of Technology

ABSTRACT

OXIDATION KINETICS OF METALLIC POWDERS

by
Hongqi Nie

Aluminum and magnesium are widely used in pyrotechnic formulations and other energetic materials; they are also common components of reactive alloys, e.g., Al-Mg and B-Mg, and others, which are potential fuels for explosives and propellants. Reaction mechanisms and oxidation kinetics of aluminum, magnesium and Al-Mg alloy powders in different oxidizing environments are investigated using thermo-analytical measurements. New methods of data processing are developed, relying on measured particle size distributions of the reactive spherical powders. It became possible to identify the reaction interface location for many heterogeneous metal oxidation processes; for several reactions, detailed kinetic descriptions are obtained.

For aluminum powders, location of the reaction interface is established for oxidation in steam and liquid water. Stage-wise oxidation behavior is observed and interpreted. The oxidation of aluminum covered by a thin natural oxide layer in oxygen occurring at relatively low temperatures is quantitatively characterized using different types of thermo-gravimetric (TG) measurements with increased amount of powder for greater sensitivity. Activation energy and the pre-exponent are determined as a function of reaction progress using isoconversion processing and assuming a diffusion-limited reaction mechanism. The reaction kinetics is also established for aluminum nanopowders. It is shown that the oxidation mechanism established for micron sized aluminum remains valid for particles as small as 10 nm. Aluminum oxidation model is combined with a heat

transfer model to describe ignition of aluminum particles exposed to a heated oxidizing environment.

For magnesium powders, their oxidation by both oxygen and steam was studied by thermo-analytical measurements for micron-sized powders. The location of reaction interface is identified using experiments with spherical powders with different but overlapping particle size distributions. The reaction is found to occur at the interface of metal and the growing oxide layer for all oxidizing conditions. Thus, the reaction is rate limited by diffusion of oxidizer to the metal surface. Reaction rates for low and elevated temperatures are quantified using heat flow calorimetry and TG measurements, respectively. Simplified diffusion-limited reaction models are developed for oxidation of magnesium in both oxygen and steam. The models enable one to predict both pre-ignition reactions and the time of Mg powder aging when exposed to moisture or oxygen at different temperatures.

Finally, the mechanisms of low-temperature, heterogeneous oxidation of differently prepared Al-Mg alloy powders in oxygen are studied using thermo-gravimetric measurements. Fully and partially oxidized samples are recovered and characterized using scanning electron microscopy and x-ray diffraction. Voids grow within oxidized alloy powders for both atomized and mechanically alloyed powders. Two oxidation stages are identified for both alloy powders. Both magnesium and aluminum are oxidized at first oxidation stage, producing MgO and amorphous alumina. Spinel $MgAl_2O_4$ is produced during the second stage. The reaction is found to occur at the internal surface of the oxide shell as determined by matching the oxidation dynamics for particles with the same size but belonging to powders with different particles size distributions. Apparent activation

energies for both oxidation stages are obtained as a function of the thickness of the growing oxide layer. The switchover between oxidation stages occurs when the spinel structure starts forming.

OXIDATION KINETICS OF METALLIC POWDERS

by
Hongqi Nie

A Dissertation
Submitted to the Faculty of
New Jersey Institute of Technology
in Partial Fulfillment of the Requirements for the Degree of
Doctor of Philosophy in Chemical Engineering

Otto H. York Department of
Chemical, Biological and Pharmaceutical Engineering

May 2016

.

APPROVAL PAGE
OXIDATION KINETICS OF METALLIC POWDERS

Hongqi Nie

Dr. Edward L. Dreizin, Dissertation Advisor — Date
Professor of Chemical, Biological, and Pharmaceutical Engineering, NJIT

Dr. Robert B. Barat, Committee Member — Date
Professor of Chemical, Biological, and Pharmaceutical Engineering, NJIT

Dr. Xianqing Wang, Committee Member — Date
Associate Professor of Chemical, Biological, and
Pharmaceutical Engineering, NJIT

Dr. Mirko Schoenitz, Committee Member — Date
Associate Research Professor of Chemical, Biological, and
Pharmaceutical Engineering, NJIT

Dr. Stephen Da-Yen Tse, Committee Member — Date
Professor of Mechanical and Aerospace Engineering, Rutgers University, NJ

BIOGRAPHICAL SKETCH

Author: Hongqi Nie

Degree: Doctor of Philosophy

Date: May 2016

Undergraduate and Graduate Education:

- Doctor of Philosophy in Chemical Engineering,
  New Jersey Institute of Technology, Newark, NJ, 2016
- Master of Science in Chemical Engineering,
  New Jersey Institute of Technology, Newark, NJ, 2011
- Bachelor of Science in Pharmaceutical Engineering,
  Wuhan University of Technology, Wuhan, P. R. China, 2009

Major: Chemical Engineering

Presentations and Publications:

Peer-Reviewed Journal Publications:

H. Nie, M. Schoenitz, E.L. Dreizin, Oxidation of differently prepared aluminum and magnesium alloys in oxygen, Journal of Alloys and Compounds, under review (2016).

A. Abraham, H. Nie, E.L. Dreizin, A.B. Vorozhtsov, M. Lerner, N. Rodkevich, Bimetal Al-Ni for Advanced Energetics, The Journal of Physical Chemistry C, under review (2016).

A.B. Vorozhtsov, M. Lerner, N. Rodkevich, H. Nie, A. Abraham, M. Schoenitz, E.L. Dreizin, Oxidation of nano-sized aluminum powder, Thermochimica Acta, under review (2016).

H. Nie, M. Schoenitz, E.L. Dreizin, Initial stages of oxidation of aluminum powder in oxygen, Journal of Thermal Analysis and Calorimetry, in press (2016).

H. Nie, M. Schoenitz, E.L. Dreizin, Oxidation of magnesium: implication for aging and ignition, Journal of Physical Chemistry C 120 (2016) 974-983.

H. Nie, S. Zhang, M. Schoenitz, E.L. Dreizin, Reaction interface between aluminum and water, International Journal of Hydrogen Energy 38 (2013) 11222-11232

A. Corcoran, S. Mercati, H. Nie, M. Milani, L. Montorsi, E.L. Dreizin, Combustion of fine aluminum and magnesium powders in water, Combustion and Flame 160 (2013) 2242-2250

H. Nie, M. Schoenitz, E.L. Dreizin, Calorimetric investigation of the aluminum-water reaction, International Journal of Hydrogen Energy 37 (2012) 11035-11045.

Presentations:

H. Nie, M. Schoenitz, E.L. Dreizin, Oxidation of differently prepared aluminum and magnesium alloys in oxygen, *2016 ESSCI Spring Meeting*, Princeton, NJ, March 8-13, 2016.

H. Nie, M. Schoenitz, E.L. Dreizin, Oxidation of differently prepared aluminum and magnesium alloys in oxygen, *AIChE Annual Meeting*, Salt Lake City, UT, November 12, 2015.

H. Nie, M. Schoenitz, E.L. Dreizin, Oxidation of magnesium: implication for aging and ignition, *AIChE Annual Meeting*, Atlanta, GA, November 21, 2014.

H. Nie, M. Schoenitz, E.L. Dreizin, Initial stages of oxidation of aluminum powder in oxygen, *AIChE Annual Meeting*, Atlanta, GA, November 21, 2014.

H. Nie, M. Schoenitz, E.L. Dreizin, Oxidation of magnesium: implication for aging and ignition, *Gordon Research Seminar and Conference*, Sunday River resort, ME, June 13-21, 2014.

H. Nie, S. Zhang, M. Schoenitz, E.L. Dreizin, On mechanism of split water by its reaction with aluminum and magnesium, *AIChE Annual Meeting*, San Francisco, CA, November 5-7, 2013.

H. Nie, M. Schoenitz, E.L. Dreizin, Effect of particle size on hydrogen production by reaction of liquid water and aluminum powders, *AIChE Annual Meeting*, Pittsburgh, PA. October 2012.

H. Nie, M. Schoenitz, E.L. Dreizin, Calorimetric investigation of the aluminum-water reaction, *Gordon Research Conference*, West Dover, VT, June 2012.

This dissertation is dedicated to my beloved parents,
My wife, Stacy; my son, Jaden.
Thank you and love you all forever!

ACKNOWLEDGMENT

Praise the Lord! It is amazing and unbelievable that I become to be a real Dr. Nie. However, I certainly know that I definitely couldn't reach my goal alone without any support and help given from you guys.

Firstly, I would like to express my deepest gratitude to my advisor, Dr. Edward L. Dreizin, who is knowledgeable, optimistic, humorous and considerate. He constantly gives me support and encouragement, even though I always complain to him about difficulties in my projects. He is not only an advisor with an open mind to listen in my research, but also the one providing me a whole picture in my future career. Under his guidance and influence, I was always attracted to discover the unknowns and feeling exited when something is explored to be interesting.

Secondly, I would like to appreciate my co-advisor, Dr. Mirko Schoenitz, for his constructive criticism to my work and genuine assistance through my research experience. Whenever you need help from him, he was always right behind of you. As a fantastic mentor, he always instructs and teaches me with enough patience and tells me the trick that is really useful to solve problems.

Special thanks to Dr. Robert B. Barat, Dr. Xianqing Wang and Dr. Stephen Tse, who serve as my PhD dissertation committee, for their useful and helpful suggestions from various academic backgrounds and valuable time.

I would like to recognize all the co-workers in the research group. It was so pleasure to work with current students: Ani Abraham, Song Wang, Kerri-Lee Chintersingh, Ian Monk and Xinhang Liu. Special appreciation needs to give to the senior students who providing me an idea to work it out at beginning of my research life: Shasha

Zhang, Yasmine Aly, Shashank Vummidi, Rayon Williams and Priya Santhanam. In addition, I like to thank two undergraduate students, Hari Ravichandran and Danielle Quijano, for working with me on their independent studies related to my dissertation; and a master student, Siva Kumar Valluri, who helped me to perform multiple TG experiments and conduct data processing. I also like to acknowledge the people who visit our group and worked with me on collaborating projects, Stefano Mercati, Professor Zou Meishuai and Yao Wang.

Special thanks to Ms. Gonzalez-Lenahan and Dr. Ziavras from the Graduate Studies office at NJIT for their valuable contributions in preparing my thesis document and making it in a better looking of manuscript.

Personally, I feel lucky to have the infinite love from my parents, Gang Nie and Shuping Dong and my wife, Wenjing Liu, especially. She is so pivotal in every success I have made. She has sacrificed so much for me and supported me without any doubt. Without my family's unconditional love and support, I definitely will not achieve this goal in my life. I greatly appreciate everything you have done for me and sacrificed for me.

Lastly, I really appreciate our project sponsor, Defense Threat Reduction Agency (DTRA), for the financial support on my various projects and conferences I attended.

TABLE OF CONTENTS

TABLE OF CONTENTS
(Continued)

Chapter **Page**

TABLE OF CONTENTS
(Continued)

TABLE OF CONTENTS
(Continued)

LIST OF TABLES

LIST OF FIGURES

LIST OF FIGURES
(Continued)

LIST OF FIGURES
(Continued)

LIST OF FIGURES
(Continued)

LIST OF FIGURES
(Continued)

LIST OF FIGURES
(Continued)

LIST OF FIGURES
(Continued)

LIST OF FIGURES
(Continued)

LIST OF FIGURES
(Continued)

CHAPTER 1

INTRODUCTION

1.1 Background

Aluminum and magnesium are widely used in pyrotechnics as well as in other energetic formulations due to their high combustion enthalpy and high energy density [1-7]. They are also components of reactive alloys, e.g., Al-Mg [8-12] and B-Mg [13, 14], which are potential fuels for explosives, propellants, and pyrotechnics.

Aluminum-magnesium alloys have also been explored recently as components of oxygen generators [15] and as materials capable of reacting with water in a wide range of temperatures for hydrogen production [16, 17]. Metal-assisted water split reactions producing hydrogen are explored for a variety of applications, from in-situ operated fuel cells [18, 19] to fueling automobiles[20], to propulsion of underwater vehicles [21-24].

1.2 Challenge

For aluminum powder as a reactive material, one of the advantages is its long-term stability ensured by protective properties of the naturally formed surface alumina film. However, a delayed ignition caused by the diffusion resistance of the same alumina film often becomes a bottleneck to the overall burn rate of aluminum particles. Predicting this ignition delay for different conditions and for powders with different particle size distributions (PSDs) is important for proper design of energetic systems employing aluminum powders. Despite recent progress in understanding aluminum oxidation processes [25-31], substantial uncertainties remain for the rates of low-temperature oxidation, controlled by diffusion of reactants through very thin, naturally grown oxide films. Because of its relatively low rate,

this process affects the ignition delays significantly; yet, it is the most difficult process to quantify experimentally. Low-temperature reactions become particularly important for finer powders and nano-powders, for which an even relatively slow oxidation causes substantial heat release because of the high specific surface area.

For magnesium, it is well-known that powders are prone to aging because magnesium oxide layer is not as protective as alumina. In particular, in humid environments the powders are known to age rapidly; however, we were unable to find references describing this aging quantitatively. Although multiple approaches have been reported to alleviate the aging, using various coatings [32, 33], kinetics of oxidation of Mg powders at low temperature are not well quantified. Surprisingly little work can be found in the literature investigating the mechanisms of Mg oxidation [34]. In part, this can be explained by high volatility of Mg making it difficult to separate heterogeneous and vapor phase reactions and quantify individual oxidation processes.

Recently, there was interest in alloys involving Mg, such as Al·Mg alloys prepared by mechanical milling and useful as components of advanced energetics [35-38]. Oxidation of Al·Mg alloys prepared from the respective binary melts is also of significant interest [39, 40]. The oxidation and combustion behaviors of metastable mechanically alloyed powders in the Al-Mg binary system with varied compositions have been investigated in the context of high-energy density materials [36, 37, 41]. However, the mechanistic understanding of such oxidation processes is lacking and should rely on clearly delineated mechanisms for oxidation of individual component metals.

1.3 Objective

In this work, the focus is on characterization of detailed mechanisms of oxidation of aluminum, magnesium, and their alloys. Both dry and humid oxidizing environments are considered. For each material and for each oxidizing environment, the overarching objectives are:

- Identify the location of the interface where the heterogeneous reaction occurs
- Determine the reaction rate at different temperatures, and for different thicknesses of the growing oxide layer
- Describe the reaction kinetics quantitatively, accounting for the effects of particle size distribution, temperature, and thickness of the produced oxide.

It was further desired to determine whether the oxidation mechanism established for coarse aluminum powders is changing when the particle sizes are reduced to tens or hundreds of nanometers. Finally, it was of interest to correlate the mechanisms of oxidation of pure metals with those of the respective alloys.

In addition, it was important to establish the correlations between specific oxidation mechanisms and processes governing aging and ignition of different powders of metals and alloys. The methodology and data processing techniques developed in this research are expected to be useful for analysis of oxidation and similar reactions for a broad range of powder-like materials.

CHAPTER 2

CALORIMETRIC INVESTIGATION OF ALUMINUM-WATER REACTION

2.1 Abstract

The aluminum-water split reaction is characterized experimentally using micro-calorimetry. The rates of heat release during the reaction at two fixed temperatures, 303 and 313 K were measured for spherical aluminum powders placed in liquid water. Fully and partially reacted powders were characterized using electron microscopy and x-ray diffraction. Experiments were performed with three commercial powders with nominal sizes of 3-4.5, 10-14, and 17-30 μm. The only crystalline reaction product detected was bayerite. Initially, particles grow bayerite layers which later sinter together forming continuous aluminum-bayerite composites. The observed reaction could be broken down into several parts, including an induction time, two stages of relatively rapid reaction, and reaction termination. The significance of the first of the rapid reaction stages increased for experiments at the higher temperature. The finer powders exhibited faster and more complete reaction. Experimental data were processed using a simplified kinetic model reported in the literature to assess the diffusion coefficient describing the reaction rate-limiting process: transport of hydroxo complexes of aluminum through a growing porous layer of bayerite. The calculated diffusion coefficient was in the range expected for the experimental temperatures; however, its changes as a function of the powder particle size and as a function of the reaction time indicate that the current model is inadequate for describing the present experiments.

2.2 Introduction

Hydrogen continues to be of interest for environmentally friendly energy storage and delivery for a multitude of applications [42-44]. Fuel cells that use hydrogen as a fuel replacement for portable power generation have been developed for decades and by themselves are economically viable [45-47]. The greatest challenges to widespread adaptation of hydrogen as a fuel are the lack of infrastructure, and the problems arising from hydrogen storage. One possible method to deliver hydrogen to a fuel cell is its *in-situ* generation via a water split reaction, where a metal reacts with water to form hydrogen gas and the corresponding metal oxide or hydroxide. Many metals or alloys are suitable for this process; current research is most active on aluminum-water reactions [48-53]:

$$Al+3H_2O \rightarrow Al(OH)_3 + 1.5H_2 \uparrow \qquad \text{(R1)}$$

These particular reaction (R1) is thermodynamically favored, it yields environmentally benign condensed products, and it has been recently shown to be economically attractive for pollution-free energy-generating technologies [21, 22]. However, the mechanisms affecting the reaction rates remain poorly understood. A protective natural surface layer of alumina is known to inhibit the aluminum-water reaction at low temperatures, and a number of investigations focused on the removal of this protective layer [50, 51, 54-57]. Recently, it has been discussed how the particle size of aluminum powder affects the rate of Al-water reaction [58]; however, the specific reasons causing fine particles to be more reactive than coarse ones remain elusive. A model proposed by Deng et al. [53, 59] discusses formation of hydrogen bubbles between

aluminum and the oxide layer, which are said to disrupt the oxide layer; however, to account for the observed differences in reaction rates for powders of different sizes (varied ca. from 1 to 100 μm) [58], the tangential component of the strain developed in the oxide layer must be non-negligible. Therefore, the bubbles must be comparable in size to the dimensions of the respective particles, which is highly unlikely. In most published experimental studies, the rate of Al-water reaction is monitored by tracking the amount of released hydrogen. Identification of kinetic trends from such measurements is difficult and changes in reaction rates can remain unnoticed or poorly resolved. Conversely, measuring the heat release associated with the reaction using contemporary calorimetric techniques is possible with high resolution. The objective of this study is to characterize Al-water reaction using calorimetry and identify kinetic trends defining the reaction rate.

2.3 Experimental

Spherical aluminum powders from Alfa Aesar with nominal particle sizes 3-4.5 μm, 10-14 μm, and 17-30 μm were used. Purities as reported by the supplier were 97.5 %, 98 %, and 99 %, respectively. The actual particle size distributions for these powders were measured using a Beckman-Coulter LS230 Enhanced Particle Analyzer and are shown in Figure 2.1. Respective volumetric average particle sizes are 7.2, 21.5, and 38.5 μm.

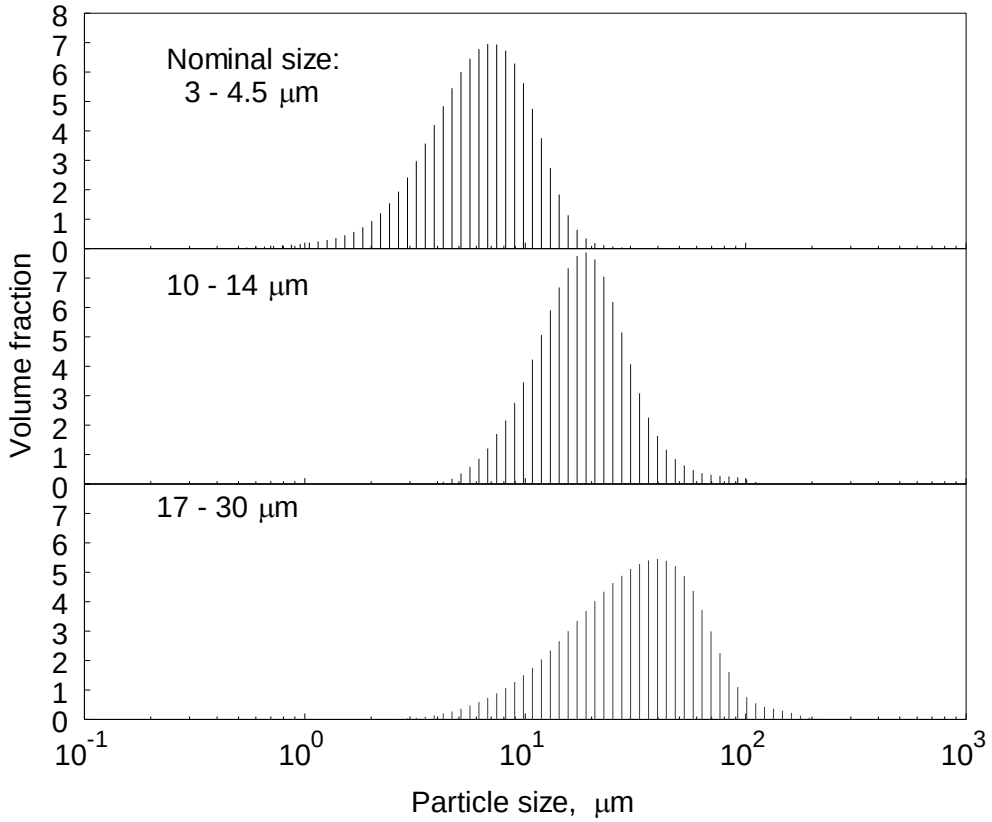

Figure 2.1 Particle size distributions for the spherical aluminum powders used in this study.

Heat flow calorimetry at constant temperature was carried out in a TA Instruments TAM III microcalorimeter. Measurements were performed using a perfusion ampoule by TA Instruments installed in a minicalorimeter. The perfusion ampoule enables calorimetric measurements for the samples subjected to a controlled gas flow or vented to the surroundings. Calibration of the minicalorimeter was carried out by passing a known current through an internal heating element and recording the response.

Measurements were carried out at 303 and 313 K (30 and 40 °C, respectively). Samples were contained in 4-mL reaction vessels. Both, stainless steel and glass vessels were used. Samples were loaded according to the following procedure: Al powder was

weighed and placed in the reaction vessel. Then, an approximate volume of distilled water was added to the reaction vessel, and weighed to determine the exact amount. Some of the samples were briefly stirred into the water with a small wooden dowel, taking care not to remove any powder from the reaction vessel. The reaction vessel was then attached to the perfusion ampoule, and the perfusion ampoule was inserted into the minicalorimeter. The time between first contact of Al powder and water, and the insertion into the calorimeter was always between five and ten minutes. For the insertion, the procedure suggested by the TAM III manufacturer was followed (stepwise insertion, 5-10 minute waiting periods) in order to not overly perturb the calorimeter signal. After insertion, the calorimeter signal was allowed to recover, and was considered correct after approximately 45 minutes. The perfusion ampoule was flushed with a regulated air flow at 50 mL/h. Hydrogen produced as a result of reaction was carried out together with the passing air.

Ideally initial and final baselines without samples loaded should be recorded to account for any baseline drift during the measurement. However, this was not feasible for the present tests. A meaningful baseline should be recorded with a reaction vessel containing water, but no aluminum. However, the exact location of the baseline is sensitive to the amount of water in the reaction vessel. With the available equipment it was not possible to reliably load water with an accuracy better than ~ 0.1 mL, and any baseline differences before and after an experiment would have been due to this uncertainty more than due to a true baseline drift. Simultaneously, a separate minicalorimeter idling in the same TAM III device during these measurements showed essentially no drift over weeks in comparison to the measurements. Therefore, the baseline for the current measurements was always assumed to be without drift.

Measurement times ranged from hours to days. Several fully and partially reacted samples were recovered for subsequent analysis by electron microscopy (SEM) and x-ray diffraction (XRD). To meaningfully arrest the reaction of partially reacted samples, the recovered material was placed in a vacuum chamber at room temperature, and dried for 30 minutes. Samples were prepared for microscopy by embedding in epoxy and grinding with SiC polishing paper up to 1200 grit. To avoid altering the embedded material, no further polishing step was performed. A Phenom Tabletop Microscope by FEI Technologies Inc., (an SEM with backscattered electron detector) was used for imaging. For XRD analysis, a Phillips X'Pert diffractometer with unfiltered Cu-Kα radiation was used. Samples were either ground in an alumina mortar and then deposited on a low-background quartz plate, or deposited on the quartz plate directly if the material was not agglomerated.

2.4 Results

A characteristic pattern of heat release for Al reacting with liquid water is shown in Figure 2.2. After an initial induction period, the main reaction proceeds in stages. The two stages visible in Figure 2.2 can be more or less pronounced. The reproducibility of the recorded heat flow patterns was lower than expected and multiple experiments were performed to assess the effects of mass of the powder sample, mass of water, initial stirring of the loaded powder, air flow through and material of the reaction vessel.

To systematically evaluate different experimental conditions, characteristic times were defined. For consistency, induction period is defined as the time elapsed between the first contact between aluminum and water and the time the heat flow reached 1 % of its maximum value. Further, the times τ_1 and τ_2 were defined as the times between the end of

the induction period and the heat flow peak maxima of the first and second stages, respectively. As alluded to in the experimental section, there is a 5-min uncertainty associated with all reported times. However, this is acceptable since times generally measure in multiple hours.

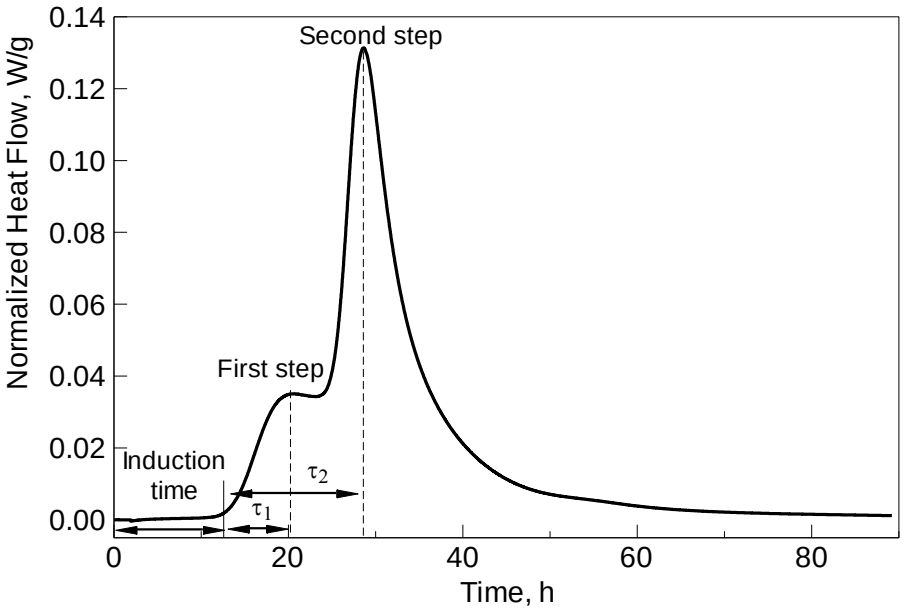

Figure 2.2 Normalized heat flow measured for 3-4.5 μm aluminum powder reacting with water at 303 K (30 °C).

After the main reaction stages, the reaction rates slowed significantly, and waiting for the reactions to complete was not practical. Therefore the measured enthalpies are expected to be less than the enthalpy of complete reaction and the degree of conversion less than one. To evaluate the conversion completeness, the enthalpies were put in relation to the theoretical reaction enthalpy. Reference data for bayerite are scarce, and not included in many standard self-consistent thermodynamic databases, the enthalpy of formation of the gibbsite polymorph of $Al(OH)_3$ is available, however ($\Delta H_{f,298}$ = –1293.1 kJ/mol [60]). The difference between the enthalpies of formation of bayerite and gibbsite is about 5

kJ/mol according to an estimate in Reference [61]. This amounts to a difference of about 1.2 % for the enthalpy of the complete conversion.

Given the approximate nature of the present enthalpy measurements, this difference does not affect the validity of any observations, and the gibbsite polymorph was therefore chosen as reference.

All times, experimental reaction enthalpies, and degrees of reaction are summarized in Table 2.1. In addition to the effects of temperature and particle size, other experimental details were considered as potentially influencing the observed results. The material of the reaction vessel could have an influence since aluminum has the potential to reduce the protective oxide layer on the surface of the stainless steel vessel. However, no systematic differences were observed between experiments using a stainless steel reaction vessel and a glass reaction vessel. Therefore, the material of the reaction vessel was regarded as insignificant. Further, most aluminum-water suspensions were briefly stirred at the time of loading as described in the Experimental section. However, in some early experiments this step was omitted. This factor, too, was not observed to have a systematic influence on the reaction behavior, and was therefore not further considered. Finally, no systematic trends were observed for either amounts of Al and water. In summary, no unambiguous effects of stirring, sample or water mass, air flow and reaction vessel material could be identified. Therefore, these parameters will not be discussed further.

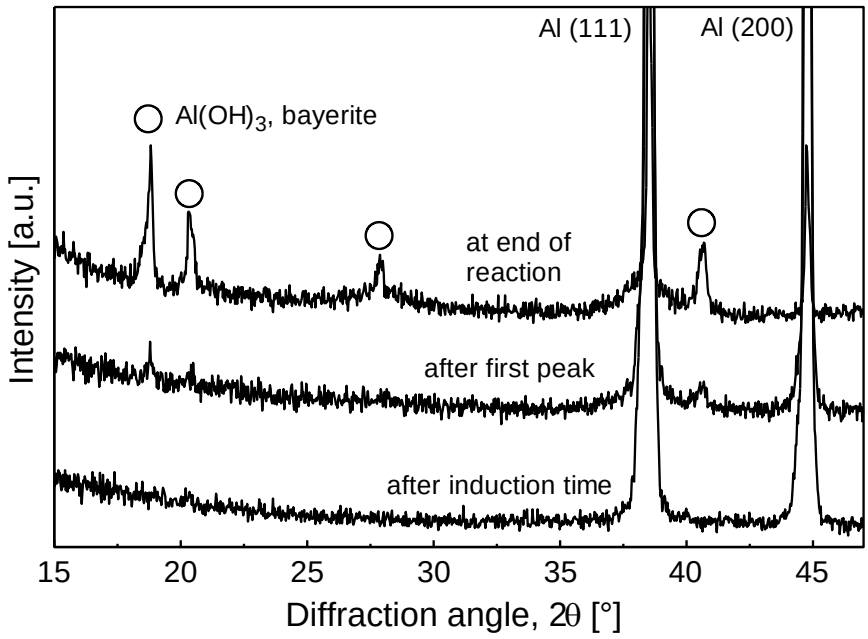

Figure 2.3 XRD patterns of samples recovered at different stages of the reaction at 303 K.

Figure 2.3 shows XRD patterns of materials recovered after the induction period, after the first heat flow peak, and at the end of the measurement, respectively. No reaction product was detected after the induction period, and the only product at later stages is crystalline bayerite. Amorphous reaction products cannot be ruled out, but the relatively low background suggests they are not prominent.

Table 2.1 Summary of Experiments

Run #	T, K	Nominal Particle Size, µm	Powder Mass, mg	Water Mass, g	Stir	Air Flow 50ml/h	Intro-duction time, min	Time to 1st peak, min	Time to 2nd peak, min	Reaction Heat, kJ/g	Est. Reaction Complete-ness*
4	303	3-4.5	20.2	2.18	No	No	650	320	595	5.98	0.37
20			20.7	2.05	No	Yes	445	390	820	14.96	0.93
19			21.0	2.00	Yes	Yes	500	390	735	12.52	0.78
1			83.2	2.18	No	No	340	240	750	8.24	0.51
2		10-14	34.0	1.89	No	No	840	340	840	5.98	0.37
6			80.1	2.12	Yes	No	2990	290	675	5.58	0.35
5			149.0	2.04	No	No	1035	205	550	4.87	0.30
3		17-30	7.0	2.00	No	No	2160	918	2188	8.60	0.53
11	313	3-4.5	5.0	1.89	Yes	Yes	555	70	575	14.97	0.93
13			5.1	0.51	Yes	Yes	198	125	360	9.02	0.56
17			5.1	1.50	Yes	Yes	210	145	315	13.99	0.87
14			5.2	1.02	Yes	Yes	645	95	N/A	8.39	0.52
7			19.4	2.01	Yes	Yes	140	80	160	11.15	0.69
21			20.4	2.05	No	Yes	90	98	120	9.68	0.60
10			21.4	2.05	Yes	Yes	185	75	300	10.24	0.63
G1*			20.3	1.99	Yes	Yes	102	105	416	8.95	0.55
G2*			5.1	2.05	Yes	Yes	125	122	N/A	15.37	0.95
16			22.3	1.93	Yes	Yes	194	Samples recovered for examination following induction period			
15			500	2.03	Yes	Yes	72				
18		10-14	20.1	2.01	Yes	Yes	240	120	265	4.69	0.29
8			20.4	2.07	Yes	Yes	350	100	705	7.36	0.46
12		17-30	21.0	2.18	Yes	Yes	520	495	1350	7.36	0.46
9			21.3	2.11	Yes	Yes	520	265	1105	1.97	0.31

* Completeness estimated using enthalpy of formation of gibbsite at room temperature.
* G1: Glass 1; G2: Glass 2

Figures 2.4 – 2.8 show backscattered electron images of the starting material, and of partially reacted materials. The images in Figure 2.4 illustrate the size distribution of one of the starting materials, and that the particle shape is approximately spherical.

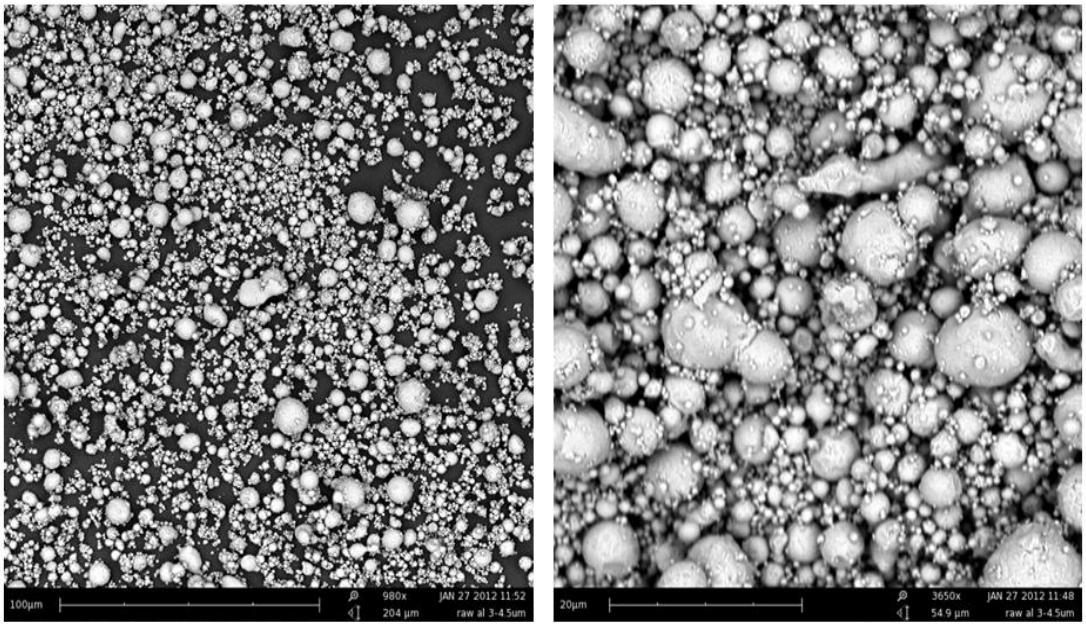

Figure 2.4 Starting material, 3-4.5 µm nominal particle size.

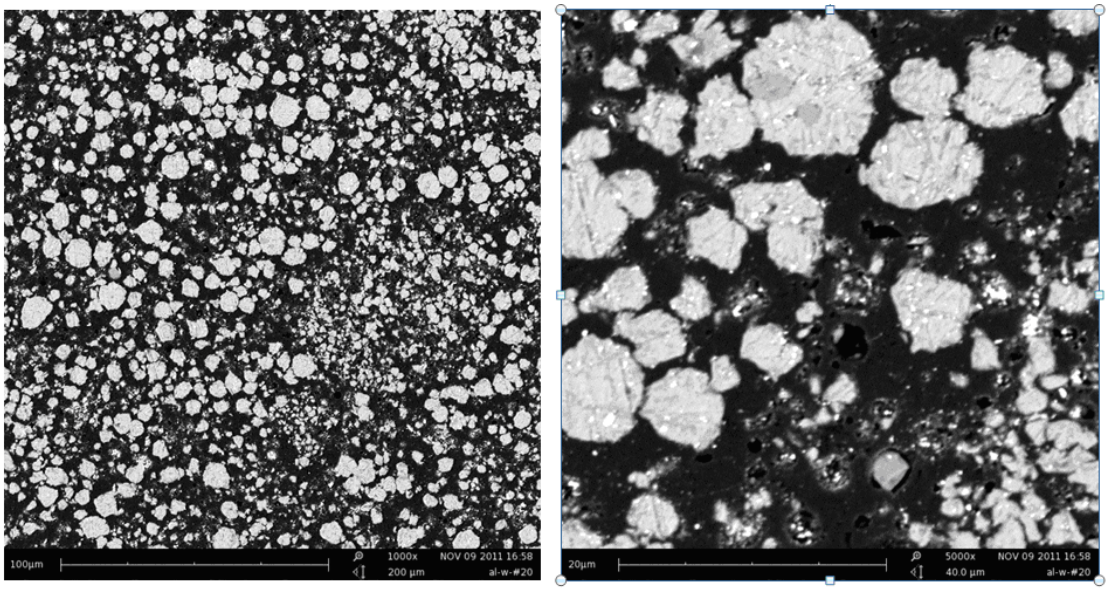

Figure 2.5 Al 3-4.5 µm, recovered after the induction period at 313 K (40 °C.).

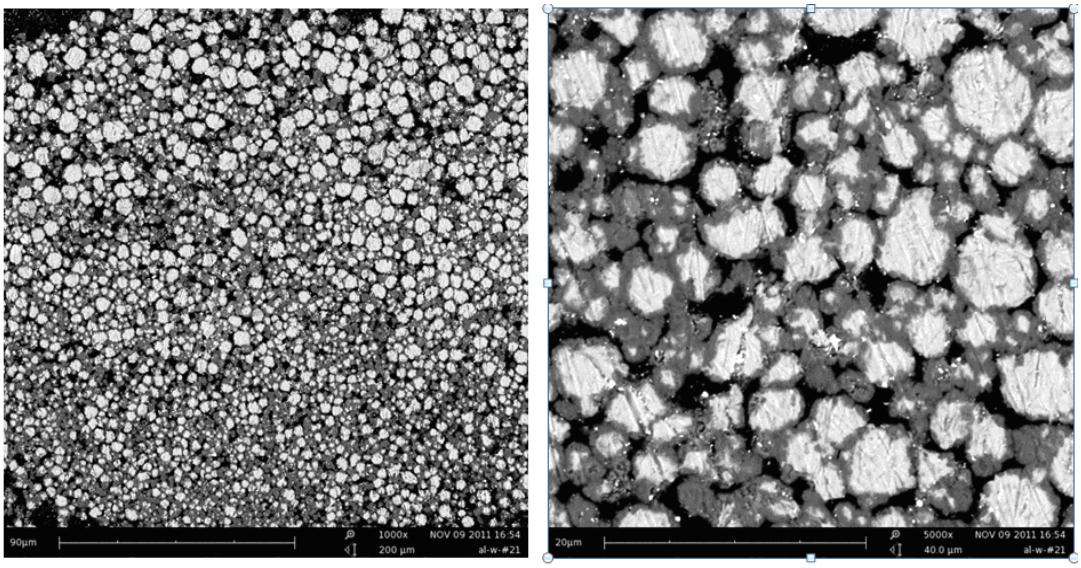

Figure 2.6 Al 3-4.5 µm, recovered after the first heat flow peak at 313 K (40 °C.).

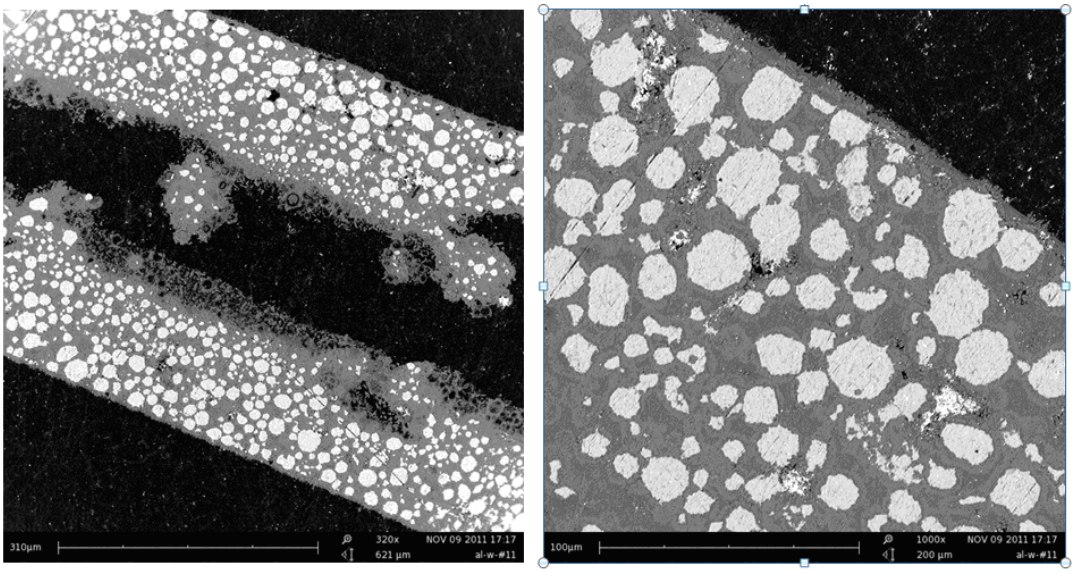

Figure 2.7 Al 3-4.5 µm at 313 K (40 °C), recovered after the reaction rate had slowed significantly, at 1300 min.

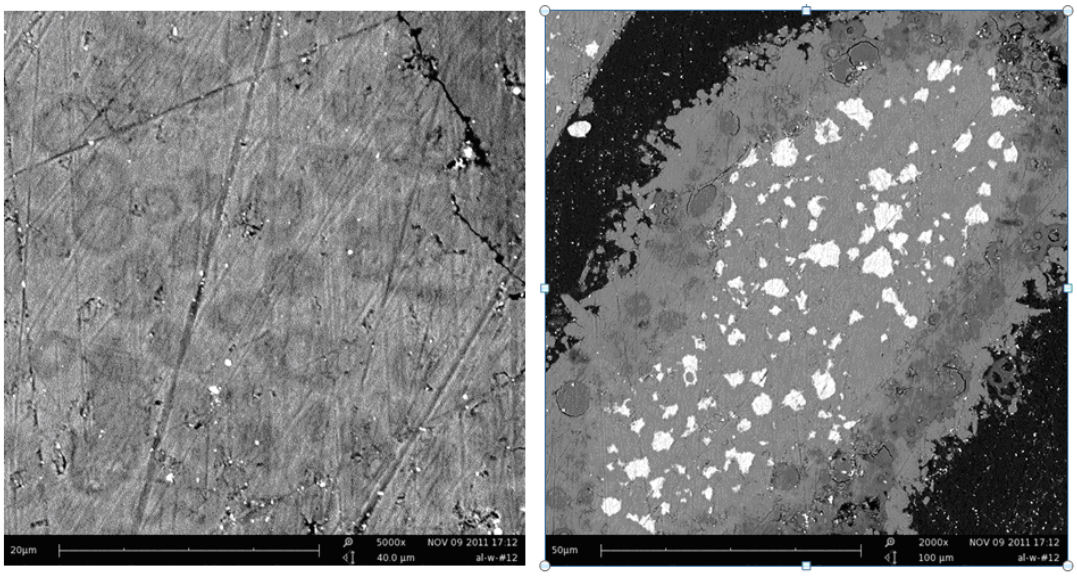

Figure 2.8 Al 10-14 µm at 313 K (40 °C), recovered after the reaction rate had slowed significantly, at 2680 min

To investigate the growth of the bayerite scale, samples were recovered after the induction period, after the first heat flow peak, and at the end of the measurement, after the reaction had slowed significantly. Figure 2.5 shows that at the onset of the first reaction stage, after the induction period, the particle shape has changed slightly, although no grown surface layer can be seen. Particles do show significant surface layers of bayerite after the first reaction step in Figure 2.6. Further, particles deviate more from the initial spherical shape, and the bayerite surface layers start to form bridges between particles. At the end of the measurement, shown in Figure 2.7, bayerite forms a continuous matrix with inclusions of remaining, unreacted aluminum. The magnified view on the right hand side of Figure 2.7 shows a brightness contrast within the bayerite matrix. This effect is seen even more strongly in Figure 2.8, in a 10-14 µm Al sample recovered at the end of the measurement. The fragment shown on the right, containing unreacted aluminum metal at its core shows an irregular outline and spherical inclusions with lower brightness near its

perimeter. XRD analysis shows no presence of any product phase other than bayerite, so the phase contrast must be the result of nanometer-scaled porosity. This suggests that a first generation of dense bayerite cemented the aluminum particles together, while a slower reaction continued to consume the aluminum metal while also dissolving and recrystallizing existing bayerite, forming a more porous second generation.

As noted above, all characteristic reaction times, including the induction period, are poorly reproducible and vary widely. Nevertheless, some qualitative trends can be identified, as illustrated in the following figures.

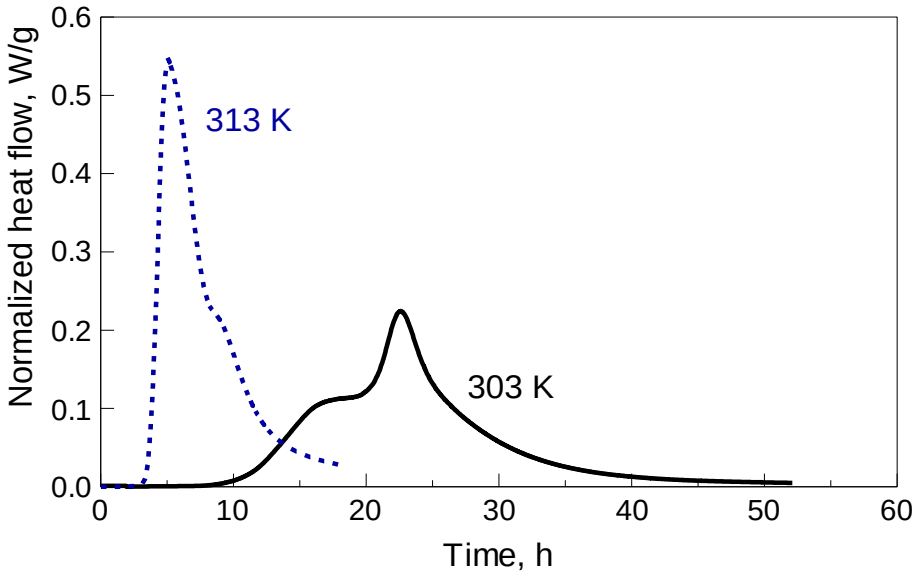

Figure 2.9 Normalized heat flow of the reaction of 3 – 4.5 µm aluminum with water at two different temperatures, 303 and 313 K. Runs#4 and #10; cf. Table 2.1.

Figure 2.9 shows heat flow curves recorded for 10-14 µm Al in water at 303 and 313 K, demonstrating the effect of temperature on the reaction. As may be expected for a non-equilibrium process, all aspects of the reaction occur earlier at the higher temperature. However, the reactions also differ qualitatively. At 313 K, the separation between first and

second reaction steps is much less pronounced, and the second reaction step is weaker relative to the first – the opposite from the behavior observed at 303 K.

Figures 2.10-2.13 show the effects of particle size. Figure 2.10 shows the heat flow curves recorded at 303 K for the three different starting materials. Larger particles consistently show lower reaction rates in all stages of the reaction. Further, as the particle size increases, the first stage of the reaction becomes more prominent relative to the second stage, and the separation between the stages increases as well. Figure 2.11 summarizes the effect of particle size on the induction time. Within the resolution of the observed trends, it can be stated that the induction time varies more strongly with average particle size at 303 K than at 313 K, although those trends are poorly constrained. Figure 2.12 shows corresponding plots for τ_1 and τ_2, the times to the first and second heat flow peaks, respectively. Both indicators show a much weaker dependence on the particle size. Only for the largest particles are slightly longer times observed.

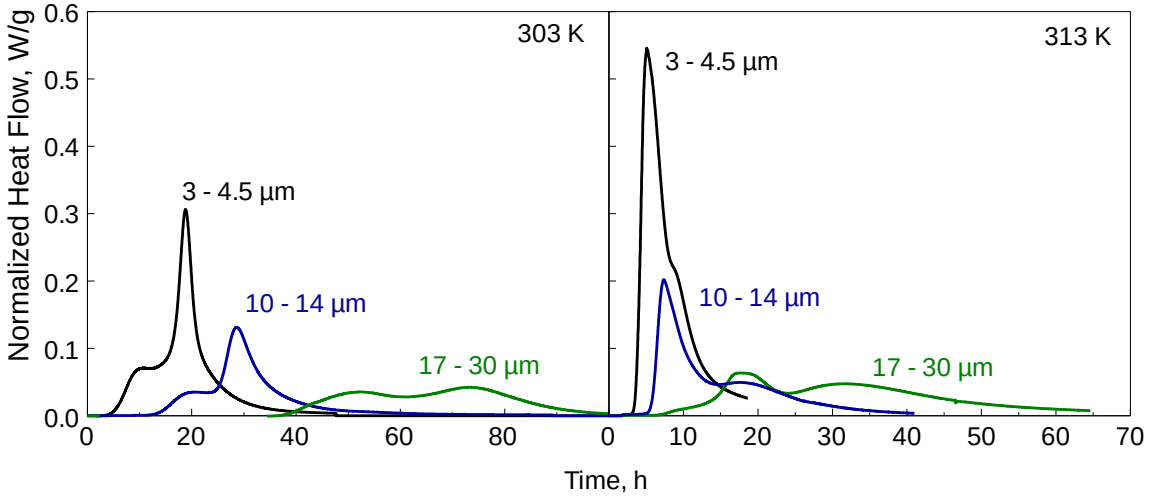

Figure 2.10 Normalized heat flows for the aluminum powders with different particle sizes reacting with water at different temperatures: left – 303 K, and right – 313 K. Runs #1, 2 and 3 are shown on the left, and runs # 7, 8 and 9 are shown on the right.

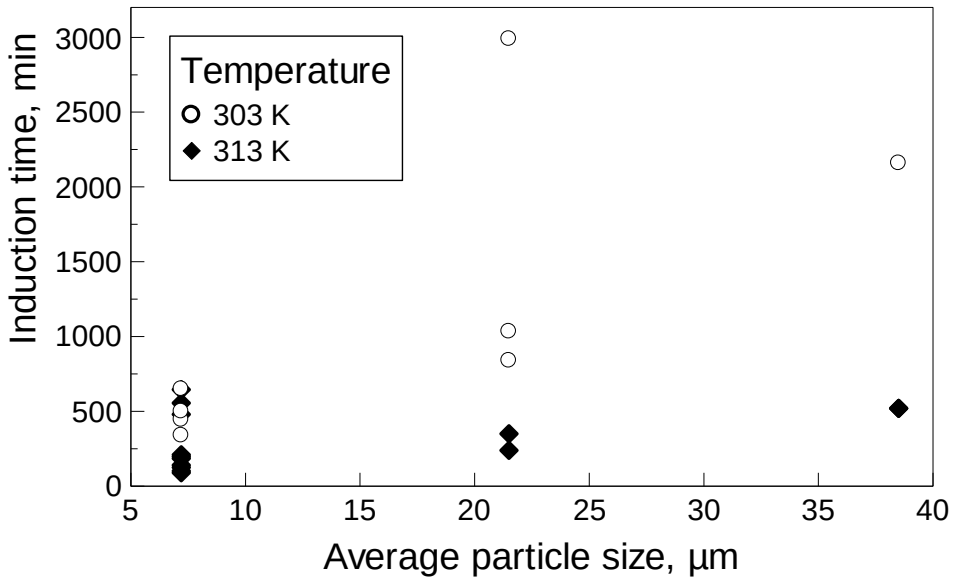

Figure 2.11 Induction times as a function of particle size.

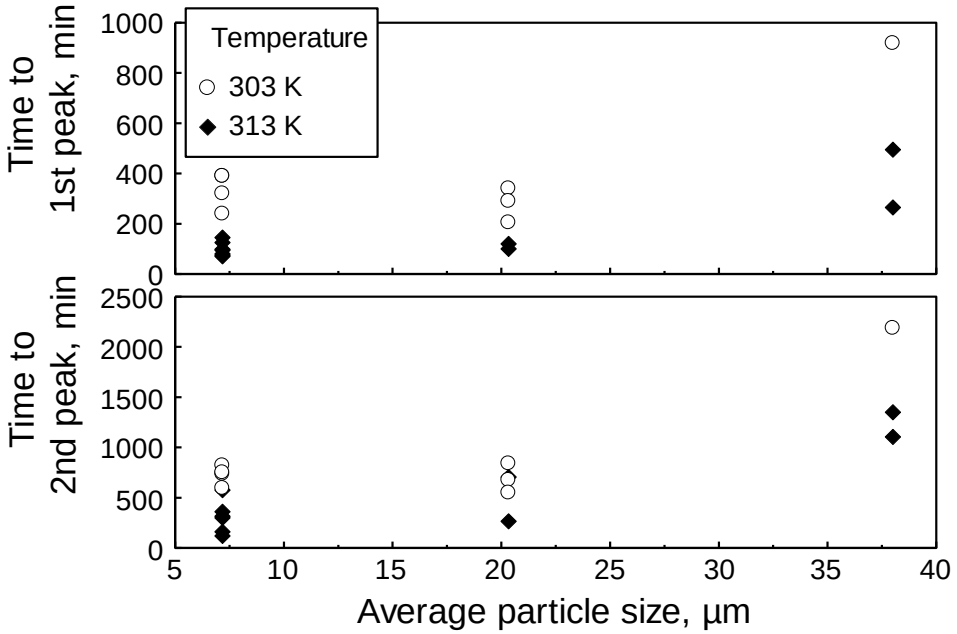

Figure 2.12 Times to the first and second exothermic peaks as functions of particle sizes.

Normalized heat of reaction as a function of the particle size is shown in Figure 2.13. The reaction tends to be more complete for finer powders at both temperatures. For

the finest powder, higher heats of reactions are observed at 313 K, however, the spread between the points is very wide. The effect of temperature on the reaction heat is less pronounced for coarser powders.

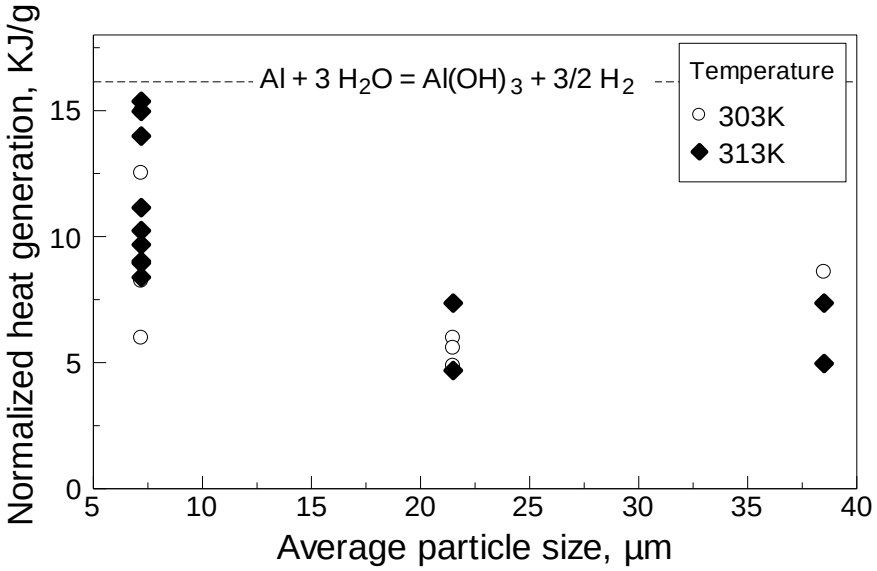

Figure 2.13 Normalized heat of reaction as a function of particle sizes. A dashed line shows the heat generation for the complete reaction.

2.5 Discussion

For the purpose of the following discussion, the reaction will be divided into a set of stages encountered in all measurements. Reactions start with an induction period, after which a period of relatively fast reaction is observed. All measurements also show extended periods of decreased reaction rates that gradually terminate the reaction.

2.5.1 Induction Time

Aluminum, once exposed to ambient conditions forms a 2-3 nm thick protective coating of amorphous oxide [25, 62]. Before the reaction between water and aluminum can take place, this protective coating must be sufficiently compromised. This process likely involves the reaction of the amorphous alumina to form hydrated products whether these are bayerite or other intermediates. Following earlier work [63], in Reference [64] it is suggested that amorphous alumina forms an amorphous hydrated gel as the first product of hydration. The hydration rates observed in Reference [64] at 298 K and 323 K are compatible with the induction periods observed in the present study. The hydration reaction is exothermic, but much less so than reaction (R1). As the initial hydrated products form, the amorphous oxide layer likely becomes pitted and porous.

2.5.2 Fast Reaction

In the geometry of the measurements, particles form a loosely packed layer at the bottom of the reaction vessel. However, as Figures 2.6 and 2.7 show, inter-particle contact is not extensive, and particles can be considered individually. Previous research considered the formation of bayerite layers on the surface of aluminum particles in the context of the preparation of metal-ceramic composite materials [65]. It was suggested that the rate limiting process for the growth of a bayerite surface layer is the diffusion of the $Al(OH)_4^-$ complex in the liquid phase. With this assumption, a simplified reaction rate model was developed and the reaction was described as:

$$\alpha^2 = \frac{2.24\rho_b^2 \upsilon D C_1 \sigma S_b V_b}{RT\rho_t^2 r^2} t \qquad (2.1)$$

where the reaction completeness, α, was defined through the mass difference between the bayerite formed and aluminum consumed, Δm, related to the final mass difference when the entire particle is reacted, $\Delta m_{complete}$.

$$\alpha = \frac{\Delta m}{\Delta m_{complete}} \tag{2.2}$$

Other parameters in Equation (2.1) and their respective values assigned following Reference [65] are:

ρ_b =2.42·10^3 kg/m^3 and ρ_t = 1.56·10^3 kg/m^3 are respectively bulk density of bayerite and tap density of aluminum powder; υ=0.5 is a coefficient accounting for the growing bayerite porosity; σ = 773·10^{-3} J/m^2 is the surface energy at the solution/bayerite interface; S_b= 53·10^3 m^2/kg is the specific surface area of bayerite, V_b=32·10^{-6} m^3/mol is the molar volume of bayerite, C_1=0.027 kg/m^3 is the concentration of aluminum in solution, at which a hydrolytic polymerization reaction begins; r is the initial particle radius, R is the universal gas constant; T is temperature; t is time; and D is the diffusion coefficient. Based on experimental reaction times for 10-μm powders at 373 K, the diffusion coefficient was estimated in [65] to vary in the range of (0.067 – 0.13)·10^{-10} m^2/s. Using the above parameter values (following Reference [65]) Reaction (R1) was solved for the diffusion coefficient, D, and the reaction completeness was expressed through the measured rate of heat release, $\dot{Q}$:

$$\alpha = \frac{1}{Q_{complete}} \int_0^t \dot{Q} dt \tag{2.3}$$

yields:

$$D = \frac{RT\rho_t^2 r^2}{2.24\rho_b^2 \upsilon C_1 \sigma S_b V_b t} \left(\frac{1}{Q_{complete}} \int_0^t \dot{Q} dt \right)^2 \tag{2.4}$$

where $Q_{complete}$ = 15.42 kJ/g is the theoretical maximum heat release expected upon the complete conversion of the entire powder mass load. Thus, using experimental $\dot{Q}(t)$ curves, assessment of the diffusion coefficient is possible.

The time was set to zero at the end of the induction period for each experiment (i.e., when the value of $\dot{Q}(t)$ reached 1% of its maximum value in each run). The calculated values of the diffusion coefficient as a function of the reaction time are shown in Figure 2.14 for the same experiments that were illustrated in Figure 2.10. For each experiment, the particle radius, *r*, was assumed to be equal to the volumetric mean obtained from the size distributions shown in Figure 2.1. This model is not capable of describing the reaction initiation, but it was expected to yield a relatively constant diffusion coefficient, at least during the initial period of fast reaction, when interparticle contacts are limited. The diffusion coefficient should also be independent of the starting particle dimension, but should be strongly affected by the reaction temperature.

Generally, the range of values for *D* shown in Figure 2.14 is higher than that reported in Reference [65], although more consistent with diffusion coefficients if ionic species in aqueous solutions. In Reference [65], the low value observed ($0.067\text{-}0.13 \cdot 10^{-10}$

m^2/s) was explained via the expected porosity of the growing bayerite layer at 373 K, expressed with the parameter υ in Equation (2.1). One could speculate that porosity may be affected by the reaction temperature and a more porous bayerite could have formed in the current experiments, performed at lower temperatures compared to Reference [65]. Images shown in Figures 2.7 and 2.8 suggest that the porosity of the growing bayerite layers changes as the reaction progresses. Because of the correlation between the morphology of the layered bayerite structures and particle sizes, the effective porosity of the growing bayerite controlling the bulk reaction rate for the powder sample may be different for powders with different particle size distributions.

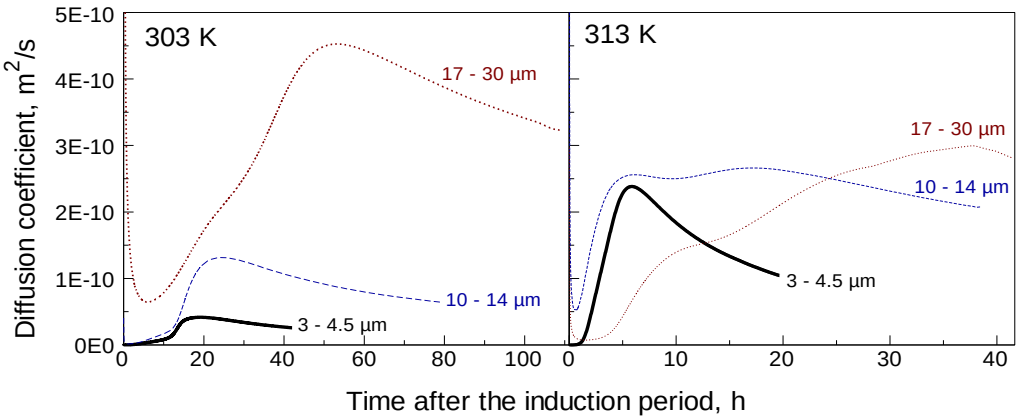

Figure 2.14 Diffusion coefficients for experimental runs illustrated in Figure 2.10 calculated as a function of reaction time corrected for the induction period.

The shape of the curves in Figure 2.14 changes depending on when one considers the model calculations to be applicable, i.e., at what point the time can be set to zero. Given the derivation of Equation (2.1), it should work best for the early stages, while the volume of the bayerite surface layer can be approximated as the product of its thickness and the surface area of the aluminum core. It should begin to apply to material like shown in Figure 2.5, and strong deviations should appear by the time the reaction has progressed

to form material like shown in Figure 2.6. Likewise, there should be no differences between particle sizes. There is however no clear way to determine the limits of the interval in time (or in the reaction progress) from the recorded heat flow curves, for which Equations (2.1) and (2.4) are valid. Therefore, the observed variation of the diffusion coefficient with time, and the effect of the effective particle size on *D* are indicative of the inadequacy of the simplified reaction model, and could change if the time limits were chosen differently. The values shown in Figure 2.14 should be taken as order-of magnitude estimates of the diffusion coefficient as defined by Equation (2.1). As a first step to a more detailed data analysis, the reaction progress must be evaluated considering the whole size distribution instead of the conventional approach relying on the average particle size, which was also followed in the present study.

2.5.3 Termination

Eventually the growing bayerite surface layers of adjacent particles will form bridges, and gradually fill all interstices between adjacent particles (see Figures 2.7 and 2.8). The diffusion path between liquid solution and the surface of the remaining aluminum particles becomes longer until finally the reaction rate becomes so slow that it becomes impractical to continue measurements.

Figure 2.13 suggests that the sample with the smaller particle size shows systematically more complete reaction. This is likely because the reaction is complete for finer powders when a thinner layer of bayerite is grown. In other words, the effect of the growing bayerite thickness on the reaction rate must be accounted for in order to quantitatively interpret the difference in reaction completeness for powders with different particle sizes.

2.6 Conclusions

Reaction of aluminum with liquid water characterized by microcalorimetry includes several parts: induction time, two stages of relatively rapid reaction, and termination. The only reaction product formed at 303 and 313 K is bayerite. The significance of the first of the two rapid reaction stages increased in experiments at 313 K. Generally, finer powders were observed to react faster and to a greater completion. Effects of powder load and mass of water are found to be negligible. Reaction characteristics were poorly reproducible despite well maintained reaction temperatures. It is hypothesized that minor differences in powder packing and trapped gases could substantially affect reaction rates for the processes occurring directly on the particle surfaces, as expected for the alumina hydration occurring during the induction period. Processing the present experimental data using a simplified kinetic model available in the literature showed that the calculated diffusion coefficient for the rate-limiting process is affected by the reaction temperature, particle sizes, and reaction time. While the first effect is expected, the observed effects of particle size and reaction time likely indicate that the model is inadequate for describing the present experiments. Porosity of the growing bayerite, defining the rate of diffusion and thus the reaction rate, changes as a function of the reaction completeness. It is also affected by experimental conditions, including reaction temperature and powder particle size distribution.

Reaction characteristics were poorly reproducible despite well maintained reaction temperatures. It is hypothesized that minor differences in powder packing and trapped gases could substantially affect reaction rates for the processes occurring directly on the particle surfaces, as expected for the alumina hydration occurring during the induction

period. Processing the present experimental data using a simplified kinetic model available in the literature showed that the calculated diffusion coefficient for the rate-limiting process is affected by the reaction temperature, particle sizes, and reaction time. While the first effect is expected, the observed effects of particle size and reaction time likely indicate that the model is inadequate for describing the present experiments. Porosity of the growing bayerite, defining the rate of diffusion and thus the reaction rate, changes as a function of the reaction completeness. It is also affected by experimental conditions, including reaction temperature and powder particle size distribution.

CHAPTER 3

REACTION INTERFACE BETWEEN ALUMINUM AND WATER

3.1 Abstract

Reaction of aluminum with water is of interest for hydrogen generation for a wide range of applications, from in-situ operated fuel cells to propulsion of underwater vehicles. Despite extensive studies, detailed reaction mechanisms are lacking and the locations of the reaction interface between aluminum and liquid water or steam are not identified. In this work, the reaction interfaces are located by interpreting heat flow calorimetry and thermo-gravimetry data for liquid water and steam, respectively. In both experiments, two spherical aluminum powders are used with different but overlapping particle size distributions. The measured reaction rate is assumed to be proportional to the surface area of the reaction interface; thus the measured heat flow and weight gain are partitioned among particles based on their size distribution. The data are processed considering several reaction models assuming different locations of the reaction interface: inside or outside of the growing Al2O3 or Al(OH)3 shells. It is expected that if the correct interface location is selected, the oxidation of the particles with the same sizes and exposed to the same temperature/environment but belonging to different powders will be identical to each other. For liquid water, results suggest that the reaction occurs at the surface of the shrinking aluminum core, inside the growing aluminum hydroxide layer. For reactions of aluminum with steam at elevated temperatures, the results are less conclusive, but indicate that the reaction is most likely occurring at the outer surface of the growing alumina shell. The growing alumina shell is rigid and is fractured multiple times during its growth. After a shell is fractured, a new shell begins to grow around the oxidizing aluminum core.

3.2 Introduction

Recent interest in producing hydrogen and energy by reacting aluminum with water [66, 67] has been driven by need in pollution-free devices, which may exploit Al-H_2O reactions at both high and low temperatures [21, 22]. The Al-H_2O reaction, as a source of energy and hydrogen, becomes attractive economically depending on costs of other energy generation methods [68], and particularly, if recycled scrap aluminum is used [19]. Because the reaction is essentially pollution-free, it is well-suited for generating hydrogen and energy in situ, in populated areas or locations where there is no energy infrastructure. The condensed products formed in the reaction, aluminum oxides and hydroxides, can be used to prepare various ceramic products. In addition, aluminum oxides and hydroxides are benign and can be safely transported to be recycled at locations housing nuclear or solar energy generating facilities. The need in low-temperature, in-situ hydrogen production processes is stimulated by rapid development of fuel cells as portable, flexible, and versatile energy sources [45-47]. Operation of fuel cells requires hydrogen, and its in-situ generation via water split reaction is very attractive as an alternative to establishing an extensive infrastructure. High-temperature Al-H_2O reactions have been of substantial interest for underwater propulsion [69, 70]. In addition, such reactions are investigated in power plant configurations [20].

Despite extensive studies in the context of preparation of Al oxide and hydroxide ceramics [65, 71, 72], the mechanisms of the Al-H_2O reactions on the scale of a single reacting particle, and particularly at atmospheric pressures, have not been reliably established. A protective natural surface layer of alumina is known to inhibit the reaction at low temperatures, and a number of investigations focused on the removal of this

protective layer [51, 54, 56, 73-75]. Recently, it has been suggested that the particle size of aluminum powder affects the rate of reaction relative to the particle specific surface area [76]; however, the specific reasons causing fine particles to be more reactive than coarse ones remain elusive. A model proposed by Deng et al. [77, 78] involves formation of hydrogen bubbles between aluminum and the oxide layer, which may disrupt the oxide layer. Such disruption is possible if the tangential component of the strain developed in the oxide layer is non-negligible, so that the bubble dimensions must be comparable to those of the particles. Considering that particle sizes explored in Reference [76] varied ca. from 1 to 100 μm, it is highly unlikely that comparable size hydrogen bubbles formed. In fact, it has not been reliably established that hydrogen generation occurs at the inside of the alumina layer, i.e., at the interface between aluminum and alumina. Generally, it is possible for the Al-H_2O reaction to occur both inside and outside of the protective oxide or hydroxide layer; furthermore, this reaction location may vary depending on temperature.

The objective of this work is to determine whether the Al-H_2O reaction occurs at the inner aluminum/(hydr)oxide interface or the outer (hydr)oxide/environment interface for a range of temperatures for both liquid water and steam. The experimental approach exploits calorimetric measurements performed at different temperatures using spherical aluminum powders.

3.3 Approach

The approach is based on interpreting the measured heat release and/or mass gain produced by the Al-H_2O reaction using spherical aluminum powders with different but well-characterized and overlapping particle size distributions. Each particle is described in

terms of an unoxidized, shrinking aluminum core embedded in a growing oxide/hydroxide layer, or shell.

The main assumption is that the individual particles react independently of the rest of the sample when exposed to water. In other words, for any particle, the rate of its reaction is assumed to be fully defined by the initial particle size and the specific heating program the particle experiences. The reaction rate is assumed to be insensitive to the particle size distribution characterizing the rest of the powder.

The second assumption is that the reaction rate is proportional to the available area of the interface at which the reaction occurs. Thus, once the particle size distribution is known, it can be recast in terms of surface areas of different size bins, so that the measured heat flow can be distributed among all particles based on their respective interface areas.

The initial thickness of the oxide layer is known or can be estimated. As the reaction proceeds, the evolution of the reactive interface is calculated depending on where the reaction is assumed to occur. This can be either at the external particle surface, or at the surface of the shrinking aluminum core. If the reaction occurs at the outer particle surface, the reactive interface area may increase when the thickness of the growing oxide or hydroxide layer grows. The reactive interface will always decrease if the reaction occurs at the surface of the shrinking aluminum core.

Depending on the interface area, and therefore on the location of the reaction, particles of a given size will contribute to different degrees to the overall oxidation of a powder with a known size distribution. If the location of the reaction is assumed, then an experimentally observed reaction – in terms of weight increase, or evolved heat – can be partitioned overall size bins of the distribution. After this partitioning, and as long as all

measurements were performed using the same temperature program and environmental conditions, particles of the same size but from powders with different size distributions should show an identical evolution of the amount of oxide produced if the reaction has been located correctly. Conversely, a discrepancy in the oxidation dynamics is expected for particles of the same initial sizes (from powders with different size distributions) exposed to the same heating program if the reaction interfaces are located incorrectly.

3.4 Experimental

Measurements were performed using aluminum powders from Alfa Aesar with nominal particle sizes 3-4.5 μm (97.5 % pure) and 10-14 μm (98% pure). Particles of both powders were nominally spherical, as shown in Figure 3.1.

The particle size distributions for both powders were measured using a Beckman-Coulter LS230 Enhanced Particle Analyzer and are shown in Figure 3.2. Respective volumetric average particle sizes are 7.2 and 21.5 μm. It is observed that there is a substantial overlap between the particle size distributions, as highlighted in Figure 3.2. The interpretation of experiments will focus on comparison of oxidation rates for particles in this overlapped size range, approximately 3 – 36 μm.

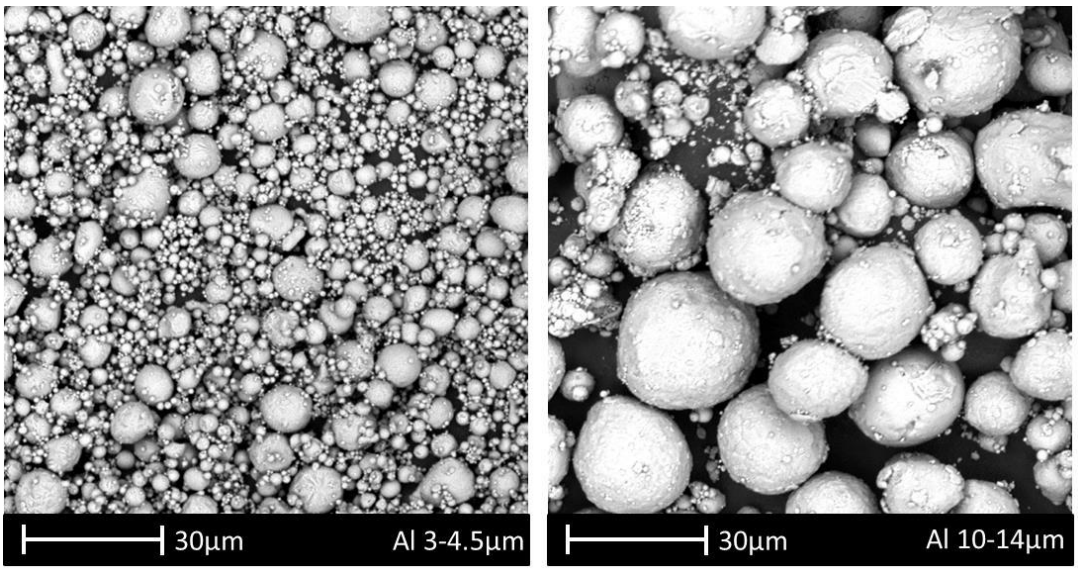

Figure 3.1 Scanning electron microscope images of the powders used.

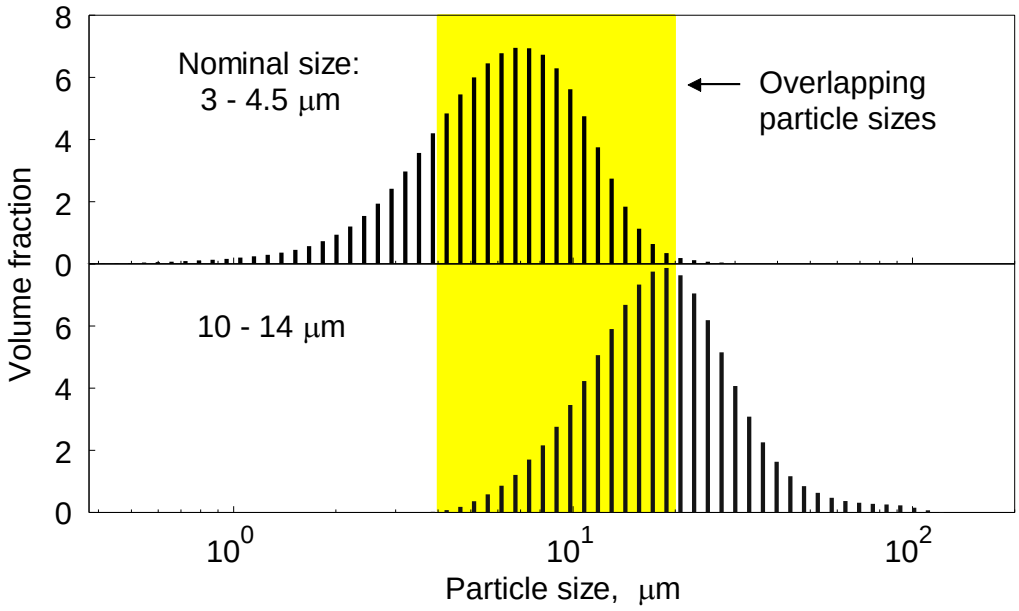

Figure 3.2 Particle size distributions for the aluminum powders.

Powders were reacted with water in a broad range of temperatures and the reaction progress was characterized using heat flow calorimetry and thermogravimetry.

Low temperature experiments with liquid water used isothermal heat flow calorimetry in a TA Instruments TAM III. Measurements were performed using a perfusion ampoule by TA Instruments installed in a minicalorimeter. The perfusion ampoule enables calorimetric measurements for samples subjected to a controlled gas flow or vented to the surroundings. Measurements were carried out at 303 and 313 K (30 and 40 °C, respectively). Samples of approximately 20 mg were contained in 4-mL stainless steel reaction vessels. Aluminum powder was weighed and placed in the reaction vessel. Then, approximately 2 g of distilled water was added to the reaction vessel, and weighed to determine its exact amount. The reaction vessel was then attached to the perfusion ampoule, and the perfusion ampoule was inserted into the minicalorimeter. The time between the first contact of Al powder and water, and the insertion into the calorimeter was always between five and ten minutes. For the insertion, the procedure suggested by the TAM III manufacturer was followed (stepwise insertion, 5-10 minute waiting periods) in order to not overly perturb the calorimeter signal. After insertion, the calorimeter signal was allowed to equilibrate, and was considered to represent the true heat flow after approximately 45 minutes. The perfusion ampoule was flushed with a dry air flow at 50 ml/h. Hydrogen produced as a result of reaction was carried out together with the passing air.

To study reaction of aluminum and water vapor, aluminum powders were heated in a Netzsch STA409PG thermal analyzer using a thermo-gravimetric (TG) sample carrier with a 17 mm diameter flat corundum plate to hold the sample. The furnace of the STA409PG was connected to a pressurized boiler, which was held at 453 K (180 °C). The

connecting lines were heated to temperatures above 423 K (150 °C) to prevent condensation.

Initial experiments established that the aluminum particles heated above the melting point (933 K) tended to coalesce into droplets with sizes in the 0.5-1 mm range. To mitigate the associated drastic loss in surface area, the powders in subsequent measurements were ultrasonically mixed with 150 nm γ-alumina powder (Inframat Advanced Materials, 99.8% pure) to contain approximately 25 wt % free Al. For the blend of alumina and aluminum powders, coalescence was not observed on heating [30]. Samples used for the measurements contained approximately 35 mg of the aluminum/alumina blend.

Argon was introduced into the furnace in two locations. The first invariant gas flow of 20 ml/min serves to protect the thermobalance from any condensation. It enters the furnace from below. Due to the furnace geometry, it has a negligible contribution to the atmosphere that the sample is exposed to. The second argon flow at 5 L/h was used as a carrier gas for steam, entering the furnace from above. The steam flow rate was 0.92 g/h at the boiler temperature, resulting in an atmospheric composition of 20 vol-% H_2O.

Reaction Interface Models

The reaction progress in terms of the oxide or hydroxide shell thickness was directly correlated with the observed heat release or mass change of the sample for heat flow and TG experiments, respectively. The data of the heat flow experiments were recast in terms of mass gain, assuming that the only condensed product forming in the reaction was $Al(OH)_3$, as is typical for the low-temperature Al-H_2O reactions [79]. For TG experiments, the evolution of the particle mass was interpreted considering its oxidation to

Al_2O_3 and respective changes in the particle morphology depending on the assumed location of the reaction interface. The evolution of the oxide shells was tracked by starting at the initial thickness, and iterating over time using the time steps from the experimental signal record. The data processing for each powder explicitly used the measured particle size distribution. The oxidation models, distinguished by the location of the reaction, that were used to interpret the experimental data are shown schematically in Figure 3.3. In Figure 3.3a, the reaction is assumed to occur inside the growing product shell (hydroxide or oxide for heat flow and TG experiments, respectively), at the surface of the shrinking aluminum core. For simplicity, the shell may be thought of as elastic, so it always adheres to the core. However, the shell properties do not affect the area of the reactive interface, which is fully determined by the aluminum core diameter. In Figure 3.3b, the reaction is assumed to occur at the outside of the product shell. The oxide product is assumed to always adhere to the shrinking aluminum core; hence it is referred to as an elastic shell. Finally, in Figure 3.3c, the reaction is assumed to occur at the outside of the product shell, however, the shell is not shrinking together with the aluminum core. Thus, when the aluminum core diameter decreased, a void was assumed to form between the core and shell surfaces. The shape of the void is not important because the reaction occurs at the external surface of the rigid spherical shell. Thus, although the aluminum core is shown in Figure 3.3c as spherical, its shape may change without affecting the surface area of the reaction interface. Note that if the aluminum core diameter increased as a result of thermal expansion, the "rigid" product shell was allowed to expand as well.

For each time step, the experimentally observed mass was distributed over the particle size bins according to the current, continuously updated area of the reactive

interface of this size bin. The size bins and time steps are respectively represented by subscripts *i* and *j*. The evolution of the particle mass m_i with radius of the reactive interface r_i in the time step, *j*, is calculated as:

$$m_{i,j} = m_{i,j-1} + \left(m_j^* - m_{j-1}^*\right)\frac{r_{i,j-1}^2}{\sum_i \left(N_i \cdot r_{i,j-1}^2\right)} \tag{3.1}$$

where N_i is the number of particles in the size bin *i*, and m^* is the mass of the entire sample. For reaction at the core-shell interface (see Figure 3.3a), the aluminum core radius, $R_{i,j}$, in the size bin *i* at the time *j* is calculated as:

$$R_{i,j} = \left[\frac{3}{4\pi\rho_{Al}}\left(m_{i,1} - \frac{2M_{Al}\left(m_{i,j} - m_{i,1}\right)}{M_{pr} - 2M_{Al}}\right)\right]^{1/3} \tag{3.2}$$

where ρ_{Al} is the aluminum density (taken as a function of temperature), and M_{Al} and M_{pr} are molar masses of aluminum and product (Al_2O_3 or $Al(OH)_3$), respectively. The evolution of the product shell thickness h_i for cases shown in Figure 3.3a and 3.3b, (elastic shell) is calculated as:

$$h_{i,j} = \left[R_{i,j}^3 + \frac{3}{4\pi\rho_{pr}} \cdot \frac{2M_{pr}\left(m_{i,j} - m_{i,1}\right)}{M_{pr} - 2M_{Al}}\right]^{1/3} - R_{i,j} \tag{3.3}$$

The evolution of the oxide thickness h_i for the case shown in Figure 3.3c, (rigid oxide) is calculated as:

$$h_{i,j} = \left[R_{i,0}^3 + \frac{3}{4\pi\rho_{pr}} \cdot \frac{2M_{pr}\left(m_{i,j} - m_{i,1}\right)}{M_{pr} - 2M_{Al}} \right]^{1/3} - R_{i,0} \qquad (3.4)$$

where ρ_{pr} is the density of product shell, and $R_{i,0}$ is the initial (i.e. maximum) core radius for size bin *i*. Only one aluminum oxide phase is assumed to exist for each time step. According to Reference [31], for the heating rate used in TG experiments, 5 K/min, the phase transitions from amorphous to γ-Al_2O_3 and from γ- to α–Al_2O_3 occur respectively at 660 and 1031 ^{o}C. Respective changes in the oxide densities were included in the calculations.

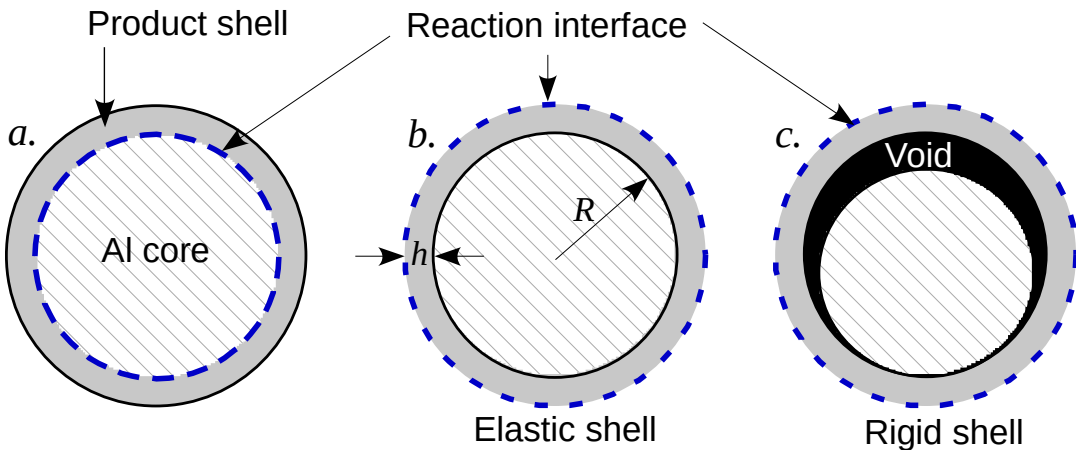

Figure 3.3 Schematic diagram of oxidation configurations. A. Reaction at the inner Al/product interface; b. Reaction at the outer product shell interface, elastic shell; c. Reaction at the outer product shell interface, rigid shell.

3.5 Results and Discussion

3.5.1 Aluminum Reaction with Liquid Water

Characteristic heat flow traces for two aluminum powders reacting with liquid water at 313 K are shown in Figure 3.4. Similar results were recently reported in Reference [80], where it was shown that particles are strongly agglomerated, losing their spherical shapes by the end of experiment. In order to use the present approach for interpreting the experimental data, only the initial portions of the measured traces, which are less likely to be affected by agglomeration, were processed. Specifically, a time period of about six hours shaded in Figure 3.4 and comprising one peak in the recorded heat flow traces was selected.

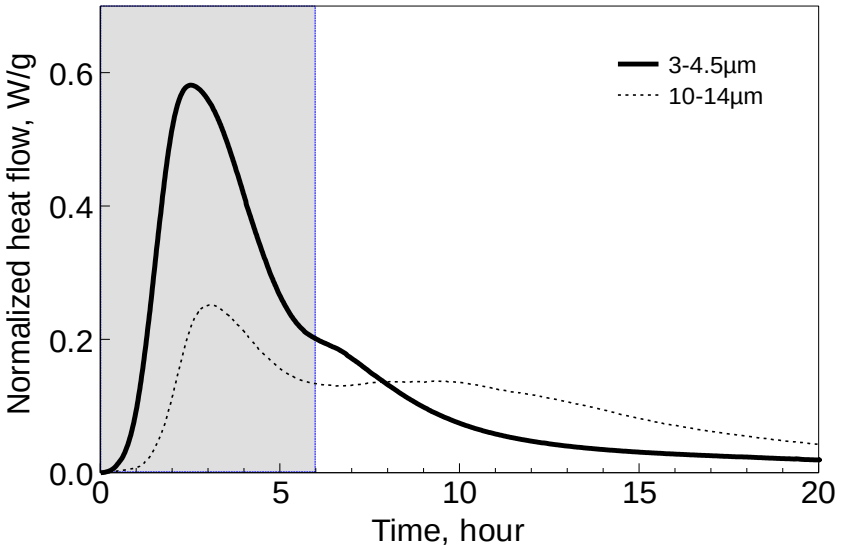

Figure 3.4 Heat flows measured for the Al-H_2O reaction at 313 K.

The mass gains for two aluminum powders reacting with liquid water at a constant temperature calculated using traces shown in Figure 3.4 are shown for the first 6 hours of reaction in Figure 3.5.

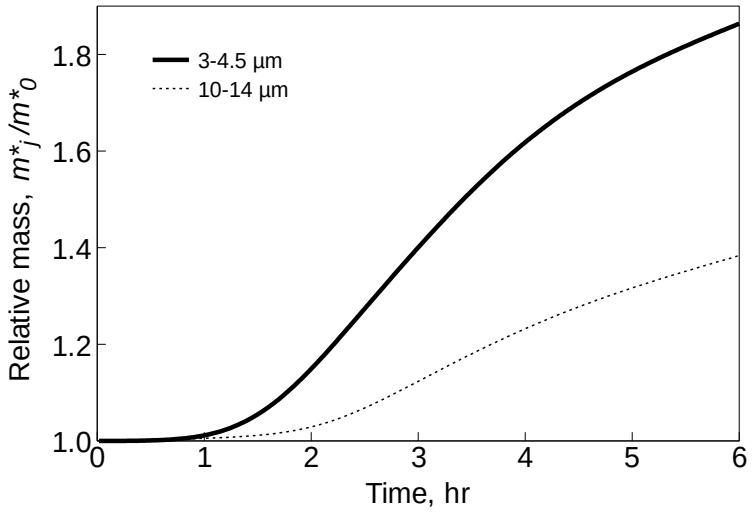

Figure 3.5 Mass gain for two aluminum powders reacting with liquid water during the initial 6 hours in mini-calorimeter at 313 K.

The increase in the sample mass, m^*, was distributed among different particle size bins, using Equation (3.1). The oxidation dynamics was then compared for individual aluminum particle sizes or size bins present in the overlapping portions of size distributions for both powders investigated. Specific size bins selected to illustrate such comparisons in detail were 4.6, 10.7 and 18.8 µm, (cf. Figure 3.2), located at the edges and in the middle of the overlapping portion of the size distributions.

Each experiment was processed considering three reaction models illustrated in Figure 3.3 a, b, and c. Each model was used to calculate oxidation dynamics for particles in each size bin. Comparisons of the oxide thicknesses predicted to grow by the three models for particles in the selected size bins are shown in Figures 3.6-3.8.

The model describing the experimental data correctly should predict a complete overlap between the two calculated curves for all particle sizes. Conversely, if the model used in calculations does not represent the experiment, the evolution of the reactive

interface will not be accurately represented resulting in a discrepancy in the predicted oxidation rates for the particles of the same sizes that belong to different powders.

Qualitatively, it is clear from Figures 3.6-3.8 that the model assuming the reaction to occur at the inner aluminum/hydroxide shell interface results in the best match between the two calculated curves for all three particle sizes considered.

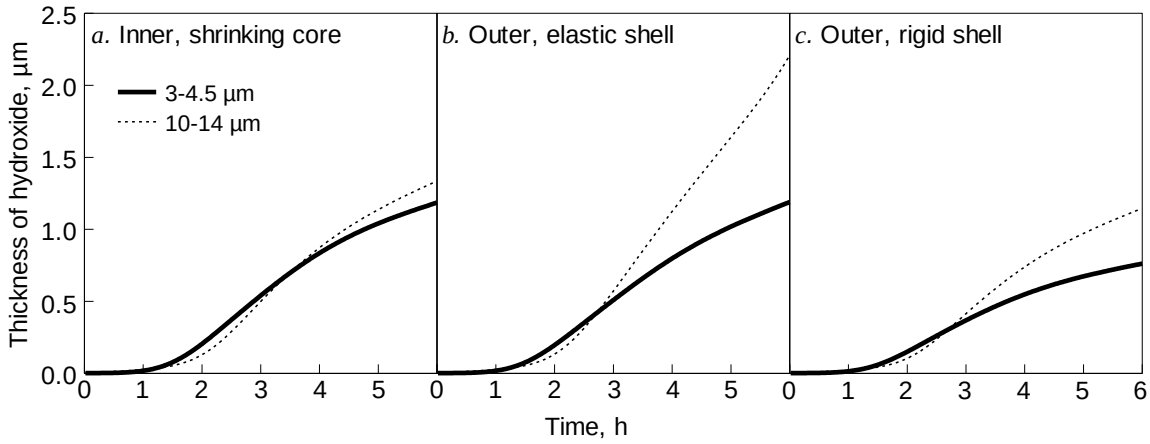

Figure 3.6 TAM III experiment processing: thickness of a hydroxide shell predicted to grow around an aluminum particle with the initial diameter of 4.6 µm using three different oxidation models shown in Figure 3.3.

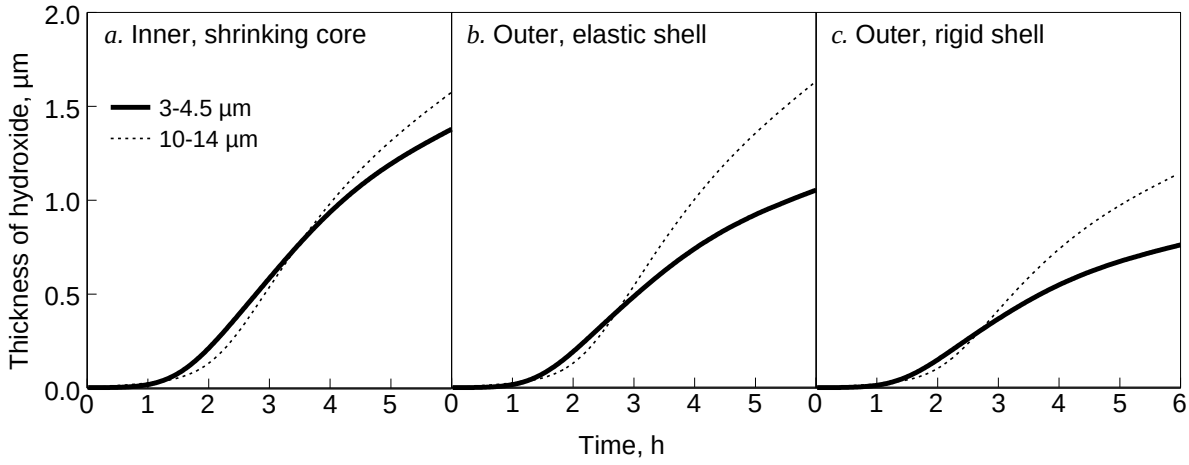

Figure 3.7 TAM III experiment processing: thickness of a hydroxide shell predicted to grow around an aluminum particle with the initial diameter of 10.7 µm using three different oxidation models shown in Figure 3.3.

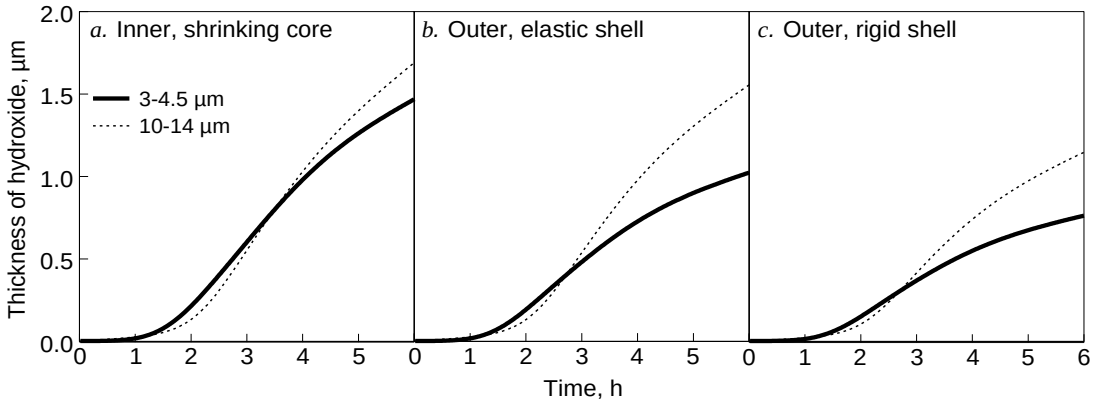

Figure 3.8 TAM III experiment processing: thickness of a hydroxide shell predicted to grow around an aluminum particle with the initial diameter of 18.8 µm using three different oxidation models shown in Figure 3.3.

To quantitatively compare the calculated curves for all particle sizes for the entire time of the experiment, the following parameter R_i was calculated for each particle size bin, i:

$$R_i = \sqrt{\frac{\sum_{j=1}^{J}\left(\Delta m_{i,j}^{I} - \Delta m_{i,j}^{II}\right)^2}{J}} \tag{3.5}$$

where $m_{i,j}^{I}$ and t $m_{i,j}^{II}$ are weight changes (in percent) for the particles of two aluminum powders (subscripts *I* and *II* stand for the powders with nominal sizes 3-4.5 and 10-14 µm, respectively) for j^{th} time step. The summation is taken for all *J* time steps available during the measurement time of six hours. Parameter R_i calculated using Equation (3.5) reduces the difference between curves shown in Figures 3.6-3.8 to one number, quantifying discrepancy between the curves over the entire measurement. Parameter R_i is plotted in Figure 3.9 for all particle sizes considered. It shows, consistently with Figures 3.6-3.8, that

the discrepancy between predictions is minimized when the reaction is assumed to occur at the inner interface between aluminum and the growing hydroxide shell.

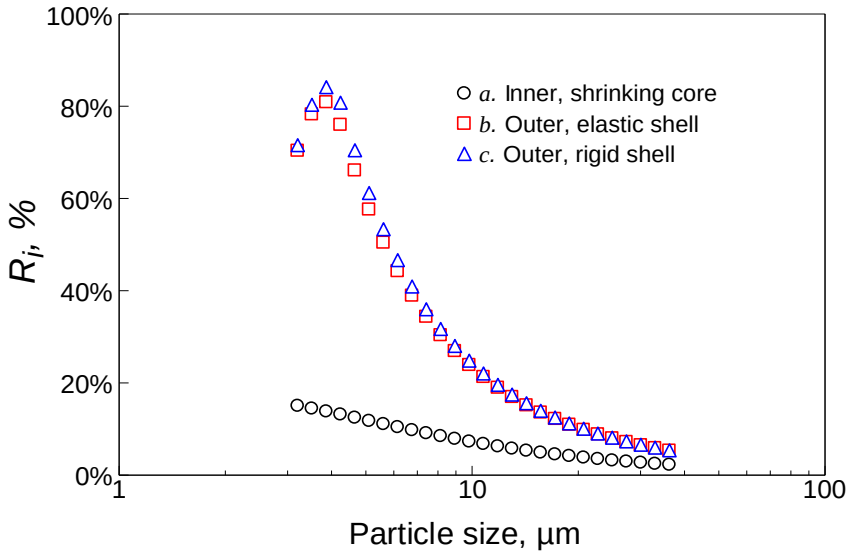

Figure 3.9 TAM III experiment processing: cumulative discrepancy measure calculated using Equation (3.5) for data processing using different reaction models.

3.5.2 Aluminum Reaction With Steam

Measured TG traces for two aluminum powders are shown in Figure 3.10. Similar to processing the heat flow curves above, the measurements were processed to distribute the overall mass increase among different particle size bins for each powder. For clarity, the mass changes were converted into oxide thickness for particles of different sizes belonging to different powders. Resulting detailed comparisons between the models for the same three selected initial particle sizes, 4.6, 10.7 and 18.8 μm, as considered above, are shown in Figures 3.11 – 3.13.

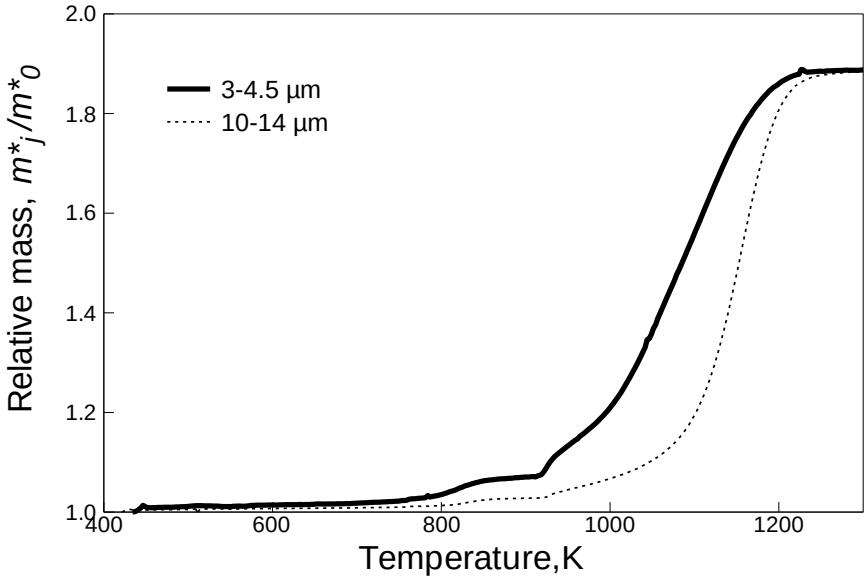

Figure 3.10 TG traces for two aluminum powders reacting with steam; heating rate 5 K/min.

All particles considered in Figures 3.11-3.13 are predicted to oxidize completely during the experiment; hence the oxide thickness in each case reaches its maximum possible value. It is interesting that for the case of rigid shell that never shrinks (unlike the shells considered in the other two cases), the oxide thickness is substantially smaller because the final diameter of the oxide shell is greater. Comparisons between different models do not appear as straightforward as for the case of aluminum reaction with liquid water. For the smallest particle size considered, 4.6 µm (Figure 3.11), the models assuming reaction to occur at the external surface appear to produce better matching curves. However, for larger particles (Figures 3.12 and 3.13), the model accounting for reaction at the inner Al-Al_2O_3 interface appears to yield curves that are closer to each other for different powders. Figure 3.11. TG experiment processing: thickness of an oxide shell predicted to grow around an aluminum particle with initial diameter of 4.6 µm using three different oxidation models shown in Figure 3.3.

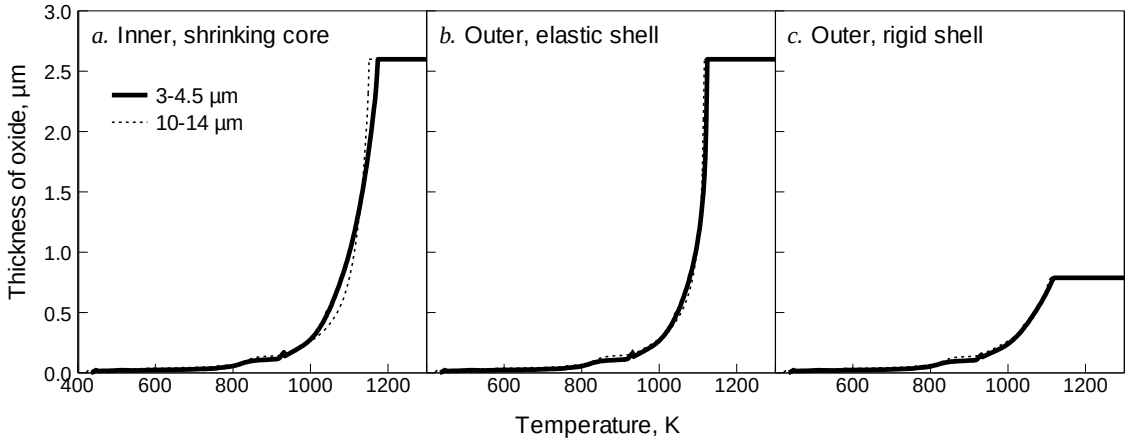

Figure 3.11 TG experiment processing: thickness of an oxide shell predicted to grow around an aluminum particle with initial diameter of 4.6 µm using three different oxidation models shown in Figure 3.3.

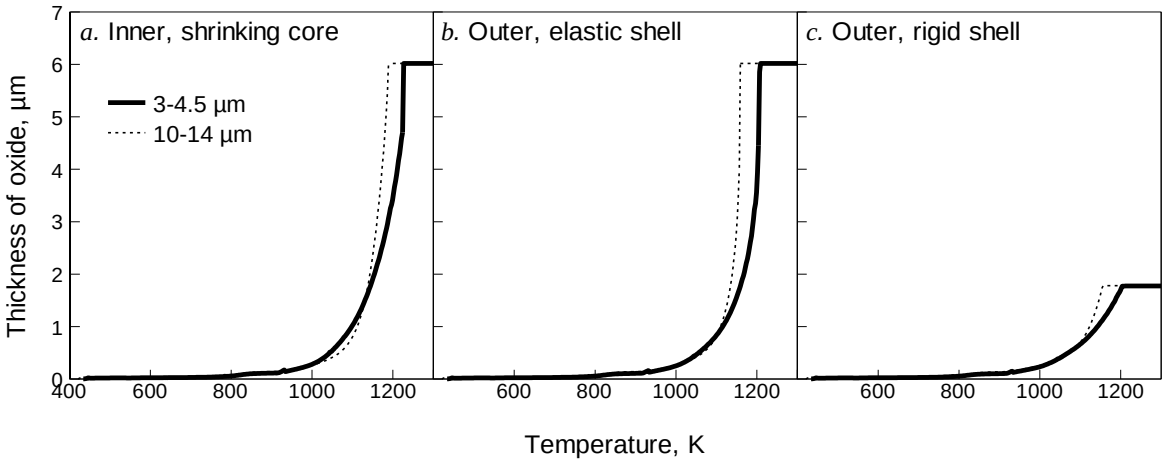

Figure 3.12 TG experiment processing: thickness of an oxide shell predicted to grow around an aluminum particle with initial diameter of 10.7 µm using three different oxidation models shown in Figure 3.3.

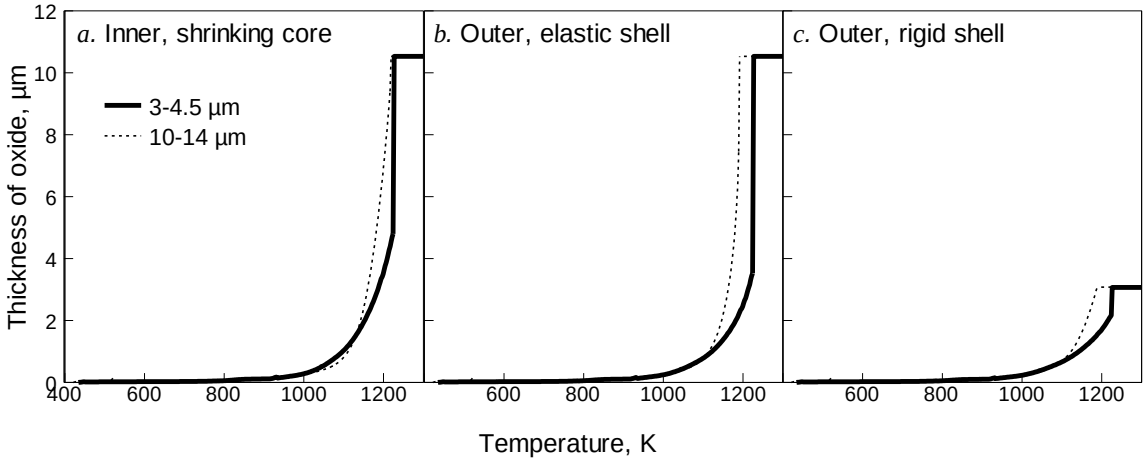

Figure 3.13 TG experiment processing: thickness of an oxide shell predicted to grow around an aluminum particle with initial diameter of 18.8 µm using three different oxidation models shown in Figure 3.3.

To better quantify the differences between different models, parameter R_i was calculated using Equation (3.5) and the results are shown in Figure 3.14. In qualitative agreement with observations made from Figures 3.11-3.13, for particles greater than ca. 7 µm, the model assuming the reaction to occur at the inner metal/oxide interface results in a better match between the calculated oxide thicknesses. For finer particles, the discrepancy between the predicted oxidation traces is the smallest for the model assuming a growing rigid shell. A fourth trend labeled as "outer, breaking shell" shown in Figure 3.14 is discussed below.

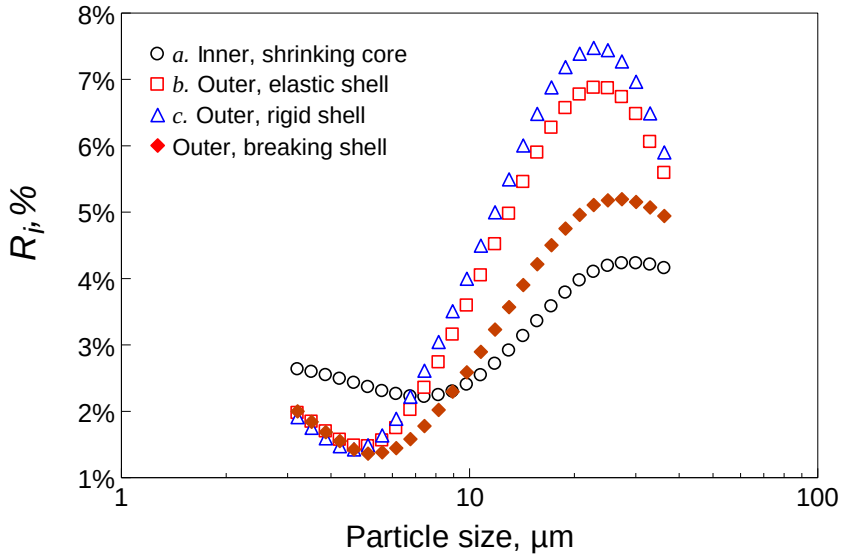

Figure 3.14 TG experiment processing: cumulative discrepancy measure calculated using Equation (3.5) for data processing using different reaction models.

In order to clarify the reaction mechanism of aluminum in steam, several TG runs were interrupted. Partially and fully reacted samples were recovered and examined using a scanning electron microscope (SEM). In preliminary tests, it was observed that the oxidized particles became very fragile, and any handling of the partially oxidized powder resulted in dramatic disruption of its morphology. Disrupted samples examined under SEM exhibited multiple broken alumina shells; it was unclear whether these broken shells formed during the experiment or resulted from handling a fragile sample. Therefore, a separate set of TG experiments was performed. A small alumina plate was coated with a monolayer of aluminum powder and placed in the TG sample holder. To prepare the monolayer powder coating, a slurry of aluminum in hexane was prepared and deposited on the alumina plate with a small paint brush. The hexane evaporated in a few minutes and the coated plate placed in the TG sample holder was subjected to a desired heating program. While mass change in such experiments was too small to be detected by TG, the heating

program was selected based on data from Figure 3.10. For example, heating a sample to 800 °C resulted in about 50% oxidation. After the experiment, the entire alumina plate was transferred to SEM sample holder and the shapes of particles subjected to heating were examined. A characteristic set of SEM images for the powder heated to 800 °C is shown in Figure 3.15. A second set of images for the fully oxidized powder is shown in Figure 3.16.

In both sets of images, multiple cracked oxide shells are apparent. It is also apparent that the oxide shells are not empty, so the observed morphology is qualitatively similar to that expected for the oxidation scenario involving a rigid oxide shell (Figure 3.3 c). However, some of the particles appear to exhibit several successive but distinct oxide shells. This morphology could be obtained if a new oxide shell begins forming after the initial oxide shell cracks.

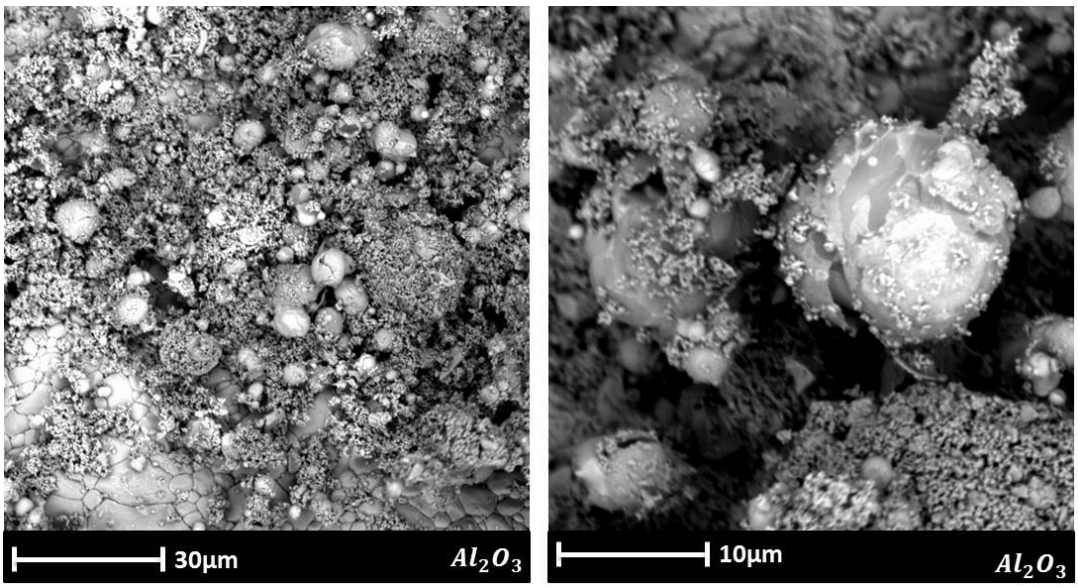

Figure 3.15 SEM images of aluminum powder (nominal particle sizes 3-4.5 µm) heated in a TG experiment to 800 °C and recovered without disrupting particle morphology.

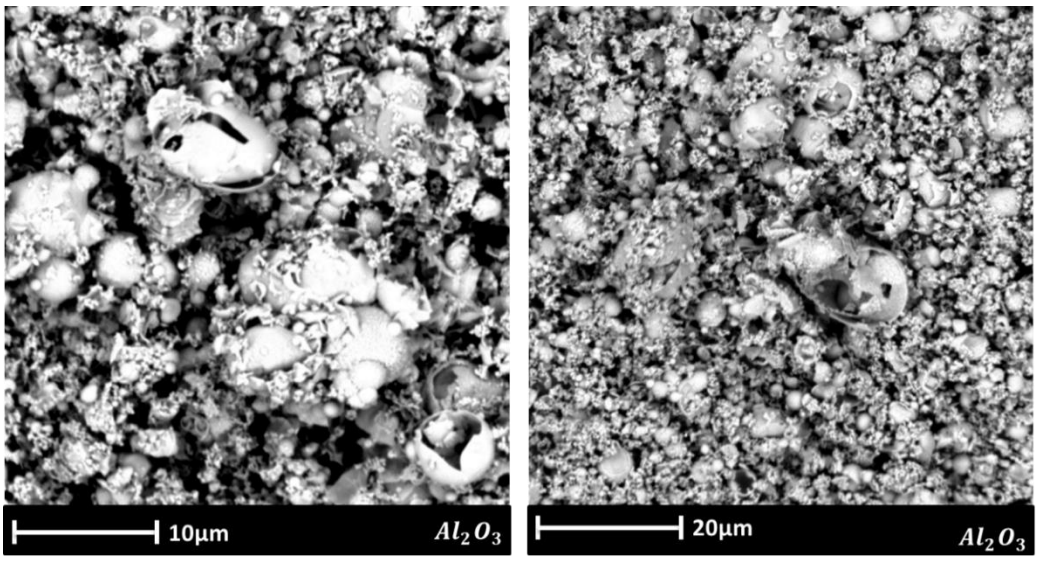

Figure 3.16 SEM images of aluminum powder (nominal particle sizes 3-4.5 μm) fully oxidized in a TG experiment recovered without disrupting particle morphology.

To examine the possibility of forming multiple oxide shells, a modified oxidation model was considered. The model altered the outer surface reaction mechanism (Figure 3.3c) by introducing cracks in the growing rigid shell, when its thickness exceeded some specific value. Once the shell's thickness increased the specific value and the shell was assumed to crack, it was no longer considered to be the barrier to the reaction. The effect of a cracked shell was then the formation of a new shell beneath the broken shell at the shrinking aluminum core surface. Thus, formation of multiple successive shells was described. Clearly, the cracks in the alumina shell depend not only on its thickness, but also on the shell diameter and temperature. However, for a first approximation, the cracks were assumed to form in all shells after some pre-set, "critical" thickness was achieved. Cases with different critical thickness were considered and R_i values for a calculation assuming the critical thickness of 0.5 μm are shown in Figure 14 (labeled as "outer, breaking shell"). Selection of a greater critical thickness results in a greater R_i values for

large particles. Selection of smaller R_i thickness causes the model to become very similar to the inner, shrinking core model.

Note that the in this outer breaking shell model, unlike the model shown in Figure 3.3c, the shape of the aluminum core may be important as defining the shape of the new oxide shell forming after the "parent" shell cracked. In the present analysis, for simplicity the aluminum core was always assumed to remain spherical. Relaxing this assumption could further improve the accuracy of calculations.

For small particles, for which the shell thickness exceeds the critical value by the end of the experiment, the introduction of the breaking shell does not result in a significant effect compared to the initial outer, rigid shell model. As the particle size increases, the breaking shell model describes the reaction best for particles as large as 9 μm. However, for larger particles, the R_i values for this model become greater than for the inner reaction model.

To better understand the oxidation mechanism, it is useful to consider the evolution of the aluminum core for particles of different sizes as shown in Figure 3.17. This evolution is predicted using both the inner, shrinking core and the outer, breaking shell models (the critical shell thickness was 0.5 μm.) For all particles, the core radius remains nearly constant until the particles melt, which is explained by competition between consumption of aluminum and thermal expansion. Melting results in a reduced aluminum density and thus a sharp increase in the core radius. The core radius decreases at higher temperatures. It is apparent that the outer breaking shell model describes oxidation of all particle sizes better when temperatures vary between the melting point and up to about 1100 K. When the temperatures exceed 1100 K, finer particles are fully oxidized. For

coarser particles, discrepancy between the curves is significant for both models, while it is somewhat greater for the outer breaking shell model.

Spherical particle shapes are less likely to be preserved as temperatures increase. Predictions from both models become less reliable for deformed particles. Thus, correlation between the curves at lower temperatures, when particles are more likely to stay spherical, is considered to be a more significant indicator of the successful process description. Conversely, the discrepancies between the curves observed at elevated temperatures may not necessarily indicate a failure for the model focused on identifying the reaction interface for spherical powders.

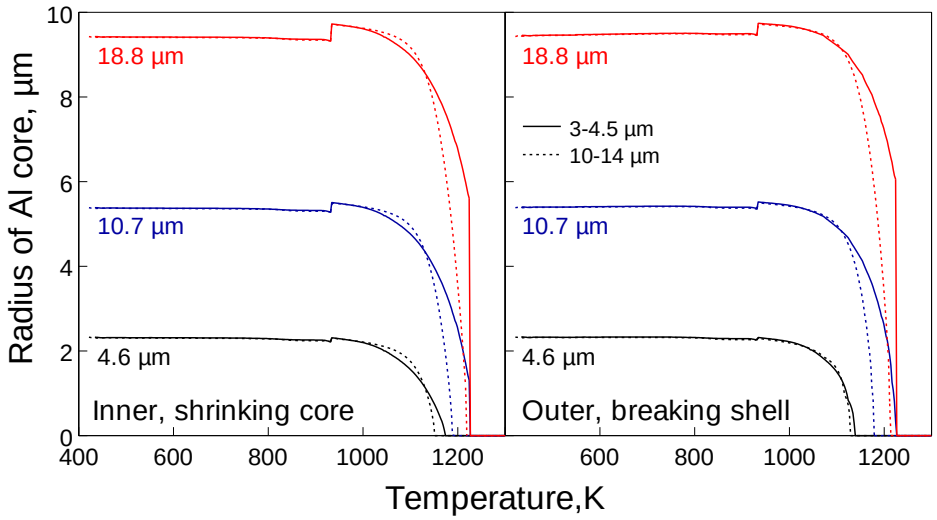

Figure 3.17 Radius of the remaining Al core for the shrinking core model (see Figure 3.3a), and the outer, breaking shell model.

3.6 Conclusions

Location of the reaction interface for aluminum with water is identified for both liquid water and steam. For liquid water, processing flow calorimetry data for two spherical

aluminum powders with different but overlapping particle size distributions suggests that the reaction occurs at the surface of the shrinking aluminum core, inside the growing aluminum hydroxide layer. For reaction of aluminum with steam at elevated temperatures, the results are less conclusive, but indicate that the reaction is most likely occurring at the outer surface of the growing alumina shell. The results also indicate that the growing alumina shell is rigid and fractures multiple times during growth. After a shell is fractured, a new shell begins to grow around the oxidizing aluminum core. The current results are best explained when it is assumed that the alumina shells fracture when they become thicker than 0.5 μm; however, the detailed fracturing mechanism will depends on particle size and temperature.

CHAPTER 4

ALUMINUM OXIDATION AT LOW TEPERATURES

4.1 Abstract

Oxidation of aluminum powders is known to include several stages, corresponding to growth of different polymorphs of alumina. The initial oxide layer is amorphous, which transfers to g-Al_2O_3 at elevated temperatures and greater oxide thicknesses. This work focuses on quantitative characterization of oxidation for thin initial oxide layers and occurring at relatively low temperatures. The experiments include different types of thermo-gravimetric (TG) measurements with increased amounts of powder load for greater sensitivity. Modulated and isothermal TG measurements were found to be less useful than constant heating rate measurements. Results were processed considering both an explicit oxidation model and a model-free isoconversion method. The latter approach was more productive in identifying the activation energy of oxidation. Using the found activation energy as a function of reaction progress, pre-exponent as a function of reaction progress was also found assuming specific reaction mechanism. The reaction kinetics was validated by comparison between predicted and measured oxidation rates for nano-aluminum powders reported in the literature. Finally, the oxidation model was combined with the heat transfer model to describe ignition of aluminum particles exposed to a heated oxidizing environment. A sharp increase in the ignition temperature from 850 to 2260 K is predicted as the particle size increases from 0.3 to 1.2 μm. The results are found to be sensitive to the assumed initial oxide thickness (2.5 nm); they are also somewhat affected by the value of thermal accommodation coefficient used in the heat transfer model.

4.2 Introduction

Aluminum powder is the most commonly used metal fuel additive to propellants, explosives and pyrotechnics [1, 81-85]. Its main advantages are high combustion enthalpy, high flame temperature and a relatively low cost. Another advantage of aluminum powder is its long term stability due to the protective properties of the naturally formed surface alumina film. However, a delayed ignition caused by the diffusion resistance of the same alumina film often becomes a bottleneck to the overall burn rate of aluminum particles. Predicting this ignition delay for different conditions and for powders with different PSDs is important for proper design of energetic systems employing aluminum powders.

The ignition delay is controlled by heterogeneous oxidation of aluminum powders. Such oxidation processes focusing on bulk rates characterizing polycrystalline powders rather than oxidation of a specified crystallographic plane, were subject of different experimental studies [25, 27, 86-89]. Based on detailed thermo-analytical measurements, a quantitative model of aluminum oxidation was proposed and included in a simplified particle ignition model [31, 90]. The model treats simultaneous growth and phase transformations in the aluminum oxide scale, which is initially amorphous, but transfers to $\gamma-$ and $\alpha-Al_2O_3$ phases at elevated temperatures. Four stages of oxidation were identified; the kinetic parameters for both direct oxidative growth of individual alumina polymorphs and phase transformations between the polymorphs were determined. The model assumed that the reaction occurred at the aluminum-alumina interface and was rate limited by inward diffusion of oxygen. More recent work identified that the reaction occurs at the aluminum oxide surface, and thus it is rate-limited by the outward diffusion of aluminum[91]. In addition to the above deficiency, substantial uncertainties remained for

the low-temperature oxidation. Because of its relatively low rate, this process affects the ignition delays significantly; yet, it is the most difficult to quantify experimentally. Low-temperature reactions become particularly important for finer powders and nano-powders, for which an even relatively slow oxidation causes substantial heat release because of the high specific surface area.

In this work, the focus is on oxidation of aluminum at low temperatures, when the oxide thickness is relatively thin. New thermo-analytical measurements are performed and interpreted taking into account location of the reaction interface identified in Reference [91]. A quantitative description of low-temperature oxidation of aluminum is proposed, which improves the accuracy of the previous model. The improved model is validated by comparison with the present and published earlier experimental data. Applicability and limitations of the proposed model for describing aluminum ignition are also discussed.

4.3 Experimental

A 97.5% pure spherical aluminum powder by Alfa Aesar with a nominal particle size of 3-4.5 μm was used. A PSD measured using a Beckman-Coulter LS230 analyzer is shown in Figure 4.1. The volumetric average particle size is 7.2 μm.

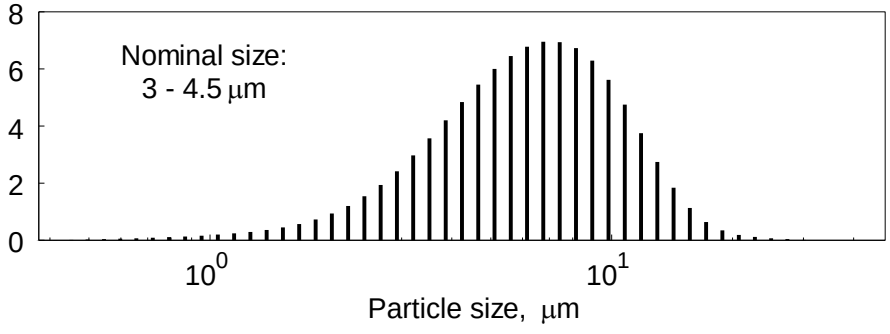

Figure 4.1 Particle size distribution for spherical aluminum powder used in experiments.

The powder was heated up to 873 K at 4 heating rates: 2, 5, 10 and 20 K/min, in a TA Instruments model Q5000IR thermo-gravimetric analyzer. In all thermo-gravimetric (TG) experiments, the balance was purged with argon at 10 mL/min and the furnace was purged with oxygen at 20 mL/min. For the fixed heating rate measurements, 30 mg of powder was loaded in an alumina crucible for each run. This exceeds significantly the mass of sample used in the previous work to better detect a relatively small weight change occurring at low temperatures.

Isothermal oxidation measurements were also performed. The powder was heated up at 20 K/min to selected different target temperatures between 638 and 691 K, while exposed only to argon. Oxygen flow was turned on when the target temperature was reached. The constant temperature was then kept for 480 minutes. The mass of aluminum powder loaded into an alumina crucible was increased to 100 mg to detect weight changes at constant temperatures.

Preliminary measurements were performed using modulated heating rates with modulation amplitudes of 1, 4, and 5 K, and periods of 120 s and 240 s. These measurements were consistent with the constant heating rate and constant temperature measurements, but did not yield comparable resolution in the specific small oxide thickness range of interest, and were therefore not considered further.

4.4 Processing of TG Measurements

The measured net weight gain was distributed proportionally to the reactive interface area among all powder particles. The measured PSD and the location of the reaction interface

were explicitly accounted for. For each time step, , *dt*, the overall weight gain, *dm*, was determined, and used to obtain the weight gain dm_i for a particle in the size bin, *i*:

$$dm_i = \frac{R_i^2}{\sum_{i=1}^{N} f_i R_i^2} dm \tag{4.1}$$

where R_i is particle radius in the size bin *i*, f_i is the fraction of the powder surface area per size bin obtained from the measured PSD, and index i counts the particle size bins, from 1 to N. This particle size-based breakdown of net TG measurements yields the mass change for individual particle sizes given a TG measurement and the PSD of the powder used. It was originally introduced, and described in detail, elsewhere [92]. Once the mass of an individual size bin is known, a core-shell geometry is assumed, and the initial oxide layer thickness is fixed, then the corresponding oxide mass, inner and outer oxide shell radius are readily calculated.

A previously introduced aluminum oxidation model described the oxidation rate as rate limited by diffusion through the growing spherical oxide layer with external radius R_i and internal radius r_i [31]:

$$\frac{dm_i}{dt} = Ca \frac{e^{\left(-\frac{Ea}{R_{gas}T}\right)}}{\left(\frac{1}{r_i} - \frac{1}{R_i}\right)} \tag{4.2}$$

where *T* is temperature, E_a is activation energy, *C* is pre-exponent in units of kg/(m·s), and R_{gas} is the universal gas constant. The size-dependent initial internal oxide radius can be

obtained from the experimentally determined PSD and literature values for the initial natural oxide layer. Note that as the oxidation continues, r_i may become different from the radius of the oxidized aluminum core; see Reference [92] for details. A thin film of amorphous Al oxide is always formed when aluminum powder is exposed to a room temperature oxidizing environment. The thickness of Al2O3 reaches 2 to 4 nm in several hours [93]. Detailed studies of growth of amorphous Al2O3 films on initially bare Al substrates showed layers of approximately uniform thickness near 2 nm and 4 nm if substrates were heated up to 573 K and 673 K, respectively [94]. For processing of the present TG results, thickness of the initial Al2O3 was assumed to be 2.5 nm based on reported electron microscopy analyses for aluminum powders [95]. The oxide was assumed to be of uniform thickness, and adhering to spherical aluminum particles. Sensitivity of results to the assumed value of the initial oxide thickness is briefly discussed below.

Rearranging Equation (4.2), one obtains:

$$\ln\left(\frac{dm_i}{dt}\right)+\ln\left(\frac{1}{r_i}-\frac{1}{R_i}\right)=-\frac{E_a}{R_{gas}T}+\ln\left(C_a\right) \tag{4.3}$$

Following Reference [31], left hand side of Equation (4.3), which is fully determined by the measured TG curve can be plotted vs. inverse temperature to determine the activation energy as a slope of the obtained line, and thus activation energy, E_a. Because the left hand side of Equation (4.3) is obtained explicitly from the TG measurements, both activation energy and pre-exponent can be found for each inverse temperature. Thus, kinetic parameters defining reaction given by Equation (4.2) can be

found as a function of temperature, or, more usefully, as a function of the particle mass. The mass is related to the change in the oxide layer thickness via the assumed core-shell geometry.

Alternatively, activation energy as a function of reaction progress can be found using a model free isoconversion method [96]. Most kinetic methods consider the reaction rate as a function of a kinetic triplet, including activation energy, E_a, pre-exponent, C, and a function of a suitably defined reaction progress, $f(\alpha)$:

$$\frac{d\alpha}{dt} = -C_a \cdot e^{\left(\frac{E_a}{R_{gas}T}\right)} \cdot f(\alpha) \tag{4.4}$$

The kinetic parameters C and E_a can be determined as functions of the particle mass, and therefore as functions of oxide layer thickness from a set of measurements with different heating programs without having to specify the term $f(\alpha)$. From a set of isothermal measurements, E_a and C were determined directly by taking the logarithm of Equation (4.4), and plotting $ln\left(\frac{dm_i}{dt}\right)$ vs. inverse temperature. For the measurements at constant heating rate, the isoconversion algorithm described in Reference [97] was used. Since this algorithm did not readily yield values for C, the pre-exponent was calculated by solving Equation (4.2) for C, and using the activation energy determined by the isoconversion algorithm, and the records of particle mass mi, inner and outer oxide shell radius, r_i, and R_i which were all obtained from the PSD-based breakdown of the individual TG measurements described above.

4.5 Results

Results of constant heating rate and isothermal TG measurements are shown in Figures 4.2 and 4.3, respectively. A consistent shift to higher temperatures is observed for the traces shown in Figure 4.2 at increasingly higher heating rates. These measurements are consistent with earlier reports, e.g., [25]; however, low-temperature oxidation is resolved better because of the greater initial sample mass. Also, as expected, the oxidation rate increases at elevated temperatures in data shown in Figure 4.3. The measurement at 658 K was repeated and resulted in the trace that effectively overlapped with the first measurement at this temperature.

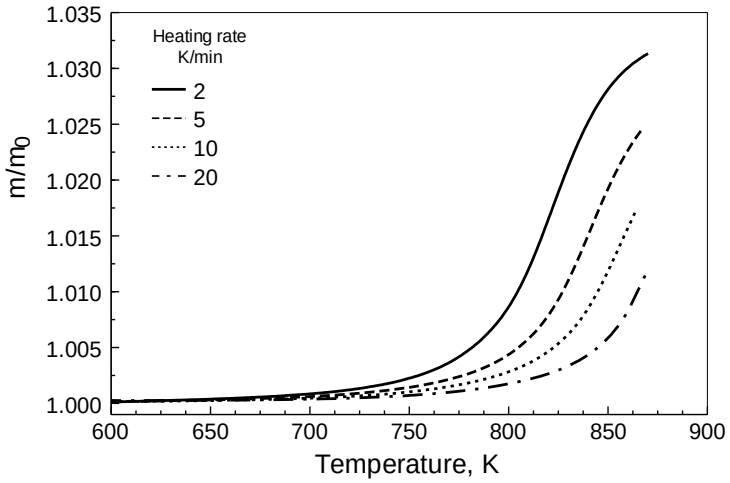

Figure 4.2 TG traces for aluminum oxidation in oxygen obtained for different heating rates.

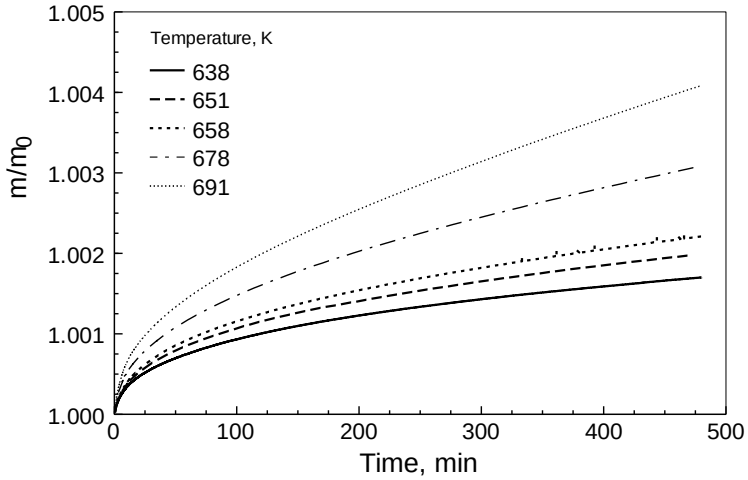

Figure 4.3 TG traces for aluminum oxidation in oxygen obtained at different fixed temperatures.

All activation energies of aluminum oxidation at low temperatures obtained using different data processing methods are plotted together as a function of aluminum oxide thickness in Figure 4.4. Aluminum oxide thickness is selected as a convenient indicator of oxidation progress, which could be universally applied to characterize reactions for powders with different particle sizes. Different dashed traces represent the activation energies of aluminum oxidation calculated based on processing the individual TG measurements and employing the explicit oxidation model described by Equation (4.3). Each trace is thus based on a single measurement. The solid black and gray traces represent the activation energies calculated using the model-free isoconversion processing applied to the constant heating rate and isothermal measurements, respectively. Each line is calculated processing all available measurements simultaneously.

The activation energies calculated using Equation (4.4) for the individual traces are noisy for low temperatures and, respectively, thin oxide films. The noise is particularly strong for the trace based on a 2 K/min measurement. However, a close inspection shows

that the average activation energies for thin films obtained from the individual traces at low temperatures follow closely that obtained using the model-free isoconversion processing applied to all constant heating rate measurements. The latter trace is smoother and easier to follow. The trend for the activation energy obtained from the model-free isoconversion processing applied to the constant temperature measurements is reasonably close to that obtained from constant heating rate measurements for small oxide thicknesses. For the isoconversion processing, the constant temperature measurements are limited by relatively small thickness, attained in experiments with lowest temperatures.

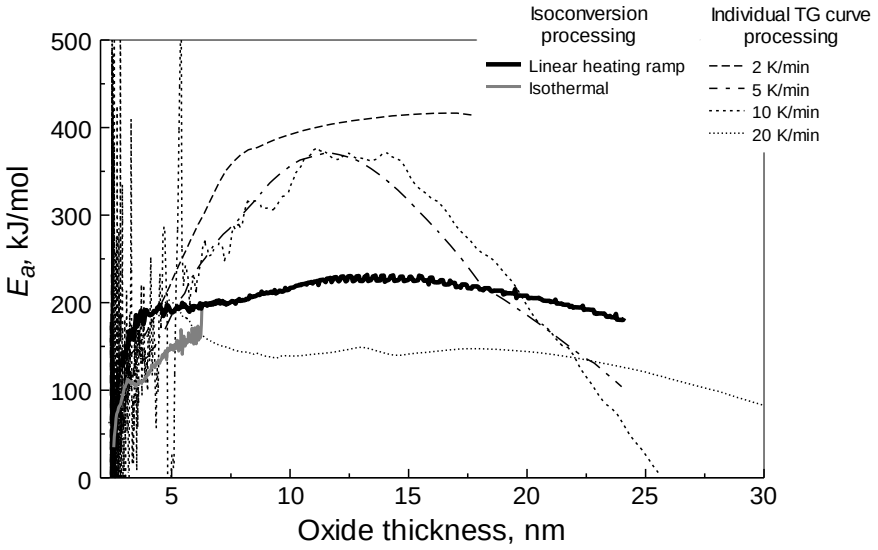

Figure 4.4 Activation energies of aluminum oxidation obtained by processing constant heating rate measurement and isothermal measurement using both explicit model and model-free isoconversion methods.

Figure 4.5 repeats the trend for activation energy obtained using model-free isoconversion processing for constant heating rate measurements shown in Figure 4.4 and shows respective trend for the pre-exponent *C*. The pre-exponent, *C*, was calculated using

the activation energy corresponding to the specific oxide thickness obtained the model-free isoconversion processing and then assuming the explicit oxidation model expressed by Equation (4.2). Not surprisingly, the calculated pre-exponent is a strong function of activation energy, E_a. Values of activation energy and pre-exponent varied as a function of the oxide thickness suggest that the reaction mechanism evolves as the oxidation continues. Identifying underlying detailed reactions causing changes in the apparent activation energy and pre-exponent are beyond the scope of this work. Instead, this effort is aimed to develop a simplified and practically useful quantitative description of aluminum oxidation, which can be employed in respective ignition and aging models.

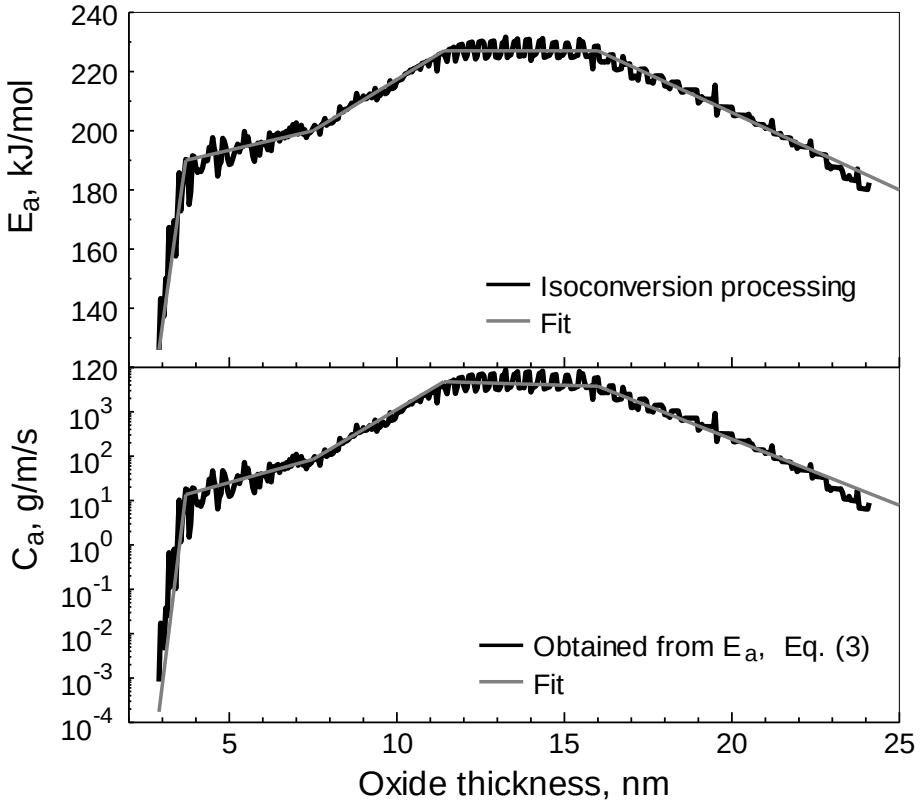

Figure 4.5 Activation energy and pre-exponent for aluminum oxidation calculated using constant heating rate measurements based on model-free isoconversion processing and explicit model, Equation (4.2), respectively.

For practical use of trends shown in Figure 4.5, simplified fits were obtained following somewhat noisy activation energy and pre-exponent traces calculated directly from experimental data. Somewhat arbitrarily, straight lines were fitted to different portions of the obtained traces. Note that straight line fits were applied to E_a and *log(C)*. The straight line fits as a function of the oxide thickness, *h*, plotted in Figure 4.5 are explicitly shown in Table 4.1. A Matlab code to calculate the early stage of oxidation of an aluminum powder using the reaction model given in Table 4.1 and accounting explicitly for the measured particle size distribution is given in supporting information.

Table 4.1 Activation Energy and Pre-Exponent as Functions of Oxide Thickness of Aluminum, h (nm). The Activation Energy is Obtained Using Model-Free Isoconversion Processing of Constant Heating Rate Measurements

Range of oxide thickness, nm	E_a, kJ/mol	$Log(C_a)$
2.4-2.9	60h-54	0.5h-5.44
2.9-3.4	87.5h-133.75	6.15h-21.5
3.7-7.5	3.42h+177.34	0.19h+0.44
7.5-11.4	6.15h+156.85	0.47h-1.64
11.4-16	227	-0.02h+3.93
16-25	-5.2h+310.56	-0.31h+8.48

In Figure 4.6 and 4.7, measurements and calculations are systematically compared. Figure 4.6a shows the constant heating rate measurements with calculated traces based on the kinetic parameters exclusively determined from isothermal measurements. Figure 4. 6b shows the same constant heating rate measurements with calculations based on (1) activation energy from constant heating rate measurements, (2) pre-exponent based on

single-curve processing, and the reaction model *f(α)* based on the geometric constraints of a rigid oxide shell, growing on its outer surface (cf. Figure 4.5 and Table 4.1).

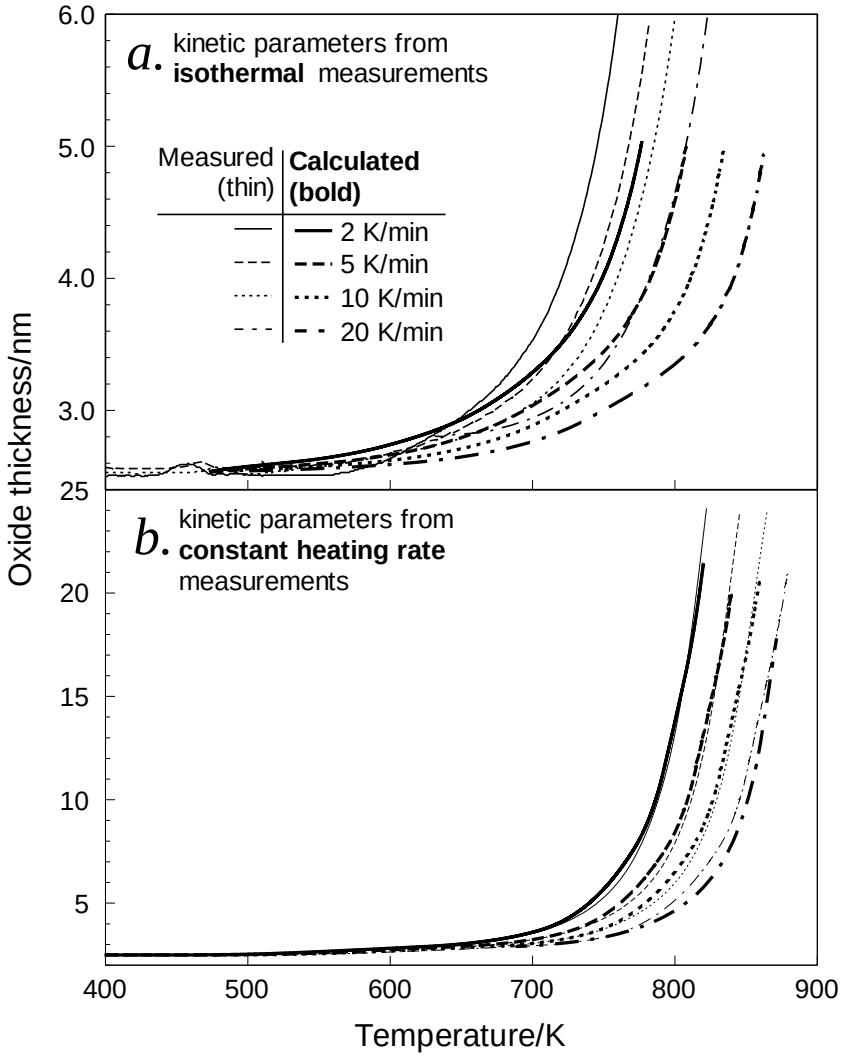

Figure 4.6 Aluminum oxide thickness as a function of temperature for constant heating rates. Thin lines represent measurements, bold lines show calculations. Calculations are based on kinetics derived from (a) isothermal measurements (b) constant heating rate measurements.

All results are plotted in terms of the aluminum oxide thickness as a function of temperature. The oxide is calculated for the particle with diameter 2.188 μm, equal to the surface area average diameter for the powder particle size distribution. The thin lines

represent the experimental data at different heating rates, and the bold lines represent the calculations. The match between the measured and calculated curves is good for all heating rates and for the entire range of temperatures and oxide thicknesses considered.

A comparison similar to that shown in Figure 4.6, but using constant temperature experimental data is shown in Figure 4.7. Thin lines represent TG traces measured at different temperatures and bold lines represent respective calculations. The match between the measurements and calculations is good for Figure 4.7a, but not for Figure 4.7b, although calculations are generally following measurements at lower temperatures, and for thinner oxide layers. At higher temperatures, the calculated thickness systematically exceeds the experimentally observed thickness.

The discrepancies observed in Figures 4.6a and 4.7b are likely explained by shortcomings in both types of measurements, isothermal as well as linear heating. Due to the relatively large sample mass (about 100 mg, chosen to achieve good mass resolution at low degree of oxidation), the oxidation in the isothermal measurements is slower because of uneven exposure of the powder to oxygen. Although the measurements were conducted essentially in pure oxygen, the samples were initially heated to the target temperature in argon. Oxygen flow was turned on only after the temperature had stabilized. Therefore, as the argon in the pore space of the sample slowly diffuses out, there likely is a concentration gradient in the pore space of the whole sample, exposing the lower/inner parts of the sample to a significantly lower oxygen concentration than the target atmospheric composition. The removal of argon from the pore space would be further hindered by the Stefan flow of the oxygen. This problem would become more pronounced at higher temperatures, higher reaction rates, and therefore higher oxygen consumption rates. The

measured rate of mass increase could become limited by diffusion of oxygen through the porous sample. As a result, the mass increase for the entire sample is lower than it would be if all the powder was exposed to the same oxidizing environment. The result of the kinetic processing would then yield activation energy and pre-exponent that are too small relative to those obtained from constant heating rate measurements. Additional isothermal experiments were performed at a selected temperature where the mass was systematically varied, leading to increasing diffusion distances required to saturate the pore space with oxidizer. These measurements are included in the supporting information. Results confirm that the oxidation rate is lower for larger sample masses and at longer times. At the same time, measurements with lower masses show strong experimental noise at the beginning of the exposure to oxygen, and thus are difficult to use to investigate the very early stages of oxidation.

Alternatively, sample self-heating could pose an experimental problem for the constant heating rate experiments. If the heat flow within the loosely packed powder sample is too low, and the heat of the oxidation reaction causes a temperature gradient to develop in the sample, then the actual temperature of part of the sample could be higher than what is recorded. This is hard to quantify. In some measurements this effect can be seen from a plot of the difference between the actual sample temperature and the programmed sample temperature vs. time. However, the sample temperature is used by the TG to control the heating elements, and therefore observing no deviation of the net sample temperature from the programmed temperature does not mean that there are no temperature gradients in the sample. Since the heat exchange between the sample and the environment occurs at the surface of the sample, a lower sample mass, and therefore a higher specific

surface area should minimize internal gradients. In addition, gradients are likely to be stronger for higher heating rates and higher oxidation rates. The measurement at 20 K/min was therefore repeated with a sample mass of about 2 mg (vs. about 20 mg used here) in order to investigate the effect. These additional measurements are also presented in the supporting information. At the peak of the oxidation rate, the result can be interpreted as showing an effective sample temperature that is about 10 K higher if the sample mass is 20 mg than for the 2 mg sample, making the recorded temperature, which is used in the isoconversion analysis, too low. The difference becomes impossible to resolve at lower temperatures, lower oxidation rates, and therefore lower oxide layer thickness. We estimate that the measurement at 20 K/min may be biased as the oxide thickness approaches 20 nm. Lower heating rates and lower oxide thicknesses are not affected.

Therefore, kinetic data recovered from constant heating-rate measurements were subject to fewer experimental problems, especially at lower oxide thickness, and preferred for subsequent calculations. To validate the kinetic parameters, different published datasets characterizing oxidation of aluminum were compared to predictions obtained using reaction kinetics implied by both isothermal and constant heating rate measurements. As mentioned below, such comparisons further supported selection of reaction kinetics obtained from constant heating rate measurements as more reliable.

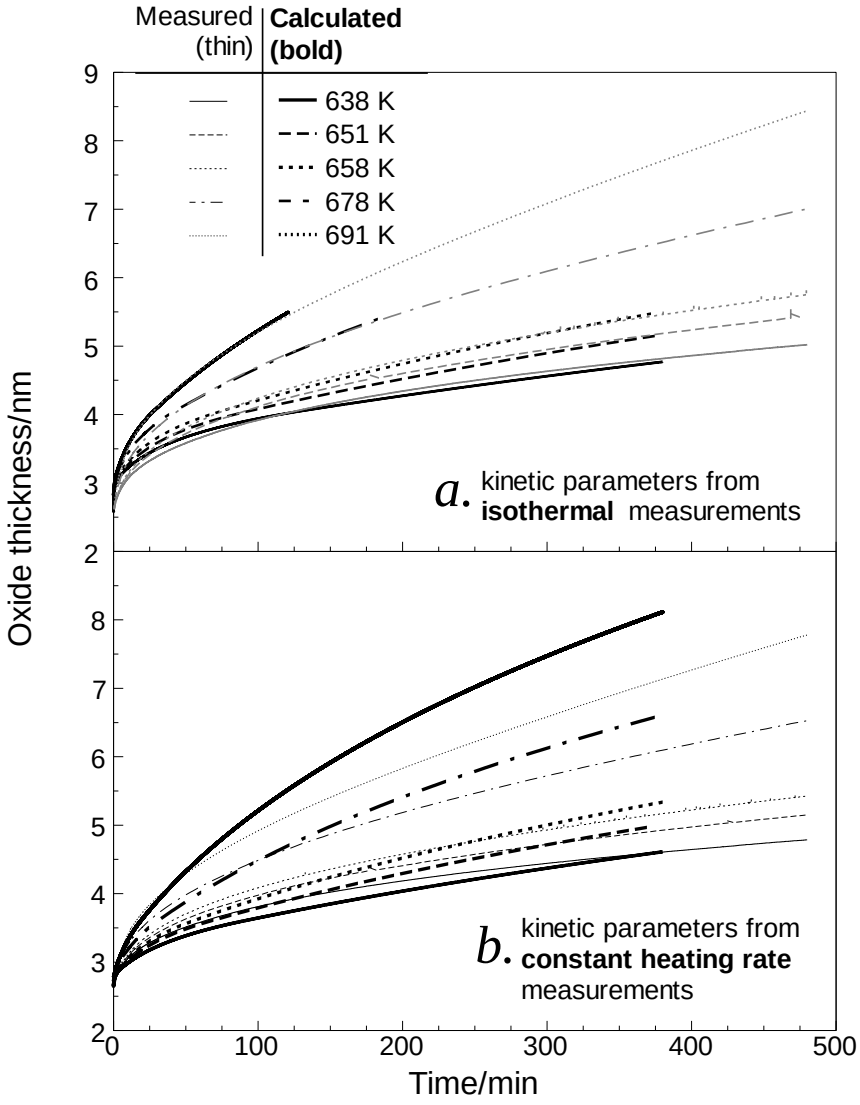

Figure 4.7 Aluminum oxide thickness as a function of time at constant temperatures. Thin lines represent measurements, bold lines show calculations. Calculations are based on kinetics recovered using (a) isothermal measurements (b) constant heating rate measurements.

4.6 Validation of the Oxidation Model

A simplified description of aluminum oxidation given in Table 4.1 is used in this section to interpret the earlier reported experimental data. Specifically, data sets reported for

nano-sized aluminum powders are selected, for which the effect of aluminum oxide thickness on the measured oxidation rate is expected to be most pronounced. Further, experimental data sets were found for which specific powder PSDs were reported, as is necessary for the present calculations.

Aumann et al., [98] reported oxidation behavior for ultrafine aluminum powders. Both the PSDs and initial oxide thicknesses were specified. The PSDs were obtained from high-resolution transmission electron microcopy and described using log-normal functions.

Aumann et al., [98] performed isothermal TG measurements for two powder samples at different temperatures. Comparisons with respective calculations for sample C (163 nm for the PSD peak) are shown in Figure 4.8.

All data are shown in terms of the relative powder mass. The bold lines represent calculations and thin lines show measurements. At lower temperatures, 523 and 573 K, the calculated traces follow the experimental data well. However, at higher temperatures, the discrepancies between calculated and experimental traces increase and become significant. Similarly to the comparison shown in Figure 4.7b, the oxidation rates are substantially over-predicted for higher temperatures. It is possible that, as discussed above for Figure 4.7, this discrepancy is also caused by the lack of oxidizer access to the entire powder sample when the temperatures in experiments increased and the oxidation rates became higher. Conversely, particle sintering and corresponding loss of free surface area cannot be ruled out.

Applying kinetics inferred by the isothermal measurements under-predicts the reaction rate observed at low temperatures (results are omitted for brevity). This

discrepancy is consistent with the discussed above limitation of the reaction rate in isothermal measurements caused by diffusion of oxygen through the sample pores.

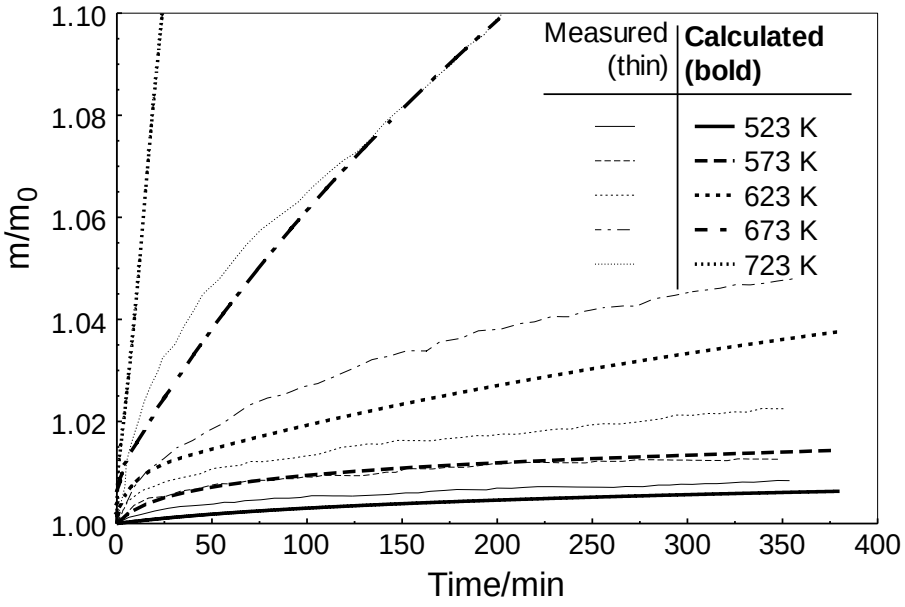

Figure 4.8 Measured isothermal TG traces (sample C, [98]) and traces calculated using kinetics shown in Table 4.1 for respective temperatures.

Thermogravimetric measurements at constant heating rate were previously reported by our group [99] for the oxidation of nano-sized aluminum powders. The particle sizes obtained processing BET measurements and assuming the powders to be monodisperse spheres for the three powders studied were 44, 80 and 121 nm, respectively. Corresponding small-angle X-ray scattering (SAXS) measurements showed crystallite size distributions [99]. Actual particle size distributions were not available. Data on the initial oxide thickness for each powder were also unavailable. For preliminary comparison, the SAXS results were interpreted as particle size distributions, and all powders were assumed to have an initial oxide thickness of 4 nm[93, 100, 101] (rather than 2.5 nm used for micron powders, because a thicker initial oxide layer is expected and usually observed, [102] to

form for nano-sized powders, which self-heat more during their passivation in an oxidizing environment). Resulting calculated TG traces are shown together with those measured in Reference [99] in Figure 4.9a. The calculations used kinetics from Table 4.1. The heating rate for all curves is 5 K/min. Solid lines show measurements and dashed lines show calculations. All calculations substantially overestimate the oxidation rates.

One likely reason for the observed discrepancy is that the SAXS-based crystallite size distributions systematically underestimate the actual particle sizes. The resulting apparent loss of surface area available for oxidation can be accounted for in calculations by describing the actual particles, which comprise multiple crystallites, as hard agglomerates, or aggregates. In addition, agglomerates of nanoparticles due to Van der Waals forces can reach tens or hundreds of micrometers in size [103-105], also substantially decreasing the specific surface area available for oxidation. Agglomeration for nano-aluminum powders was specifically reported to occur in Refs. [106, 107]. For these reasons, a nominal agglomeration factor was used in the following calculations as an adjustable parameter. A similar agglomeration factor was introduced in Reference [108]. In the present work, the volume fraction of each particle size bin in the agglomerated PSDs was assumed to remain consistent with the SAXS measurements. Agglomerated particle sizes were generated by multiplying the original particle size obtained from SAXS by the agglomeration factor. Figure 4.9b shows that with this procedure, the calculated TG curves can be matched to the experimental ones using agglomeration factors of 2.2, 2.5 and 5.5 for the powders with average BET sizes of 44, 80 and 121 nm, respectively.

The agglomerated particle sizes should more accurately reflect the surface area available for oxidation, and should therefore be compared to the nominal BET average

particle sizes. The powders with BET sizes of 44, 80, and 121 nm have surface-averaged agglomerated particle sizes of 69, 122, and 305 nm, respectively which corresponds to an apparent specific surface area of 64 %, 66 %, and 40 % of the corresponding values measured by BET. These values are comparable considering that a single agglomeration factor cannot distinguish between hard aggregates of crystallites, and loose agglomerates of particles. Any remaining discrepancies can be rationalized by progressive sintering during oxidation.

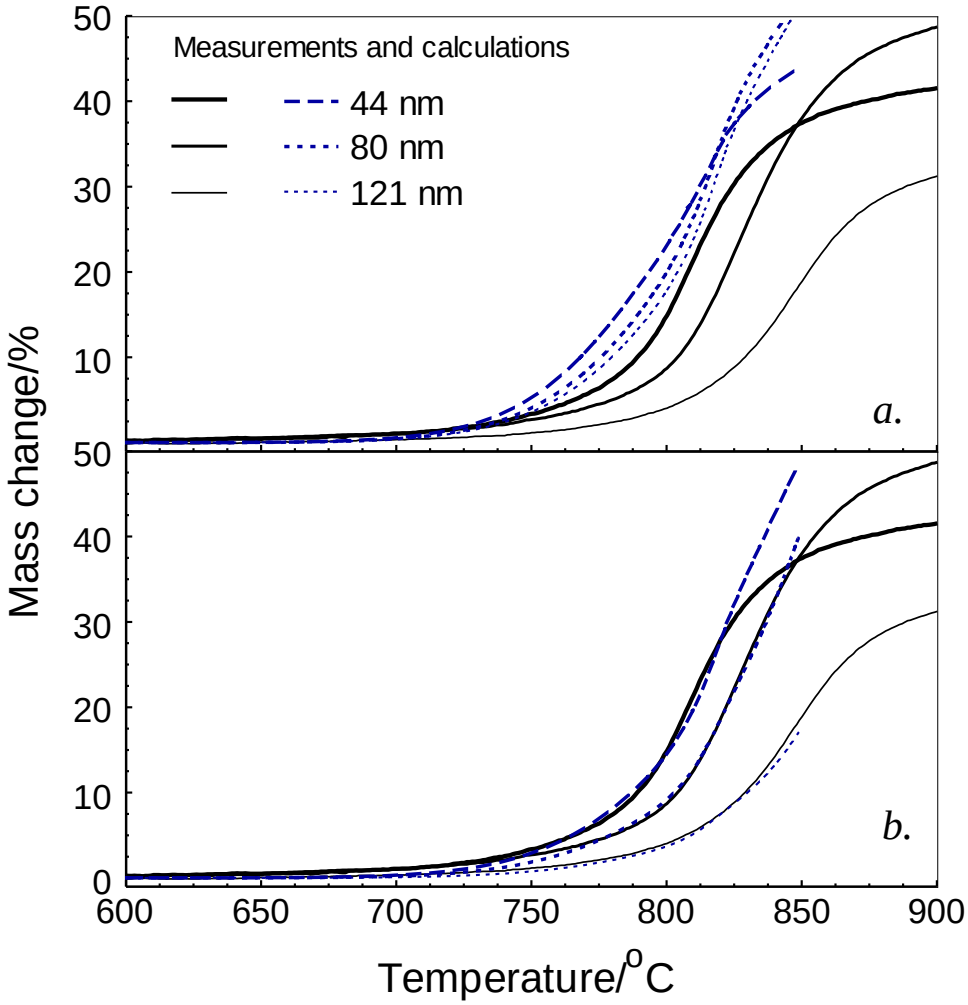

Figure 4.9 Measured [99] and calculated TG traces for three aluminum nanopowders for a heating rate of 5 K/min; (a) interpreting SAXS measurements as PSD (b) adjusted PSD using agglomeration factor.

Once the appropriate nominal agglomeration factor was found for each powder, additional calculations were performed for a heating rate of 1 K/min, for which experimental data were also reported in Reference [99]. Results as well as experimental data are shown in Figure 4.10. Calculations performed using previously reported oxidation kinetics [31]are also shown for side-by side comparison with the current, corrected model. Note that the calculations using kinetics from Reference [31] are extended to describe growth of γ-Al_2O_3 at a greater oxide thickness. The current calculations, however, were limited by growth of thin layers of amorphous alumina. The model can be readily extended to describe growth of other alumina polymorphs as discussed below, when it is applied to describe aluminum powder ignition.

Results of the present calculations match equally well the experimental data for all powders for both heating rates. Importantly, both the rate of oxidation as a function of temperature and the shift of the measured TG curves as a function of heating rate are well described. Conversely, calculated curves from Reference [31] are only describing general shapes of the TG traces; however, the details are not well reproduced. Both calculated curves reported in Reference [31] shift systematically from under-predicting to over-predicting the oxidation rates when the particle sizes increase (cf. respective curves in Figure 4.10 a vs. b vs. c). The increase in slope of the experimental TG curves observed at increasing temperatures in each experiment is not predicted well either; calculations [31] predict a slower increase in the oxidation rate.

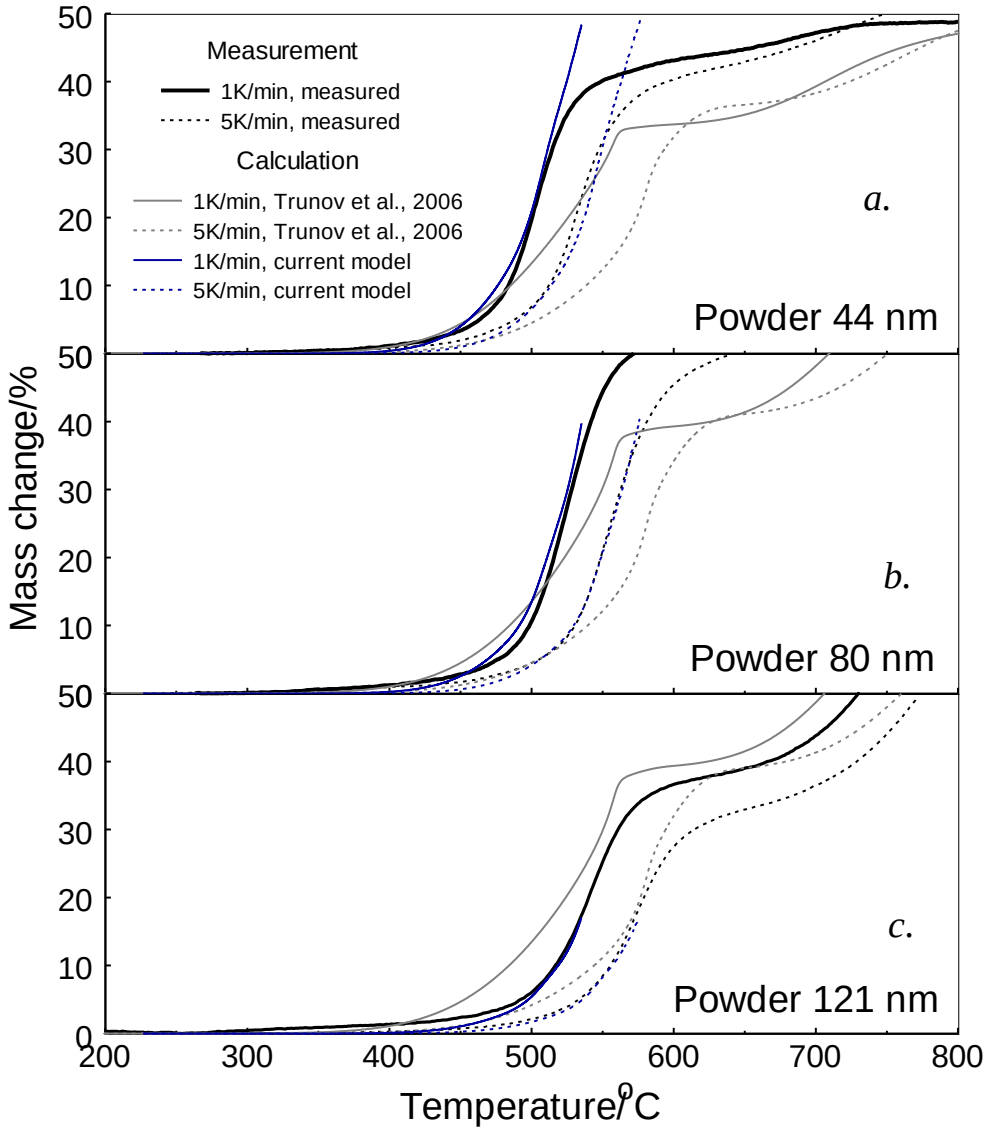

Figure 4.10 Measured[99] and calculated TG traces for two heating rates for three aluminum nanopowders. Calculations performed using kinetics described in Table 4.1 and using earlier model [31].

4.7 Ignition of Aluminum Powders

An ignition model for a single aluminum particle introduced in a hot oxidizing gas was previously described in Reference [31]. In that model, the ignition temperature was defined as the gas temperature at which an initially cold particle is predicted to self-heat in excess

of the melting temperature of alumina, 2345 K. The same criterion for ignition temperature was adopted here.

The general approach for describing particle temperature history used in Reference [31] is retained here. However, two substantial changes are made in the model. Heat transfer between the particle and environment was described in Reference [31] considering convection with Nusselt number Nu=2. Instead, transition heat transfer is used in the present paper, suitable for particles with dimensions comparable to the mean free path of gas molecules. Details of the present transition heat transfer model are available in the [109, 110]. The heat transfer was analyzed for conditions employed in experiments [111].

The second modification concerns the specific reaction model for oxidative growth of amorphous alumina. The present reaction kinetics described in Table 4.1 is used. The reaction is considered to occur outside of the growing rigid oxide layer following Reference [91]. The Matlab code used for calculations of the particle temperature history as well as tracking thicknesses of the growing alumina polymorphs is available as Supplement 4.2.

A summary of calculated ignition temperatures as a function of the particle size is shown in Figure 4.11. Experimental data points from Reference [111]are shown for comparison as well as a calculated curve reported earlier [31], which did not account for the transition heat transfer and modifications in the oxidation kinetics for amorphous alumina obtained in the present work. The present calculations suggest that nano-sized particles can ignite at an even lower environment temperature than predicted previously. Conversely, the ignition temperature for coarser particles was somewhat under-predicted in Reference [31]. Experimental data show an increase in the ignition temperature as a

function of the particle size, qualitatively in agreement with the present predictions and with earlier results, e.g., see summary in Reference [86]. However, the experimental ignition temperatures are higher than predicted for the finest particles and lower than predicted for coarser ones. A likely interpretation for this discrepancy is that experiments never use truly monodispersed particles. Ignition is registered in shock tube experiments, such as in Reference [111] by an optical emission increased above the background lever. Such emission may be dominated by coarser particles, when the nominal particle size is very small; conversely, for nominally coarser powders, fine fraction can ignite sooner and assist in ignition of nearly coarser particles.

The predicted ignition temperatures depend on assumed initial thickness of the oxide layer; they may also be affected by the value of thermal accommodation coefficient used in the transition heat transfer model and quantifying efficiency of energy exchange between gas molecules and particle surface. The sensitivity of the predicted ignition temperatures to the above two parameters was considered. Predicted ignition temperatures for particles of different sizes with different initial oxide thickness are shown in Figure 4.12. It is observed that the ignition temperatures increase significantly with thicker initial oxide layers for aluminum nano-particles; however, for the coarser particles ($\geq$0.5 μm) the ignition temperatures almost do not change. Typically, the initial oxide thickness is only known approximately; thus, an oxide layer thicker than 2.5 nm for the nano-particles powders used in experiments from Reference [111] would help explain a higher experimental ignition temperature than currently predicted.

The thermal accommodation coefficient used in calculations was taken as equal to one. However, several studies, e.g. [112, 113], suggest that this coefficient may be

substantially smaller. To test sensitivity of the present predictions, the accommodation coefficient was reduced by an order of magnitude, to 0.1. The predicted ignition temperature became lower, but the effect was different for particles of different sizes. The effect was most significant for particles with sizes close to 0.5 μm, for which the ignition temperature was reduced by 180 K compared to that shown in Figure 4.11. Only minor reduction of 50 and 10 K, in the predicted ignition temperature was observed for the particle sizes closed to 100 nm and 1 μm, respectively.

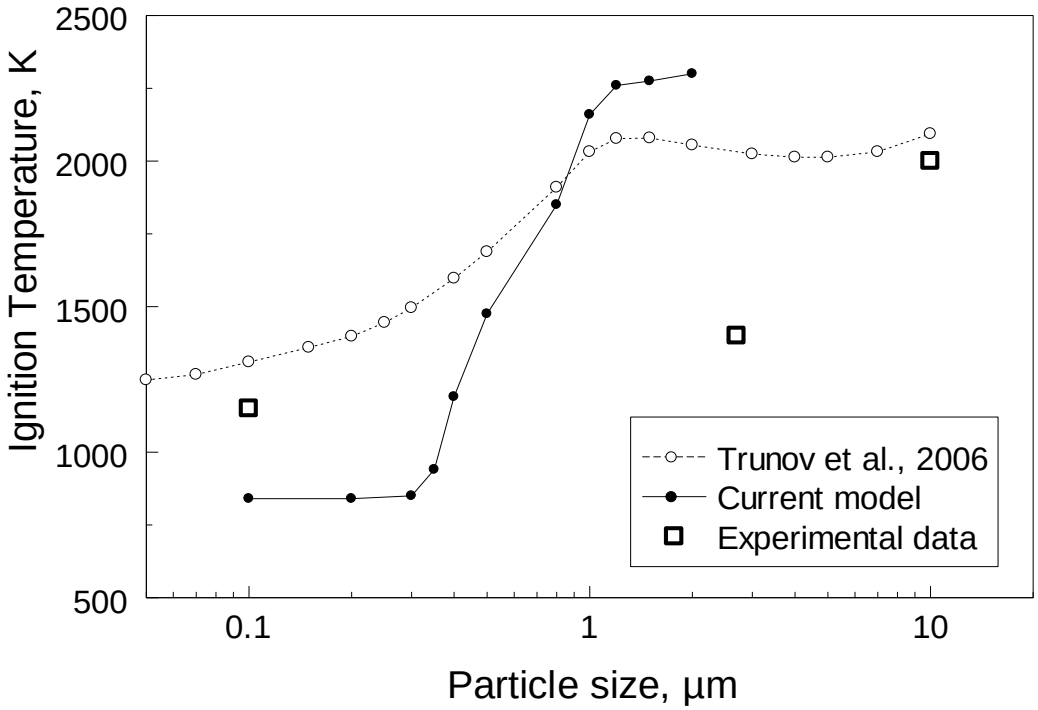

Figure 4.11 Ignition temperatures for aluminum particles of different sizes exposed to a heated oxidizing environment. Experimental data are from Reference [111]; earlier calculations are from Reference [31]. For present calculations, initial oxide thickness is assumed to be 2.5 nm; thermal accommodation coefficient equal to 1 is used in the transition heat transfer model.

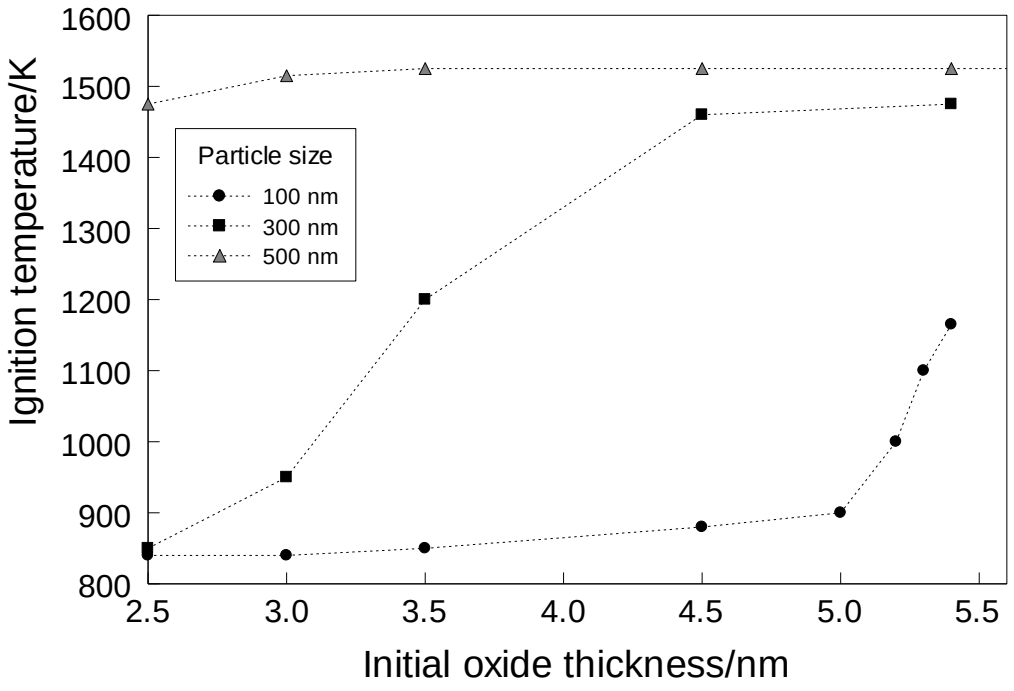

Figure 4.12 Predicted ignition temperatures for aluminum particles of different sizes with different initial oxide thickness exposed to a heated oxidizing environment. Thermal accommodation coefficient is taken to be equal to 1.

To better understand which specific oxidation processes cause ignition for Al particles of different sizes, results of calculations are illustrated in Figures 4.13, 4.14, and 4.15 for particles with sizes 0.3, 0.5, and 1 μm, respectively. The plots show evolution of the particle temperature in time and thickness of amorphous and γ-Al_2O_3 layers, as well as the total oxide layer thickness. For all plots, the time scale is limited to 100 μs, although the calculations for non-ignited particles continued for 100 ms, to ensure that no additional temperature peak was predicted. Ignited and non-ignited particles for each size are illustrated respectively with traces shown in the left and right sides of Figures 4.13-4.15. Dashed lines in temperature plots represent the temperatures of the surrounding environment. For each case, the difference between ignition and non-ignition is estimated

with the accuracy of 5 K in terms of difference between respective environment temperatures.

Each calculated temperature history includes an initial temperature increase up to the environment temperature or up to the aluminum melting point, during which the growth of the oxide layer thickness is negligible. This is followed by a temperature plateau, corresponding to the surrounding temperature and/or aluminum melting. During this temperature plateau, substantial part of the amorphous Al_2O_3 transforms into γ-Al_2O_3 polymorph. For all cases, calculations predict that the newly formed γ-Al_2O_3 does not fully cover aluminum surface because it has higher density than the original amorphous oxide and because the original alumina thickness does not exceed the size of the forming γ-Al_2O_3 crystallites. Thus, as reported earlier [31], oxide becomes porous and the model accounts for the ensuing oxidation as limited by gas diffusion of the oxidizer to the open pores at the particle surface. This causes rapid increase in the particle temperature, which is marked in Figures 4.13-4.15. However, this increase is insufficient to cause ignition for any particle size considered. Once the open pores are closed, the model considers diffusion resistance of the newly formed γ-Al_2O_3. Initially, its diffusion resistance is small because of remaining porosity; the oxide is allowed to "heal" attaining the usual, higher diffusion resistance of a polycrystalline material. Interestingly, for all particle sizes, ignition occurs during this "healing" process considered in the model. Smallest particles ignite almost immediately when the healing of γ-Al_2O_3 begins. Conversely, larger particles are predicted to ignite when γ-Al_2O_3 is nearly fully healed. If the environment temperature is reduced, the oxide will be fully healed and the reaction continues at a much slower rate, insufficient to cause ignition.

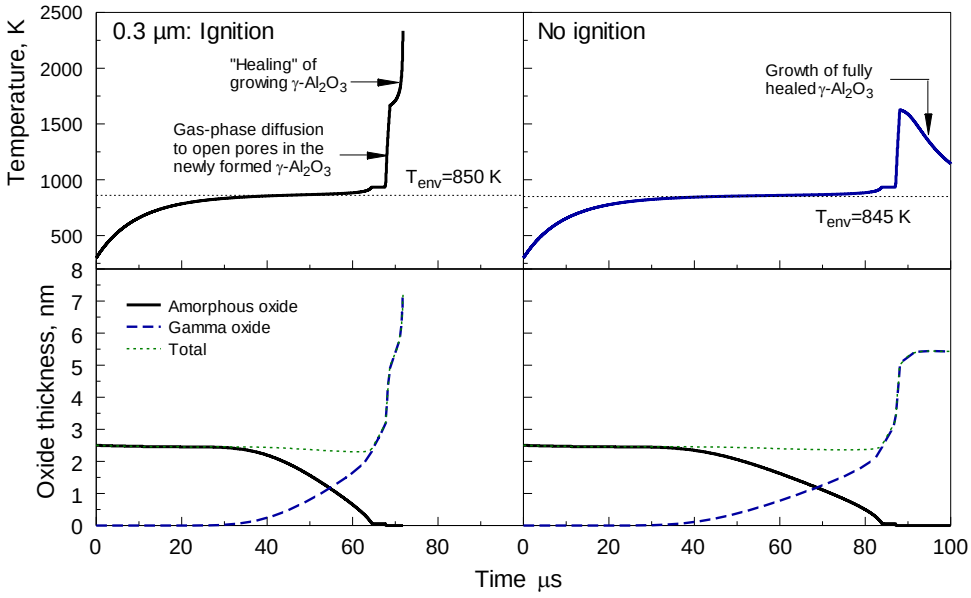

Figure 4.13 Temperature histories and thicknesses of different Al_2O_3 polymorphs forming on surface of a 0.3 μm diameter aluminum particle exposed to a heated gas surrounding at 850 (left) and 845 K (right).

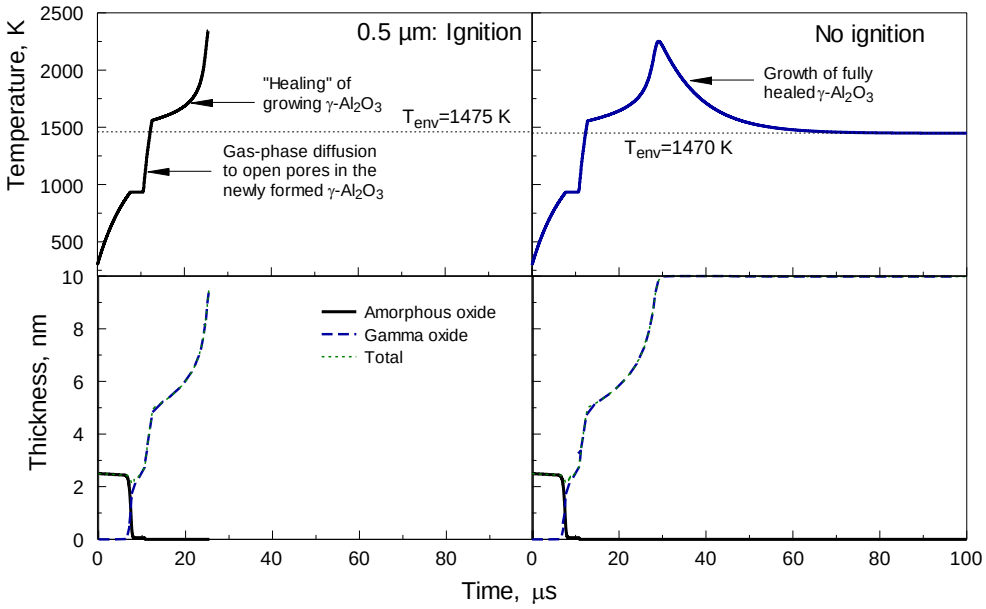

Figure 4.14 Temperature histories and thicknesses of different Al2O3 polymorphs forming on surface of a 0.5 μm diameter aluminum particle exposed to a heated gas surrounding at 1475 (left) and 1470 K (right).

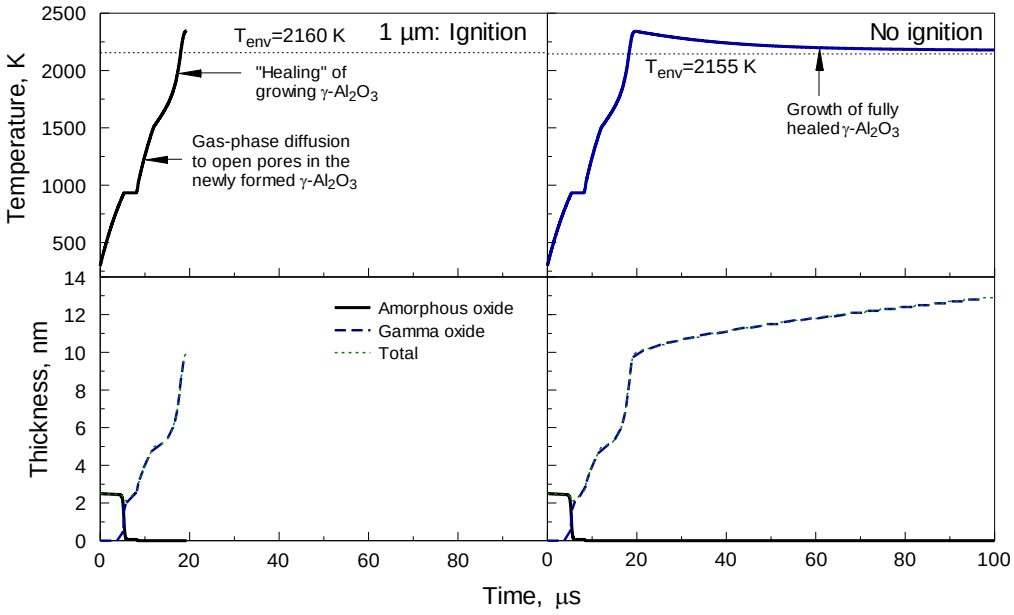

Figure 4.15 Temperature histories and thicknesses of different Al2O3 polymorphs forming on surface of a 1 μm diameter aluminum particle exposed to a heated gas surrounding at 2160 (left) and 2155 K (right).

4.8 Conclusions

Thermo-gravimetric measurements with large amounts of fine aluminum powders are useful in obtaining detailed information on their oxidation kinetics at low temperatures. However, restricted access of oxidizer to the powder for increased powder load can also cause misleading TG measurements, during which different portions of the sample react with different rates. Constant heating rate measurements were most useful in establishing reaction kinetics for aluminum powders at low temperatures and reduced oxide thickness. The activation energy as a function of reaction progress was obtained using a model-free isoconversion processing of experimental data. Once the activation energy was obtained, an explicit oxidation model assuming reaction occurring at the outside of a rigid spherical layer was considered to determine the pre-exponent as a function of the reaction progress.

Therefore, both activation energy and pre-exponent were obtained as functions of the reaction progress expressed, for convenience, through the oxide layer thickness. The oxidation model was compared with the present and previously reported data on oxidation of fine aluminum powders; the match between experiments and calculations is satisfactory. For nano-powders, agglomeration is accounted for, and the results illustrate that this is essential for accurate calculation of oxidation rate. The oxidation model was combined with description of heat transfer for an aluminum particle exposed to a heated oxidizing environment. Thus, a model describing particle ignition was obtained and compared to earlier predictions and recent experiments. The model predicts a sharp rise in the ignition temperature from 850 to 2260 K for particles with sizes increasing respectively from 0.3 to 1.2 μm. The specific results are affected by the assumed initial oxide thickness (2.5 nm) and thermal accommodation coefficient (taken as 1). The experiments show an increase in the ignition temperature; however, this increase may be more gradual than predicted in the model. The discrepancy between predictions and measurements is most likely due to a relatively broad particle size distribution for the powders used in experiments and a difficulty to identify which size sub-range of the heated particles ignites at the threshold temperature.

CHAPTER 5

OXIDATION OF MAGNESIUM: IMPLICATION FOR AGING AND IGNITION

5.1 Abstract

Magnesium is widely used in pyrotechnic formulations; it is also a component of reactive alloys, e.g., Al-Mg and B-Mg, which are potential fuels for explosives and propellants. Despite its widespread applications, kinetics of oxidation of Mg powders are not well quantified. Such kinetics are of fundamental importance for the models aimed to describe thermally induced ignition of metal powders. In addition, for Mg the issue of aging is important because its oxide, MgO is porous. In this work, magnesium oxidation by both oxygen and steam was studied by thermo-analytical measurements for micron-sized spherical powders. Heat flow calorimetry and thermogravimetric were used to quantify reaction rates for low and elevated temperature ranges, respectively. Experiments with spherical powders with different but overlapping particle size distributions were used to identify the location of the reaction interface. The reaction was found to occur at the interface of metal and the growing oxide layer for all oxidizing conditions. The reaction is thus rate limited by diffusion of oxidizer to the metal surface. Kinetics of oxidation for both dry and humid oxidizing environments were quantified using thermo-analytical measurements and different data processing techniques. Activation energy of magnesium oxidation in humid environments at low temperatures is close to 60 kJ/mol. Activation energy for oxidation of magnesium in oxygen is 148 kJ/mol. For oxidation of magnesium in steam at elevated temperatures, the activation energy increases linearly from approximately 130 to 360 kJ/mol, while the forming oxide layer thickens up to 2.4 μm. Simplified diffusion-limited reaction models were developed for oxidation of magnesium

in both oxygen and steam. The models enable one to predict both pre-ignition reactions occurring upon heating of Mg particles and the time of Mg powder aging when exposed to moisture or oxygen at different temperatures.

5.2 Introduction

Magnesium is widely used in pyrotechnic formulations and other energetic materials [114-116]. It is also well-known that magnesium powders are prone to aging, in particular in humid environments [117, 118]; however, we were unable to find references describing this aging quantitatively. Two main oxidation products form during oxidation of magnesium: magnesium hydroxide, $Mg(OH)_2$, and magnesium oxide, MgO. In low-temperature, humid environments, magnesium hydroxide forms as a result of hydration of a naturally grown thin MgO film uniformly adhering to the Mg metal core [119, 120]. Multiple studies characterized the respective bilayer structure including a relatively dense layer of $Mg(OH)_2$ on top of a porous layer of MgO [121, 122]. As the temperature reaches or exceeds the range of 280 – 450 ºC, and depending on the partial pressure of water, $Mg(OH)_2$ decomposes, resulting in growth of thicker MgO films [123, 124].

Low-temperature rates of formation of layers of oxidized magnesium need to be known in order to develop handling guidelines for or predict the lifetime of magnesium powders stored under different conditions or included as components in a composite structure. The rates of reaction at elevated temperatures become important for predicting ignition behavior of magnesium and related energetic systems. Additionally, kinetics of magnesium oxidation may serve as a useful reference for assessments of reactivity of

alloys employing magnesium, e.g., Al·Mg alloys prepared by mechanical milling for advanced energetics [36, 125, 126].

The work is aimed at characterizing oxidation of Mg powders experimentally in both dry and humid gas environments. Separate experiments address different temperature ranges. Location of the reaction interface is first established. Reaction rates are then quantified.

5.3 Experimental

5.3.1 Material

Spherical magnesium powder with a nominal size of -325 mesh, and 99.8% purity was provided by Magnesium Elektron. This powder was passed through a 550 Mesh (25 μm opening) sieve to obtain coarse (as received) and fine fractions for high-temperature oxidation measurement in oxygen and steam. The actual particle size distributions for both size fractions were measured using a Beckman-Coulter LS230 Enhanced Particle Analyzer. Results are shown in Figure 5.1. For low-temperature oxidation measurements, in order to obtain a more distinguishable discrepancy between the reaction progresses of two size fractions, an even finer size fraction was prepared by passing the as-received powder through a 650 mesh (20 μm opening) sieve. Sieving was carried out using ASTM certified 12-inch test sieves by Advantech Manufacturing. Powders were placed on the sieves in an argon-filled glove box, and shaken by hand for several minutes. It was only necessary to obtain small quantities with sufficiently different size distributions. Complete size separation was not needed, and therefore not attempted.

A common feature for all pairs of coarse and fine powder fractions was that, as shown in Figure 5.1, there was an overlap between the particle sizes, which was necessary for data processing. For brevity, only one pair of size distributions is shown here.

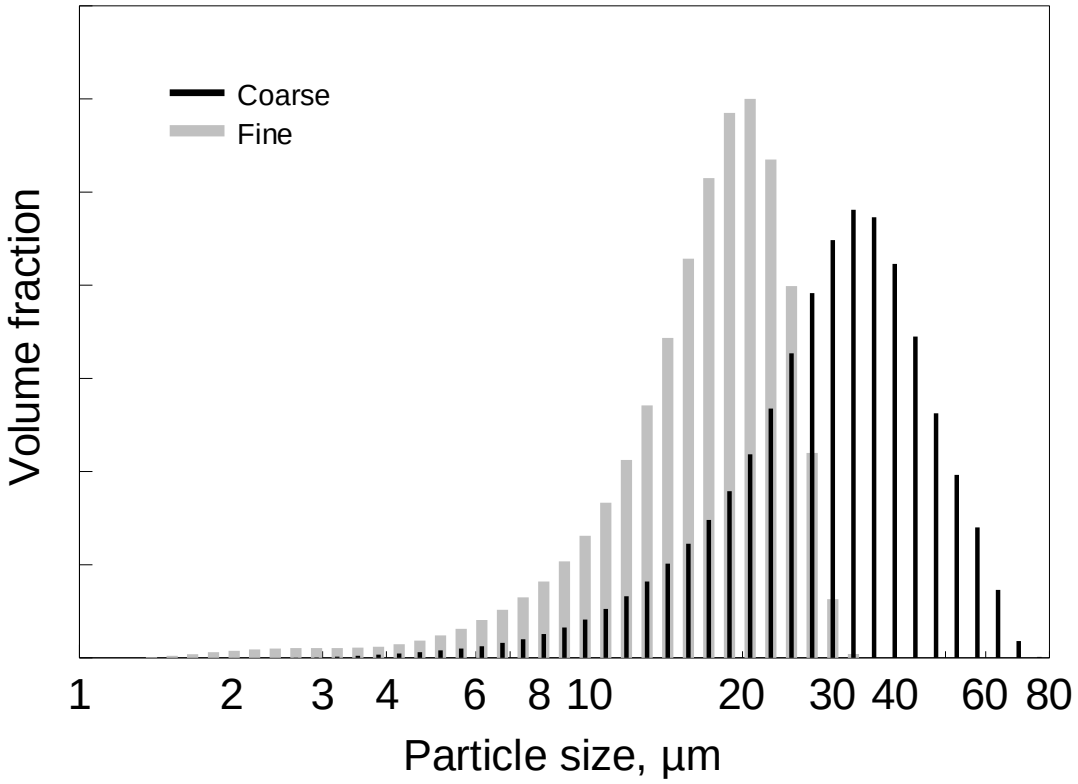

Figure 5.1 Particle size distributions for coarse (as received) and fine fractions of the spherical magnesium powder used in experiments.

5.3.2 Thermo-Analytical Measurements

Magnesium oxidation was studied in two temperature ranges and using two oxidizers. For temperatures in the range of 40 – 80 °C, oxidation in a humid gas flow was studied using a TAM III calorimeter by TA Instruments. A perfusion ampoule was used, enabling calorimetric measurements for samples subjected to a controlled gas flow with defined humidity or vented to the surroundings. Measurements were carried out at 313, 333 and 353 K (40, 60 and 80 °C, respectively). Samples were contained in 4-mL steel reaction vessels. Samples were weighted and loaded in the reaction vessel, the reaction vessel was

then attached to the perfusion ampoule, and the perfusion ampoule was inserted into the calorimeter. The perfusion ampoule was flushed with a regulated air flow at 50 mL/h. The relative humidity was controlled by varying the percentage of wet and dry air flows through a humidifying water reservoir.

Oxidation in steam and oxygen at higher temperatures, from 350 to 650 ºC, was studied using a Netzsch STA409PC/PG thermal analyzer using a thermogravimetric sample carrier with a 17 mm diameter flat corundum sample plate. Thermogravimetric (TG) traces were recorded.

In preliminary experiments, oxidizing magnesium in a dry oxygen/argon mixture, and using the general-purpose SiC furnace of the STA409PC, magnesium evaporation posed a serious problem. In this configuration, the gas flow in the furnace rises vertically from the bottom, creating a wake downstream of the sample carrier. Gas mixing in this wake is poor; oxygen is being consumed by the sample, while argon is not effectively flushed out. This causes an environment with a relatively low oxygen partial pressure immediately surrounding the sample, leading to noticeable magnesium evaporation as the temperature reaches 500-600 ºC. This causes a number of problems ranging from contamination of the furnace, to unrealizable sample mass during the measurement, to ignition and formation of a magnesium vapor flame above the sample. In order to avoid these problems, the water vapor furnace of the STA409PG was used in experiments with both steam and oxygen as oxidizers. In this furnace, the oxidizer flows from the top of the furnace down to the sample. This flow pattern ensured that the gas surrounding the sample always had the set concentration of oxidizer, which minimized evaporation of the heated magnesium.

For the measurement with steam, the furnace was connected to a pressurized boiler, which was held at 180 °C. The steam was supplied to the furnace through a heated connecting line maintained at least at 150 °C to prevent condensation. Argon (Ultra-pure by Airgas) was introduced into the furnace in two locations. The first and invariant gas flow of 50 mL/min served to protect the thermobalance from any condensation. It entered the furnace from below. Due to the furnace geometry, it had a negligible contribution to the gas environment that the sample was exposed to. The second argon flow was used as a carrier gas for steam, entering the furnace from above; its flow rate was set to 166.7 mL/min, which converted to 253.4 mL/min at 180 ºC, the temperature at which steam was produced. Steam was supplied at 13.8 mL/min, generating an argon flow with 5% of steam fed to the sample.

For dry oxidation experiments, oxygen (Ultra-pure by Airgas) was used. The gas flow configuration was similar to that used in measurements with steam: argon was introduced as a protective gas around the thermobalance. It was also mixed with oxygen and flushed through the furnace. The argon flow rates were 50 and 90 mL/min, respectively. The oxygen flow rate was 10 mL/min to ensure that 10% of oxygen in argon was supplied to the sample.

5.4 Results and Discussion

5.4.1 Reaction Interface for Magnesium Oxidation

A method locating the reaction interface described in detail in Refs. [92, 127] was employed for oxidation of magnesium. Briefly, two size fractions of a spherical powder are reacted in the same environment following the same temperature program. The size

distributions for the two powder fractions are distinctly different, but contain an overlapping range of particle sizes. It is assumed that the particles with the same sizes will oxidize in the same fashion in both powder fractions. Different reaction scenarios placing the reaction interface at different locations are initially considered, as illustrated in Figure 5.2. In all cases, a core-shell geometry is assumed for oxidation of spherical particles. For each reaction scenario, the reaction rate is assumed to be proportional to the reaction interface area. This area is continuously changing while the reaction is progressing. For case a in Figure 5.2, the reaction interface area shrinks, while for cases b and c, it increases. In case a, reaction occurs at the metal/product interface; for cases b and c the reaction occurs outside of the forming product shell. In case b, the shell is assumed to be ductile, and its internal radius r shrinks when the metal core is diminished. In case c, the shell is rigid and its internal radius r remains constant; thus, a void can form in the reacting particle.

Taking into account the measured particle size distributions shown in Figure 5.1, it is possible to distribute the change in mass measured in a thermogravimetric experiment among all particles, based on their diameter and an assumed reaction model, e.g., a, b, or c in Figure 5.2. This distribution will change continuously during the experiment, because of continuous changes in radii r and R (Figure 5.2). Thus, an individual oxidation curve can be obtained for each specific original particle size, which will differ for different reaction models. When the model selected represents the actual process, these individual oxidation curves should be identical for the particles of the same sizes but belonging to different size distributions. Comparison of such curves, and finding the reaction scenario providing the best match between them leads to the selection of the most appropriate reaction model.

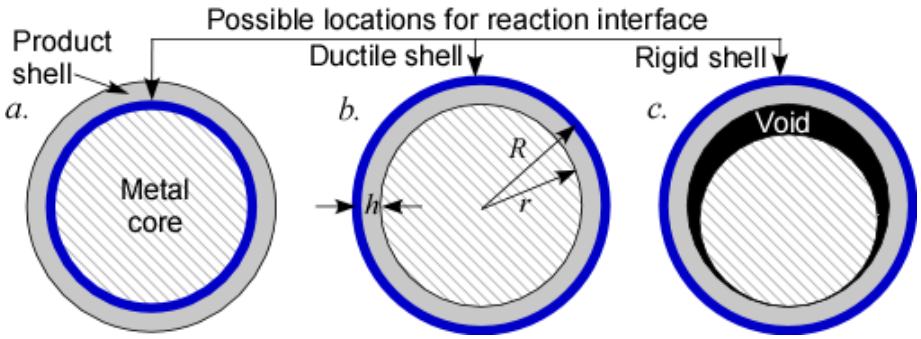

Figure 5.2 Schematic diagram illustrating possible locations for the reaction interface: a. Reaction at the inner metal/product shell interface; b. Reaction at the outer metal/product shell interface, ductile shell; c. Reaction at the outer metal/product shell interface, rigid shell.

Both coarse and fine powder size fractions were heated at a rate of 10 K/min up to 1100 K using steam as an oxidizer. The measured TG traces are shown in Figure 5.3. An inset shows the results expanding the temperature range between 800 and 900 K, where the most significant difference between the two traces was observed.

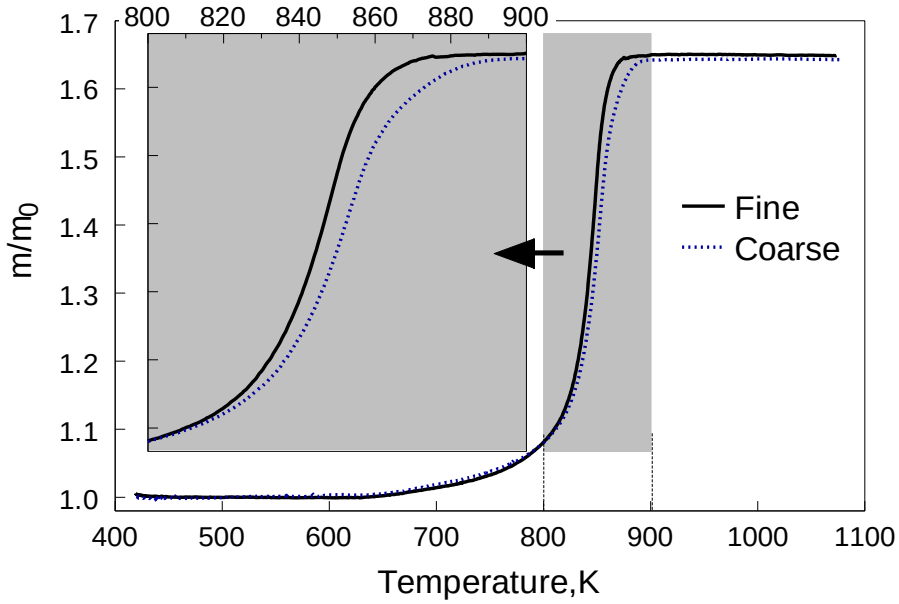

Figure 5.3 TG traces for two size fractions of the magnesium powder oxidizing in steam; heating rate was 10 K/min.

Mass changes shown in Figure 5.3 were distributed among different particle size bins for both powder fractions assuming reaction models illustrated in Figure 5.2 a, b, and c and using particle size distributions shown in Figure 5.1. The mass changes can be translated into oxide thickness, a convenient indicator of the reaction progress. In this processing, the initial oxide thickness was taken as 24 nm, following Reference [128], where it was determined based on the total weight gain of the Mg powder fully oxidized in steam. For example, for two size fractions, two curves for the obtained oxide thickness as a function of temperature for a selected, 20.7 μm particle size, are shown in Figure 5.4 for three reaction scenarios. This specific particle size is present in both powder fractions; thus, for an ideal model the two curves shown in Figure 5.4 should coincide. Note that the temperature range shown in Figure 5.4 is narrowed down to focus on the discrepancies between different curves.

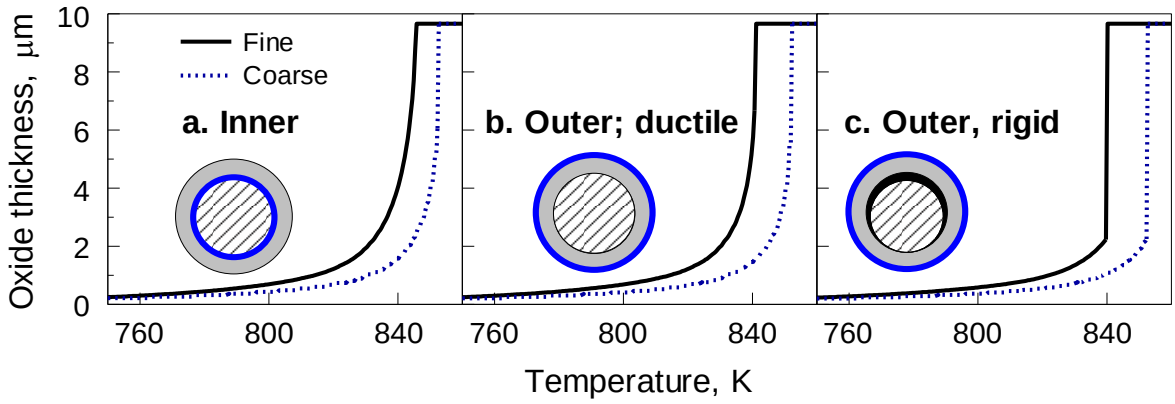

Figure 5.4 Comparison of oxide thicknesses predicted to grow for a magnesium particle with initial diameter of 20.7 μm from both fine and coarse powders using three different oxidation models shown in Figure 5.2. Experimental data shown in Figure 5.3 are processed using size distributions shown in Figure 5.1.

It appears that the discrepancies are somewhat smaller for case a, when the reaction is assumed to occur at the inner metal-product layer interface. These discrepancies were

assessed quantitatively for all sizes present in both powder fractions using parameter, Er_i, calculated for each particle size bin, i:

$$Er_i = \sqrt{\frac{\sum_j \left(m_{i,j}^{Coarse} - m_{i,j}^{Fine} \right)^2}{j}} \tag{5.1}$$

where summation is done for all j time steps for the measurement and $m_{i,j}^{Coarse}$ and $m_{i,j}^{Fine}$ are the weight changes for coarse and fine Mg fractions respectively, corresponding to the j^{th} time step.

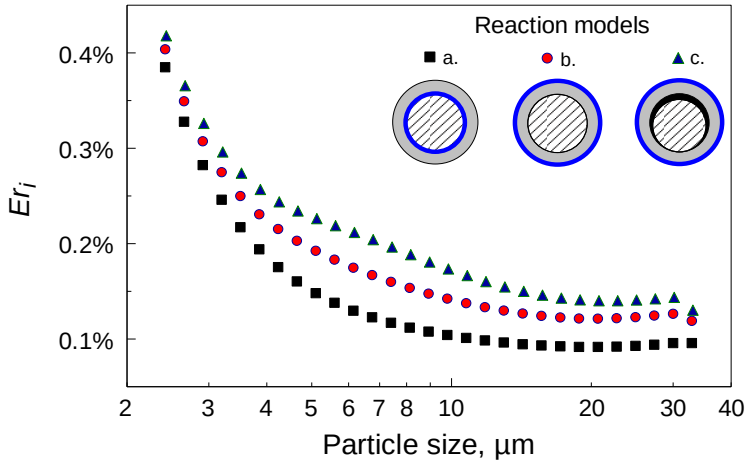

Figure 5.5 Total discrepancy measure calculated using Equation (5.3) for data on oxidation of Mg in steam processing using different reaction models.

Parameter Er_i reduces the differences between the calculated traces shown in Figures 5.4 to one number, quantifying discrepancy implied by each model for the entire measurement. Parameter Er_i is plotted in Figure 5.5 for all the overlapping particle sizes for two Mg powder fractions. The discrepancy between predictions is minimized for the case a

shown in Figure 5.2, when the reaction of Mg with steam is assumed to occur at the inner interface between magnesium and the growing product layer.

The same approach was followed to identify the reacting interfaces for the oxidation of Mg by oxygen at elevated temperature and by water vapor at low temperatures (latter experiments were performed isothermally.)

Both coarse and fine fractions of Mg powder were heated up to 840 K at a heating rate of 2 K/min in order to minimize the possibility of ignition in the furnace. The mass change for two size fractions of the magnesium powder oxidizing in oxygen was plotted as function of temperature and shown in Figure 5.6. A noticeable discrepancy of reaction rate between the two magnesium powders was observed from the result. The mass changes were distributed among different particle size bins for both powder fractions assuming reaction models illustrated in Figure 5.2 a, b, and c and using particle size distributions shown in Figure 5.1.

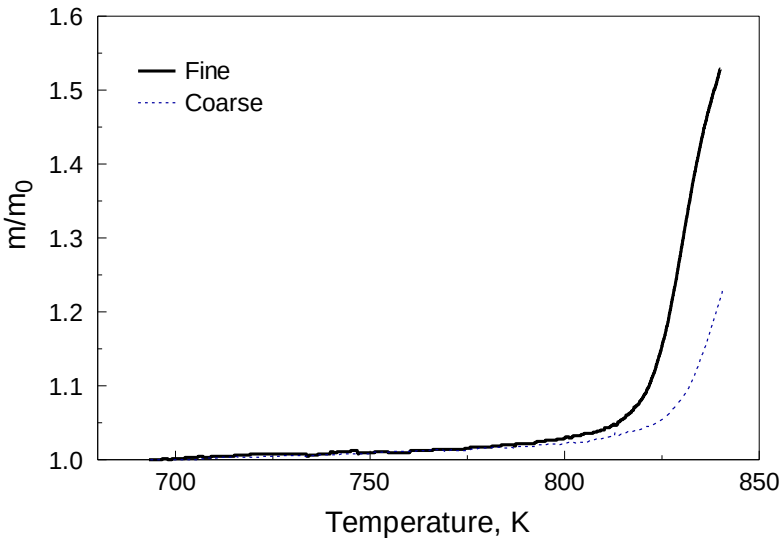

Figure 5.6 TG traces for two size fractions of the magnesium powder oxidizing in oxygen; heating rate was 2 K/min.

The quantitative analysis was performed using Equation (5.3) for the reaction of magnesium with oxygen at elevated temperature for all the overlapping size bins as well. In contrast to the oxidation in steam, however, the TG measurements could not be used over the whole temperature range due to slight but noticeable magnesium evaporation, and therefore unreliable final mass. The analysis was therefore limited to a maximum temperature of 800 °C. This has the effect that in the case of oxidation in dry oxygen the large mismatch associated with complete oxidation (see Figure 5.4) is not accounted for in the value of *Er*. The results of comparisons among three possible reaction models are shown in Figure 5.7. Similarly to reaction with steam, the reaction interface for magnesium with oxygen at elevated temperature is located between the metal and its oxide layer although the difference between the scenarios sharply decreases for larger particles due to the limited temperature range.

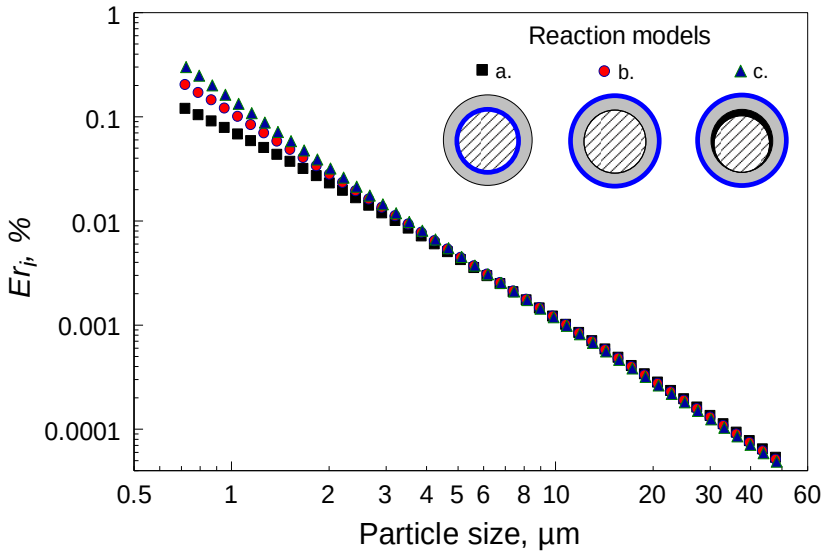

Figure 5.7 Total discrepancy measure calculated using Equation (5.3) for the reaction of magnesium with oxygen at elevated temperature using different reaction models.

Finally, the isothermal reaction of magnesium powders with water vapor at 60 °C was characterized using TAMIII. The normalized heat flow for both, coarse and fine magnesium powder fractions was converted to the mass change as a function of time. Both, the experimental heat flow traces and respective calculated mass changes for magnesium powder are shown in Figure 5.8 a and b, respectively; a significant difference between the two traces of mass changes was observed in Figure 5.8 b.

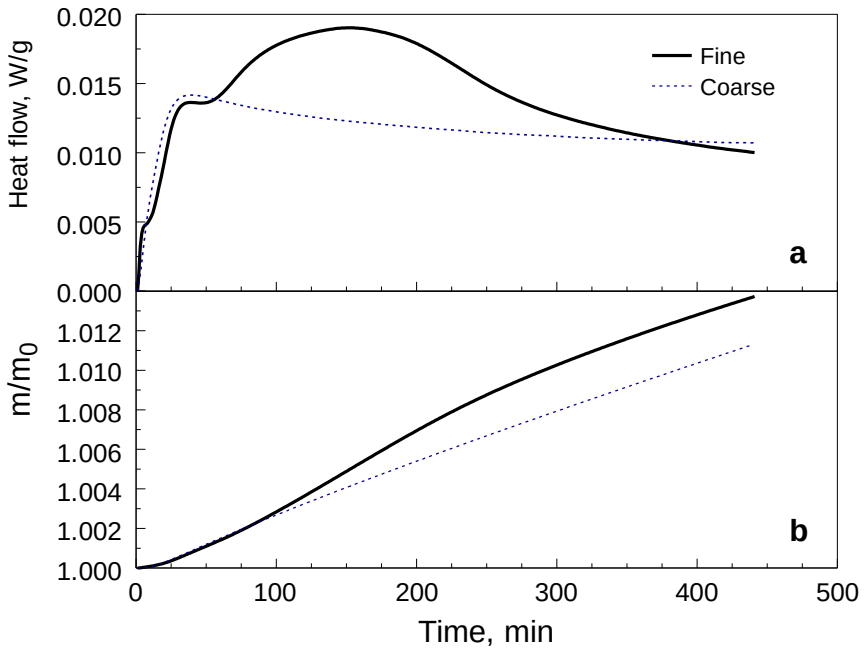

Figure 5.8 Experimental heat flow traces obtained in TAMIII isothermal measurements for fine and coarse fractions of the magnesium powder oxidizing in humid argon at 60 °C and inferred mass changes for the powder loads.

The quantitative analysis was also performed for the reaction of magnesium with water vapor at low temperatures for all overlapping particle size bins. The comparisons among three possible reaction models are shown in Figure 5.9. The absolute values of the differences are small due to the limited degree of oxidation in the low temperature

isothermal measurements. Like in the previous cases, the reaction interface for magnesium with water vapor at low temperatures is located between the metal and its hydroxide layer.

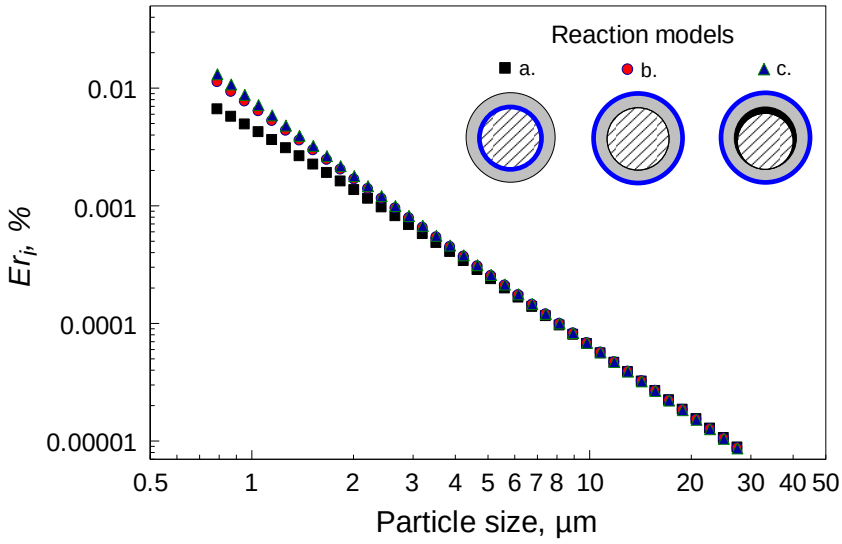

Figure 5.9 Total discrepancy measure calculated using Equation (5.3) for the reaction of magnesium with water vapor at low-temperatures using different reaction models.

Based on Figures 5.5, 5.7, and 5.9, the obtained results indicate that the reaction always occurs at the interface between magnesium and its oxide or hydroxide layer.

5.4.2 Low-Temperature Oxidation of Magnesium in Water Vapor

5.4.2.1 Experimental Results. Normalized heat flow curves recorded for the isothermal reactions of a magnesium powder (as received or coarse fraction) with water vapor mixed with argon and air at three temperatures: 40, 60 and 80 °C are shown in Figure 5.10 as grey solid lines. For both, argon and air carrier gases, the reaction rate increases with increasing temperatures as expected. In addition, the main oxidation peak was generally preceded by an induction period, consistent with previous reports on low-temperature oxidation of metals [121-123]. Since Mg hydroxide is more stable than the oxide in the presence of

water, it is likely that initially hydration contributes to the measured heat flow. The hydration leads to recrystallization of the oxide layer to yield the stable magnesium hydroxide [110, 124]. Assuming an initial dry oxide layer with a thickness of 24 nm [120], one calculates a total enthalpy of hydration of approximately 260 J/g for the coarse fraction, and 600 J/g for the fine fraction. The measurements show an integrated enthalpy of roughly 25 J/g and 150 J/g at the end of the induction period for the coarse and fine fractions, respectively. This is consistent with partial hydration of the oxide layer before the onset of the main oxidation reaction.

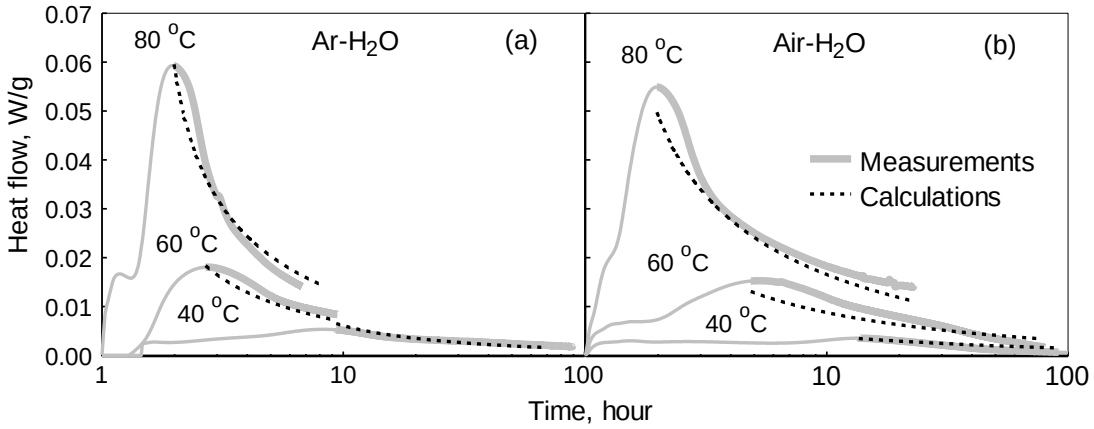

Figure 5.10 Normalized heat flows for magnesium powder oxidizing in water vapor at 100% relative humidity in argon and air (carrier gases) at three different temperatures: 40, 60 and 80 ºC.

The decaying parts of traces shown in Figure 5.10 will be described below using a conventional oxidation model. Accounting for the hydration of the initial oxide layer would consistently amount to a correction of up to 30 % to the integrated heat at the peak heat flow, which is used as the starting point for the model fits. Since the measured heat flow curves cannot be easily deconvolved to separate the oxide hydration from the metal oxidation, the oxide hydration heat effect was considered a minor contribution to the

results, and not corrected for. Even with this limitation, these data and respective reaction kinetics are expected to be useful in describing the rate at which Mg powders would age while exposed to humid environments.

Normalized heat flow traces for magnesium oxidized using humid argon at different humidity levels at 80 ºC are shown in Figure 5.11. At low humidities (50 – 70%), two peaks are observed. The second peak shifts quickly to shorter times as the humidity increases, consistent with more rapid oxide hydration. When the humidity exceeds 80%, the second peak becomes indistinguishable from the first one. At 90% humidity, another, third peak appears to follow what is expected to be merged first and second peaks. The amplitude of the initial peak drops when the humidity reaches 95%. The amplitude of the following (third) peak increases respectively.

What causes the appearance of multiple peaks at higher humidities remains speculative. A porous hydroxide layer could change morphologically, or the porosity could be saturated with condensed water, causing enhanced diffusion, and faster reaction. The aim of the present work is to describe the rate of these reactions. A future detailed structural analysis is warranted.

It should be possible to correlate the decaying portions of the traces shown in Figure 5.11 with a regular oxidation scenario, while the earlier parts of the peaks represent various induction processes.

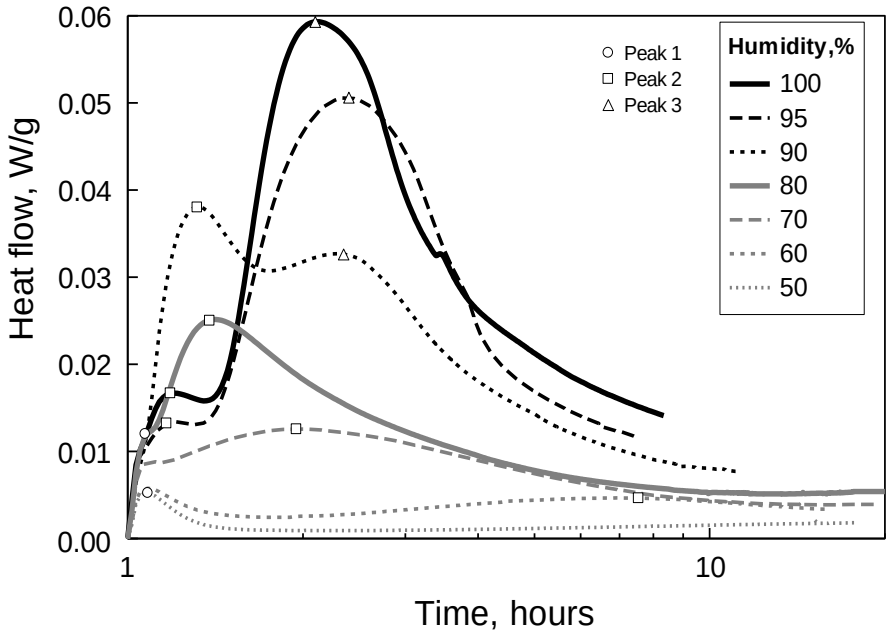

Figure 5.11 Normalized heat flows for magnesium oxidized in humid argon at different humidities at 80 ºC.

5.4.2.2 Reaction Kinetics. Following the previously developed model in Reference [31], the formula in Equation (5.2) was used to describe the rate of a direct diffusion limited oxidation for a spherical oxide layer. In current work, same equation was applied to describe magnesium oxidation as well. Decaying portions of the measured heat flow curves were described using an explicit oxidation model for spherical particles (cf. case *a*, Figure 5.2) given in terms of the rate of increase of mass of the formed hydroxide (or oxidized magnesium), $\frac{dm_{ox}}{dt}$, as:

$$\frac{dm_{ox}}{dt} = C \cdot e^{\left(-\frac{E}{R_{gas} \cdot T}\right)} \cdot \left(\frac{1}{r_i} - \frac{1}{R_i}\right)^{-1} \tag{5.2}$$

The measured heat flow was translated into $\frac{dm_{ox}}{dt}$ accounting for the magnesium oxidation enthalpy; values of r_i and R_i were calculated based on the experimental heat flow as a function of time considering the surface area based average particle size. Values of the activation energy, E and pre-exponent, C were treated as adjustable parameters. Different reaction models, expressed mathematically as the last term in Equation (5.2), were considered. The reaction model reflected in Equation (5.2) represents oxidation limited by diffusion through a growing spherical product shell and gave the best match with experimental data. Initially, three traces measured at 100% humidity and at constant temperatures of 40, 60, and 80 °C, respectively, were fitted simultaneously. The fitting began from the peak in the heat flow, matching the decaying portion of each trace. For each peak position, thickness of magnesium hydroxide and the respective value of m_{ox} were calculated using the experimental integrated heat release. The resulting values of activation energy and pre-exponent for both air- and argon-based humid environments are given in Table 5.1. Calculated traces are shown as black dashed lines in Figure 5.10. The match between experimental and computed traces is adequate.

Table 5.1 Kinetic Parameters for Low-Temperature Oxidation of Magnesium in Humid Environments

Kinetic parameters	Oxidizing environments	
	Ar-H_2O	Air-H_2O
Ea, kJ/mol	58.2	62.6
C, g/m/s	3.38E-03	1.35E-02

Changed humidity was expected to affect the pre-exponent only, leaving the activation energy unchanged. Therefore, the experimental results shown in Figure 5.11 were interpreted using the same activation energy as given in Table 5.1, while adjusting the

pre-exponent. Note that decays after both second (merged with the first) and the third peaks observed at higher humidities were considered. Decay after the second peak could not be processed for 50% humidity, because the experiment was not long enough to capture the respective decay. The values of pre-exponents are shown in Figure 5.12 and Table 5.2. The pre-exponent identified as describing decay of the second peak should be used for humidities lower than 90%; the pre-exponent describing decay of the third peak is appropriate for higher humidities. An increase in the value of the pre-exponent that is directly proportional to the humidity is reasonable, representing an expected acceleration in the reaction kinetics.

Comparisons between measured and calculated heat flow traces at different humidities are shown in Figure 5.13. Calculated curves represent the general observed trends, although they do not reproduce the experimental data perfectly.

Obtained reaction kinetics can now be used to predict aging of magnesium powders exposed to humid environments. Such aging is well-known to occur; however, there has been no quantitative data enabling one to predict the rate at which the powder is being oxidized. Considering, for simplicity, a monodisperse 30-μm diameter powder at room temperature, predictions were made for both argon and air based environments at 100 % humidity.

Table 5.2 Pre-exponent for the isothermal reaction of Mg with varied relative humidity in argon at 80 °C

	Humidity	100%	95%	90 %	80 %	70 %	60 %
C $\times 10^3$, g/m/s	Second peak			2.20	1.07	0.82	0.47
	Third peak	6.13	5.08	3.04			

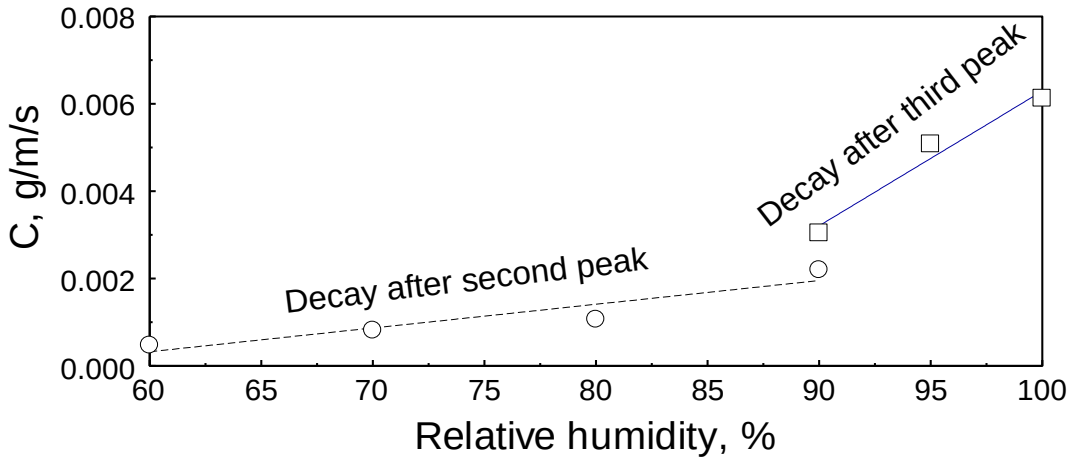

Figure 5.12 Pre-exponents of the low-temperature reaction of Mg with water vapor as a function of relative humidity.

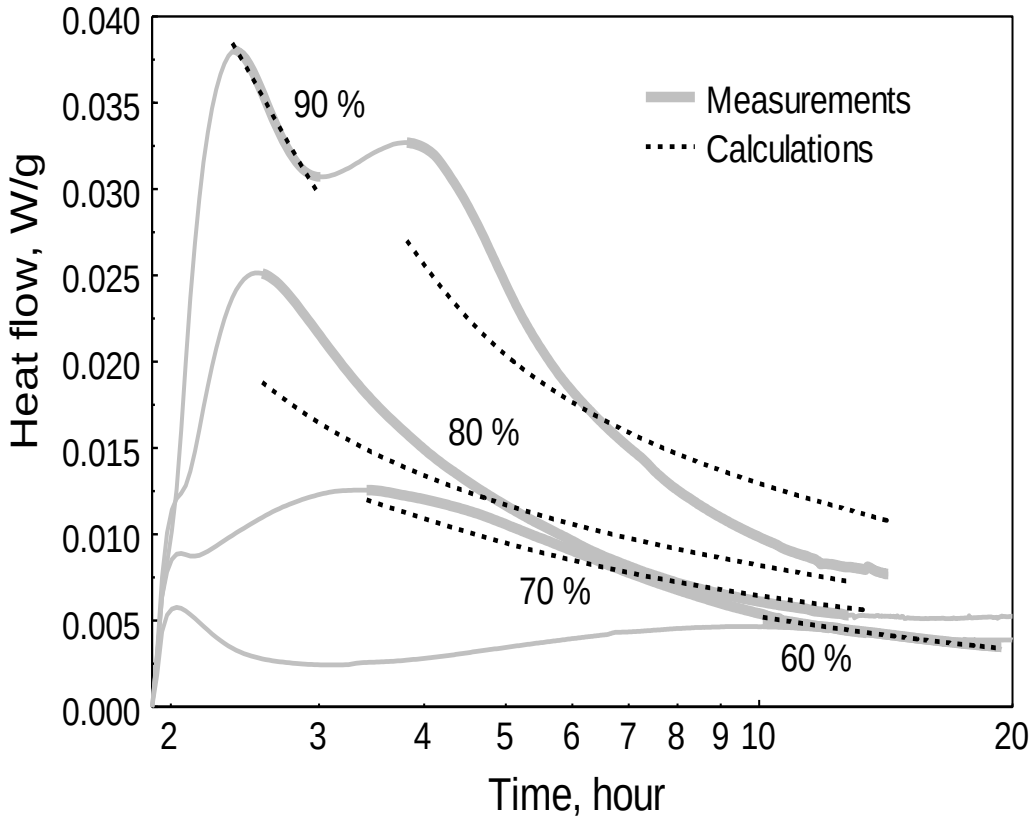

Figure 5.13 Calculated vs. experimental normalized heat flows of Mg oxidized in humid argon at varied relative humidities and at a constant temperature, 80 °C. Bold portions of the experimental curves were used to obtain reaction kinetics.

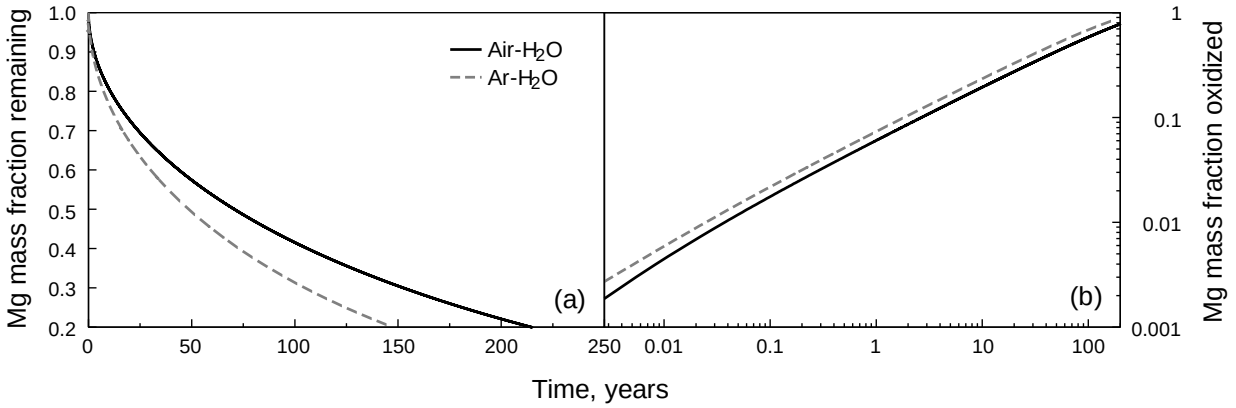

Figure 5.14 Magnesium oxidation (aging) predicted to occur at room temperature (25 °C) in air and argon-based environments at 100 % humidity.

At lower humidities, oxidation will slow down. Respective estimates are illustrated in Figure 5.15. For 60% humidity, only between 6 and 7% of magnesium are predicted to be oxidized after 0.1 year.

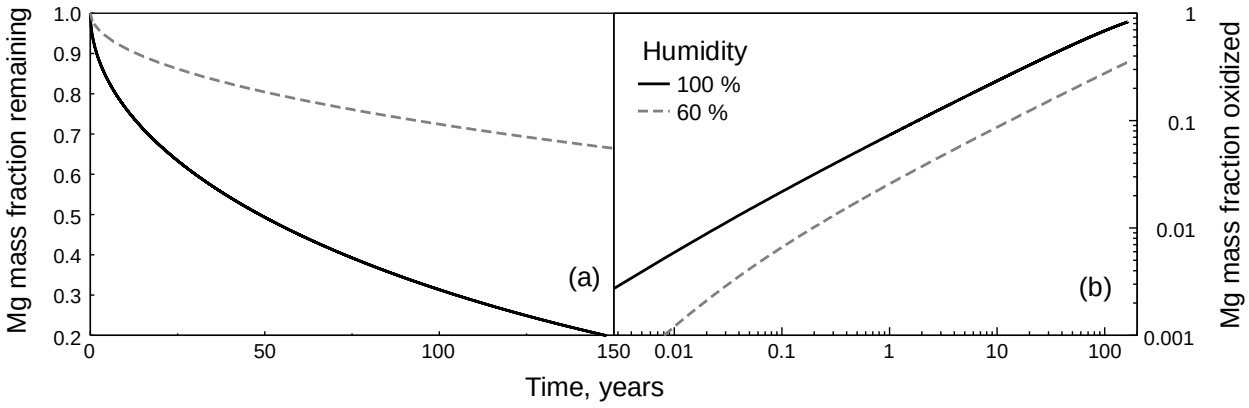

Figure 5.15 Magnesium oxidation (aging) predicted to occur at room temperature (25 °C) in the argon-based environment at different humidities.

Results are shown in Figure 5.14. On the left hand side, Figure 5.14a, remaining un-oxidized fraction of magnesium is shown versus time. On the right hand side, Figure

5.14b, the same calculation is presented in terms of magnesium mass oxidized, plotted vs. time on a logarithmic scale. It is predicted that the aging occurs somewhat faster in argon-based environments, although the difference between the two environments is minor. After only a relatively short storage time (about 0.1 year, Figure 5.14b), close to 20% of magnesium is expected to be oxidized. However, even after 200 years, it is expected that at least 20% of magnesium will remain unoxidized.

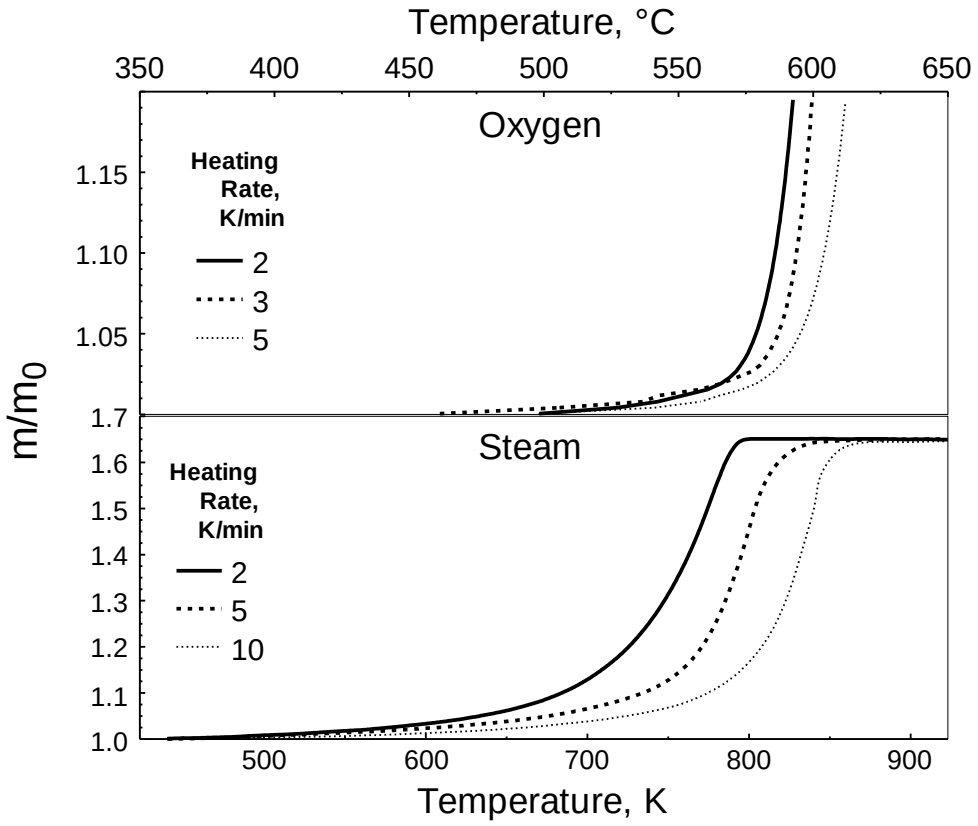

Figure 5.16 TG traces for magnesium oxidation with oxygen and steam obtained at different heating rates.

5.4.3 High Temperature Oxidation of Magnesium in Water Vapor and Oxygen

5.4.3.1 Experimental Results. Results of TG measurements performed at different heating rates for magnesium reacting with steam and oxygen are shown in Figure 5.16. The weight gain shifts to higher temperatures at greater heating rates, as expected for thermally activated reactions. The temperatures were limited for the measurements in oxygen to minimize evaporation of magnesium, making the results difficult to interpret and contaminating the furnace. The mass gain is small and the signal is noisy at lower temperatures, especially for reactions in oxygen.

5.4.3.2 Reaction Kinetics. Reaction rates are commonly described as a kinetic triplet, including activation energy, pre-exponent, and a function of reaction progress, *f(α)*:

$$\frac{d\alpha}{dt} = C \cdot \exp\left(-\frac{E}{R_{gas}T}\right) \cdot f(\alpha) \tag{5.3}$$

A model free isoconversion method [96, 97] was used to determine the activation energy as a function of the reaction progress [129-131]. At each given α, the function Φ is minimized:

$$\Phi(E_\alpha) = \sum_{i=1}^{n} \sum_{j \neq i}^{n} \frac{J\left[E_\alpha, T_i(t_\alpha)\right]}{J\left[E_\alpha, T_j(t_\alpha)\right]} \tag{5.4}$$

where the subscript α refers to selected values of the reaction progress that were observed at time t_α and the corresponding temperature *T*, and which are associated with the

activation energy E_α. The sums are taken over all included experiments. The functions J are integrals of the exponent of activation energy over experimental temperature over a chosen interval $\Delta\alpha$:

$$J\left[E_\alpha, T_i\left(t_\alpha\right)\right] = \int_{t_{\alpha-\Delta\alpha}}^{t_\alpha} \exp\left[\frac{-E_\alpha}{RT_i\left(t_\alpha\right)}\right] dt \tag{5.5}$$

Once the activation energy is obtained, the pre-exponent can be estimated assuming a specific form for the progress function $f(\alpha)$. The calculation of the pre-exponent used the reaction model given by Equation (5.2). In other words, as before, reaction was assumed to occur for a core-shell geometry, as shown in Figure 5.2a, and to be rate limited by diffusion through a coherent oxide layer.

Results of the model-free isoconversion processing for measurements in oxygen are presented in Figure 5.17 in terms of activation energy as a function of a uniform estimated oxide thickness. After a quick initial increase, the activation energy is observed to stabilize around 148 kJ/mol.

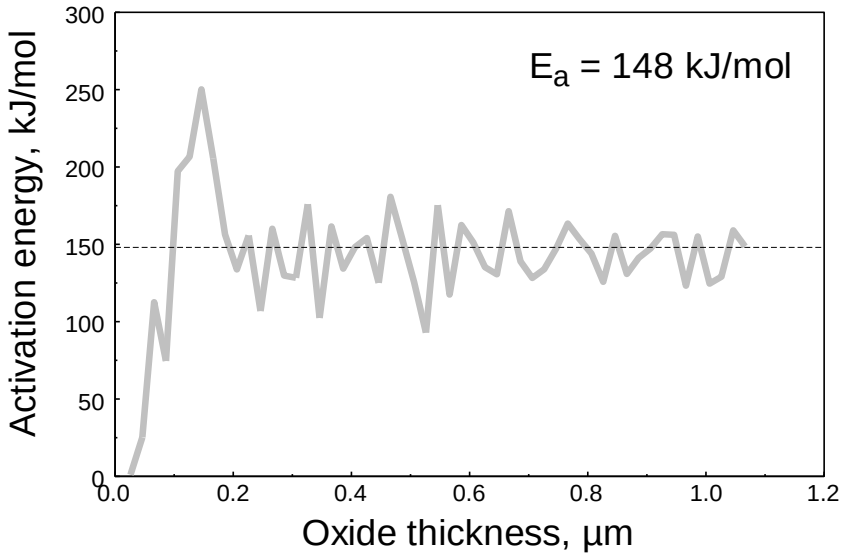

Figure 5.17 Activation energy of the reaction of Mg with oxygen as a function of oxide thickness of magnesium.

Once the activation energy for the reaction of Mg with oxygen was determined, the pre-exponent, *C*, was evaluated as a function of temperature or oxide thickness using experimental data shown in Figure 5.16 and Equation (5.2). The resulting pre-exponent as a function of the oxide thickness is shown in Figure 5.18. The solid curve represents the result of calculations using experimental data, the dashed curve is a 4^{th} order polynomial line fit. This polynomial fit was used in validating calculations, aimed to reproduce the experimental data using the identified reaction kinetics, summarized in Table 5.3.

Table 5.3 Reaction Kinetics Parameters Describing Oxidation of Magnesium in Oxygen Following Equation (5.2)

Range of oxide thicknesses	Activation energy, *E*, kJ/mol	Pre-exponent, *C*, g/m/s (oxide thickness *h* is in μm)
24 nm to 1 μm	148	$434 \cdot h^4 - 834 \cdot h^3 + 863 \cdot h^2 - 107 \cdot h + 6.76$

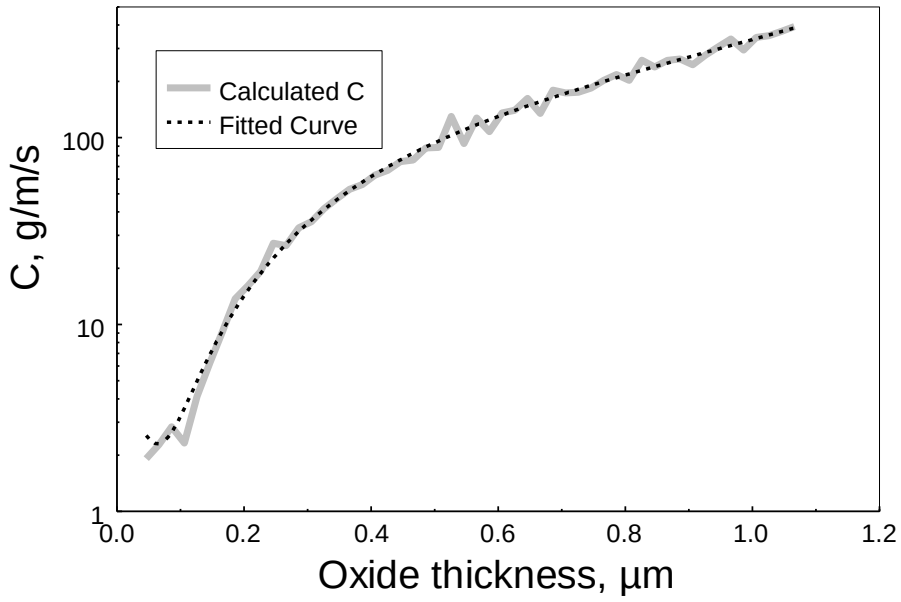

Figure 5.18 Pre-exponent of the reaction of Mg with oxygen as a function of oxide thickness of magnesium.

Results of the validating calculations are shown in Figure 5.19. Considering substantial noise in measurements observed at low temperatures, the match between the calculations and experimental data is acceptable. Both shift in the predicted TG traces as a function of the heating rate and the slope showing the rapid increase of weight during oxidation are well reproduced.

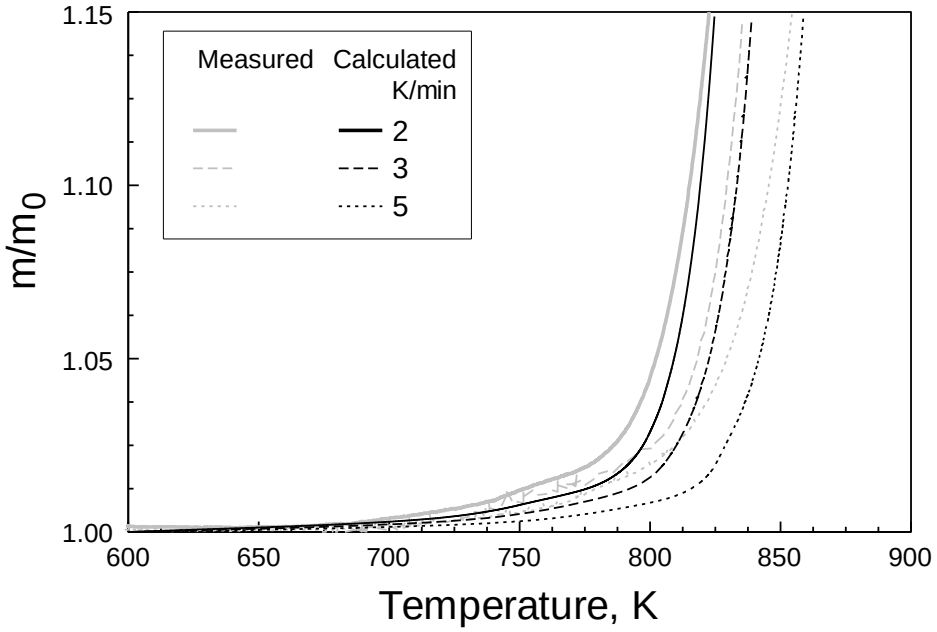

Figure 5.19 Measured vs. calculated TG traces for magnesium oxidation in oxygen at different heating rates.

Results of the model-free isoconversion processing for measurements on magnesium oxidation in steam carried by argon are shown in Figure 5.20. Unlike for oxygen, activation energy is observed to steadily increase as a function of the oxide thickness. This increase stops at about 360 kJ/mol when the oxide thickness exceeds 2.4 μm. For practical and validating calculations, the activation energy is assumed to increase linearly up to 360 kJ/mol, as shown by a dashed line in Figure 5.20 and in Table 5.4. The results for the pre-exponent, which correlate with the obtained activation energy, are also shown in Table 5.4.

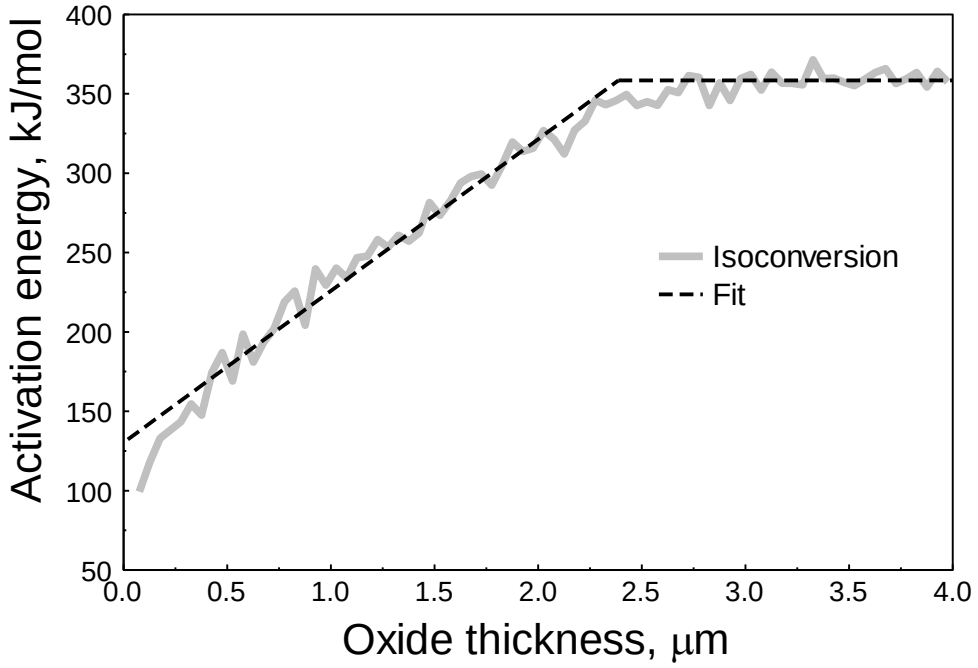

Figure 5.20 Activation energy for oxidation of magnesium in steam at elevated temperatures as a function of the magnesium oxide thickness.

Table 5.4 Reaction Kinetics Parameters Describing Oxidation of Magnesium in Steam at Elevated Temperatures Following Equation (5.2)

Range of oxide thickness	Activation energy, kJ/mol, *h* is in μm	*Ln(C)* (g/m/s); *h* is in μm
24 nm to 2.4 μm	$94.99 \cdot h + 130.4$	$6.59 \cdot h + 0.368$
>2.4 μm	358.4	16.2

Validating calculations comparing predictions made using the identified kinetics with the measurements for magnesium oxidation in steam are shown in Figure 5.21. Both shifts to higher temperature at greater heating rates and slopes of individual TG traces are well reproduced in calculations. Therefore, the reaction kinetics identified in Table 5.4 is useful in predicting the rates at early stages of magnesium oxidation in steam at elevated temperatures using Equation (5.2).

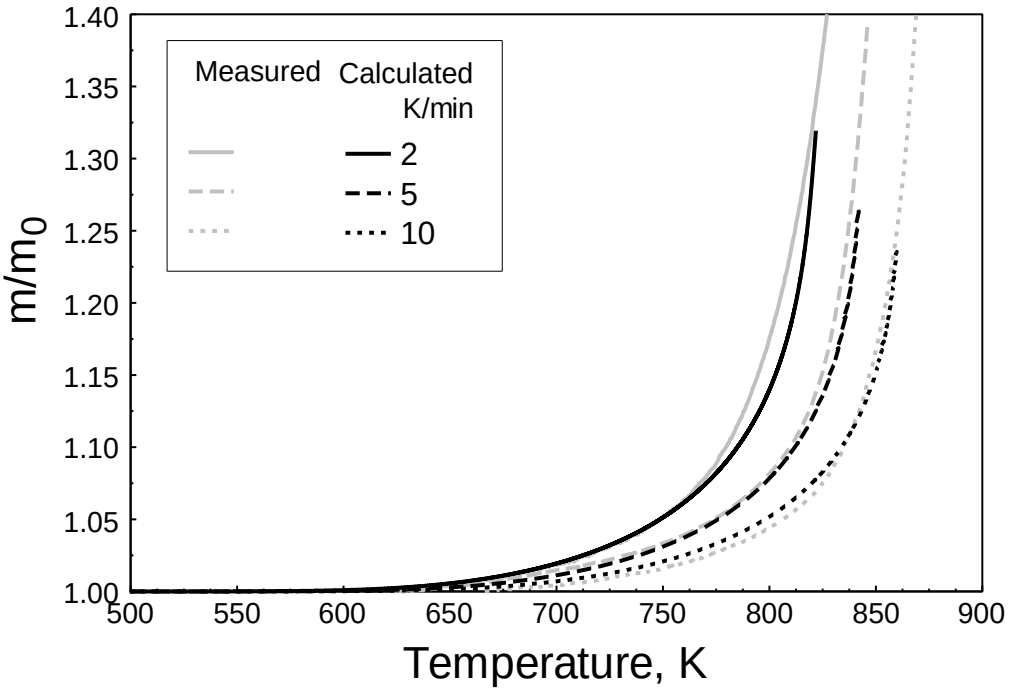

Figure 5.21 Comparison of measured TG traces and calculated TG traces of the reaction of Mg in steam for three heating rates.

Apparent kinetic parameters of Mg oxidation in dry oxygen and in steam can be compared to a limited extent. It should be noted that the final degree of oxidation is different in both sets of high temperature measurements. The measurements in dry oxygen are limited to estimated oxide thickness of less than 1.2 µm, while thicknesses up to 4 µm were reached in steam. The limitation is primarily due to evaporation of Mg and resulting unreliable measurements at higher temperatures.

In the thickness range that is covered by both sets of measurements, the activation energies are comparable. In steam, it starts from about 100 kJ/mol and increases to about 240 kJ/mol, while in dry oxygen it levels off to near constant 148 kJ/mol. The increase in activation energy, which is not based on the assumption of a specific mechanistic model, could indicate a change in the diffusing species in the presence of water.

Conversely, the pre-exponent derived using the core-shell geometry, and assuming the shell is uniform and not explicitly porous, shows different behavior. In oxygen, the pre-exponent changes by about 2 orders of magnitude up to an estimated thickness of 1.2 μm, while in steam the pre-exponent changes by about one order of magnitude and then levels out at 2.4 μm estimated thickness.

The pre-exponent *C* was treated as a comprehensive oxidation rate constant in Equation (5.2), accounting for diffusion limited reaction and evolution of the reacting interface. As the diffusion resistance of the oxide layer and the morphology of the reacting interface change during the reaction, *C* was affected and changed as a function of reaction progress (temperature or oxide thickness). Any and all changes in the true oxidation mechanism are now lumped into the pre-exponent. Contrary to the assumption of a uniform oxide shell, the oxide is porous, however, and this porosity could be counteracted by faster diffusion in the presence of water, leading to continuous recrystallization and sintering of the oxide. An additional obstacle to describing these changes mechanistically comes from the observed tendency of Mg to evaporate at higher temperatures.

Care should be taken when applying the models presented here to situations where higher temperatures as well as greater mass changes/oxide thickness are encountered.

5.5 Conclusion

Reactions of heterogeneous magnesium oxidation occurring in a broad range of temperatures in both dry and wet environments producing either MgO or Mg(OH)2 take place at the interface between magnesium metal and the growing oxidized product layer. This suggests that the reactions are rate limited by diffusion of oxidizer through the growing magnesium oxide or magnesium hydroxide layers.

All oxidation reactions for magnesium powders can be described reasonably well using a model assuming that the reaction is limited by thermally activated diffusion of oxidizer through a growing shell of the product. Activation energy of magnesium oxidation in humid environments at low temperatures is close to 60 kJ/mol. The pre-exponent varies in a range of 10-3-10-2g/m/s, depending on a specific environment and humidity. The identified low-temperature reaction kinetics enables one to describe aging of Mg powders stored at different temperatures and humidities.

Reaction kinetics at elevated temperatures, which is relevant for modeling ignition of magnesium and its alloys, is also quantified. Activation energy for oxidation of magnesium in oxygen is 148 kJ/mol. To adequately describe the observed reaction, the pre-exponent should increase as a function of the growing oxide layer, reaching ca. 350 g/m/s for 1-μm thick oxide. For oxidation of magnesium in steam at elevated temperatures, the activation energy increases linearly from approximately 130 to 360 kJ/mol, while the forming oxide layer thickens up to 2.4 μm. The preexponent, C, increases simultaneously with the activation energy; $ln(C)$ in g/m/s reaches 16.2 when the oxide thickness reaches 2.4 μm.

CHAPTER 6

OXIDATION OF ALUMINUM-MAGNESIUM ALLOY POWDERS IN OXYGEN

6.1 Abstract

Alloys of aluminum and magnesium are widely used in pyrotechnics as well as in other energetic formulations. They were also explored recently as metal additives in oxygen generators and as materials capable of reacting with water for hydrogen production. Thus, mechanisms of low-temperature, heterogeneous oxidation of such alloys by both oxygen and water are of interest. Understanding such mechanisms enables one to model both their aging and initiation in various devices. In this work, both commercial atomized spherical Al-Mg alloys and mechanically alloyed Al-Mg powders were oxidized in oxygen using thermo-gravimetry (TG). Fully and partially reacted powders were recovered and characterized using scanning electron microscopy and x-ray diffraction. Voids grow within oxidized alloy powders for both atomized and mechanically alloyed powders. Two oxidation stages were identified for both spherical Al-Mg alloys and mechanically alloyed powders. Magnesium was first oxidized selectively, producing MgO. Spinel MgAl2O4 was produced during the second stage. The reaction interfaces were always located at the internal surface of the oxide shell as determined by matching the oxidation dynamics for particles with the same sizes but belonging to powders with different particle size distributions. Thus, the reaction is always rate limited by inward diffusion of oxygen ions through the growing oxide shell. Apparent activation energies for both oxidation stages were obtained as a function of the thickness of the growing oxide layer. The switchover between oxidation stages occurs when the oxide thickness exceeds 1.2 – 1.5 μm.

6.2 Introduction

Various Al-Mg alloys find multiple applications in structural materials [132, 133], for hydrogen storage [134], and as components of energetic formulations [135-137]. Most of the published work on oxidation of such alloys deal with compositions with small concentrations of Mg, varied from less than 1 to 5% [138-140]. For such materials, it was observed that the oxide includes different layers, with MgO typically observed on top of MgAl2O4 and/or Al2O3. At the same time, alloys with much higher concentrations of Mg are of interest for propellants, explosives, and pyrotechnics [141-144]. Oxidation of such high-Mg content materials is not well understood. In Reference [145], oxidation of an Al3Mg2 alloy was considered. The reaction was observed to proceed in three stages with three distinct rates: an MgO layer was formed initially; then MgAl2O4 oxide was produced, which finally cracked, leading to the third oxidation stage. However, detailed kinetic details enabling one to describe these reactions quantitatively are not available. Such descriptions are very important for reactive materials for prediction of both aging and ignition behaviors of the relevant compositions. Recently, thermo-analytical studies were used to clarify reaction mechanisms and describe them quantitatively for both Al [92, 127] and Mg [146] powders. Here, a similar experimental approach and data processing techniques are applied to characterize high temperature oxidation in Al-Mg alloys with equal mass fractions of aluminum and magnesium. The objectives are to identify the interface for heterogeneous oxidation reactions and describe reaction rates quantitatively. The experiments performed with two types of Al-Mg alloys prepared by different techniques, and thus having distinct initial structures and morphologies.

6.3 Experimental

6.3.1 Material

Two Al-Mg alloy powders with Al/Mg mass ratio of 50:50 were used in Thermo-gravimetric (TG) experiments. An atomized spherical alloy, -270 Mesh was provided by Valimet Inc. A mechanically alloyed powder was prepared at NJIT as described in detail elsewhere [36, 125, 147]. Briefly: starting materials for the mechanically alloyed powder were elemental powders of Al (Atlantic Equipment Engineers, 99.8% pure, -325 Mesh) and Mg (Alfa-Aesar, 99.8% pure, -325 Mesh). Mechanical alloying was performed using a Retsch PM-400 MA planetary mill operated at 350 rpm. Powder mass load was 30 g per vial; 9.5 mm-diameter hardened steel balls served as milling media. The ball to powder mass ratio was 10; the milling time was 2 hours. Each vial was filled with 50 mg of hexane used as a process control agent.

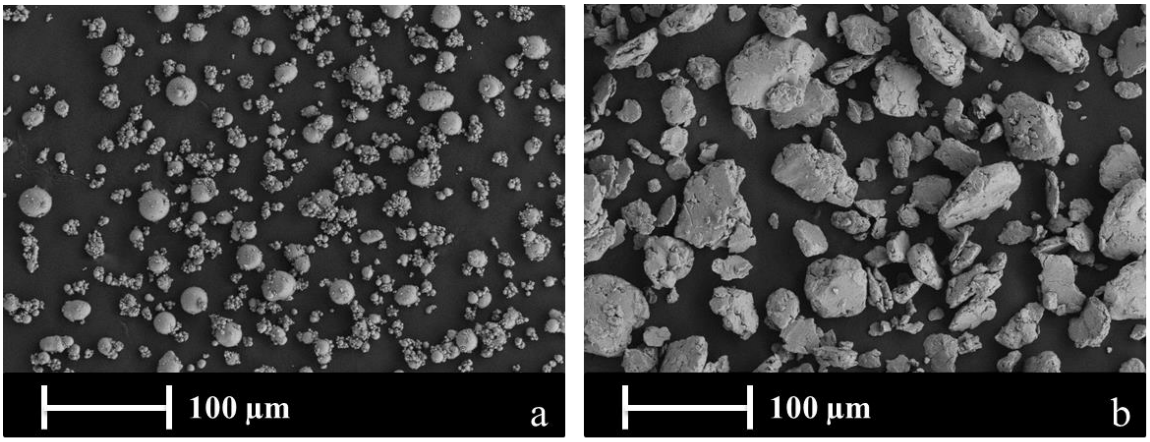

Figure 6.1 Backscattered SEM images for Al-Mg powders: atomized spherical alloy (a) and mechanically alloyed powder (b).

Scanning electron microscope (SEM) images for both Al-Mg alloy powders are shown in Figure 6.1. The particles have roughly spherical shapes for atomized Al-Mg alloys. Mechanically alloyed powder particles have characteristic angular shapes; they also are noticeably coarser than the atomized powders.

For detailed TG measurements described below, the spherical atomized alloy powder was split into two fractions with different but partially overlapping particle size distributions. The powder was passed through a 550 Mesh (25 μm opening) sieve. The particle size distributions for both obtained size fractions were measured using a Beckman-Coulter LS230 Enhanced Particle Analyzer as shown in Figure 6.2. These measured particle size distributions were directly used to process the TG measurements for the atomized alloy powder. The TG measurements for the mechanically alloyed powder were interpreted qualitatively and did not require particle size distribution measurements.

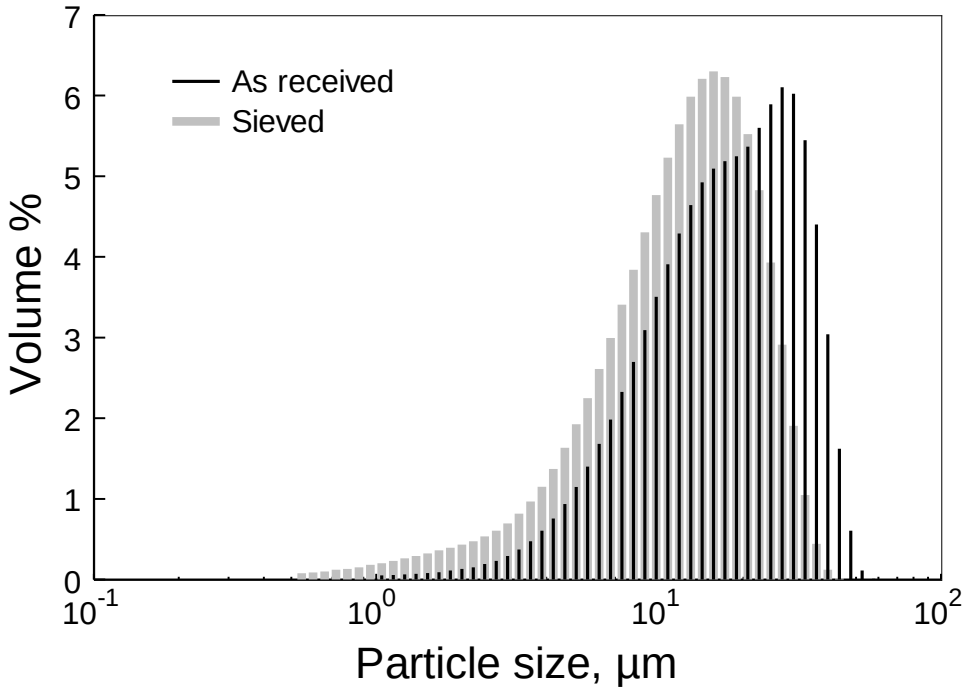

Figure 6.2 Particle size distributions for coarse (as received) and fine (sieved) fractions of the spherical atomized Al-Mg alloy powder used in experiments.

6.3.2 Oxidation Experiments

Both Al-Mg powders were oxidized in an oxygen/argon mixture using a Netzsch STA409PC/PG thermal analyzer with a thermogravimetric sample carrier. The customized furnace used in experiments provided the oxidizer flow from the top of the furnace down to the sample. This flow pattern helped to oxidize and condense evaporating magnesium directly in the sample holder. Magnesium evaporation and deposition of the oxide elsewhere in the furnace presented a serious experimental problem in preliminary experiments, when a regular furnace was used, in which the oxidizing gas was rising from the bottom up.

In these experiments, argon was introduced as both a protective gas surrounding the thermobalance and as a carrier gas for oxygen/argon oxidizing mixture; the respective flow rates of argon were 90 and 20 mL/min. The oxygen flow rate was 10 mL/min so that oxygen comprised 30% of gas supplied to the sample. The powders were held on a 17-mm diameter flat corundum sample holder and heated up to 800 °C. Heating rates varied from 2 to 20 °C /min in different experiments.

Fully and partially oxidized powders were recovered and examined using a scanning electron microscope (LEO 1530 Field Emission SEM); their compositions were characterized using x-ray diffraction (XRD) using a PANalytical Empyrean diffractometer. The diffractometer was operated at 45 kV and 40 mA using unfiltered Cu Kα radiation (λ = 1.5438 Å).

6.4 Results and Discussion

6.4.1 Phases and Morphologies Formed upon Oxidation

Initial oxidation TG measurements were performed for both atomized and mechanically alloyed powders at a fixed heating rate of 5 °C /min. The resulting TG traces and shown in Figure 6.3. For the atomized powder, an appreciable oxidation begins above 350 ºC. For mechanically alloyed powder, the weight increase becomes detectable above 400 ºC. For both materials, reaction accelerates substantially around 500 ºC. Above ca. 530 ºC, the rate of oxidation becomes slower. It remains nearly constant for the mechanically alloyed powder at higher temperatures. An additional acceleration in the oxidation rate is observed for the atomized powder at approximately 600 ºC.

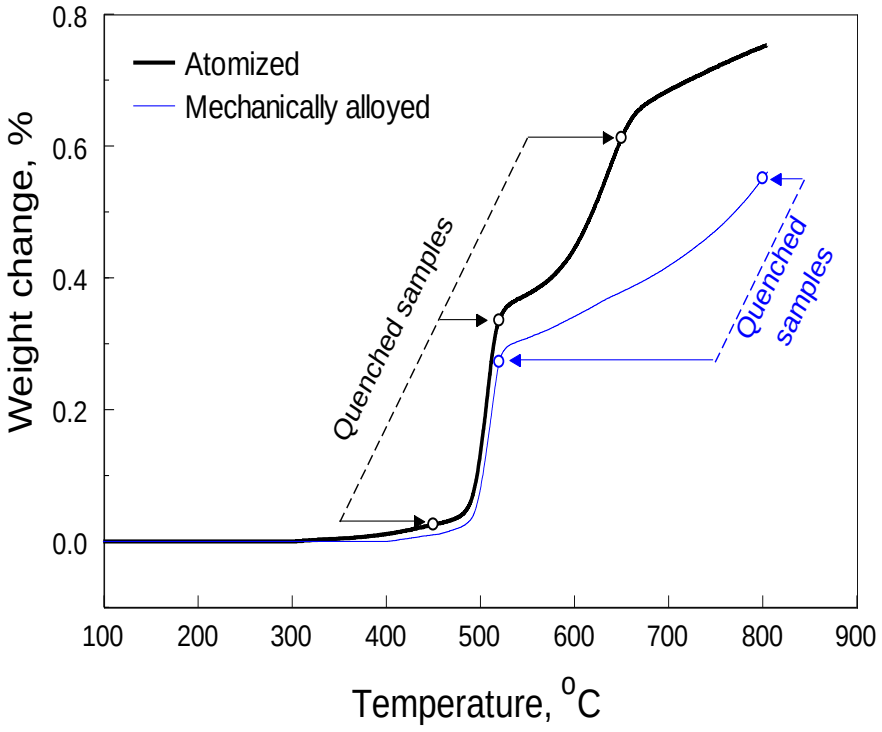

Figure 6.3 TG traces for the atomized spherical Al-Mg alloys (black) and mechanically alloyed Al-Mg powder (blue) in oxygen at 5 °C /min.

Open circles in Figure 6.3 show the temperatures, from which each powder was quenched and recovered for SEM and XRD analyses. The temperatures, from which the powders were recovered were 450, 520, and 650 °C for the atomized powder and 520 and 800 °C for the mechanically alloyed powder. These temperatures were selected to observe possible differences in the oxidation products formed at different reaction stages.

SEM images of the partially oxidized powders are shown in Figures 6.4 and 6.5 for atomized and mechanically alloyed powders, respectively. The atomized powder recovered at 450 ^{o}C, retains its spherical shape; however, the particle surface is not as smooth as for the original material. Minor surface depressions are noticed, which may indicate shrinkage of the thermally expanded particles. For the powder recovered from higher temperatures, as shown in Figure 6.4 (b) and (c), many broken hollow particles are observed. While breakage of the particles was most likely caused by the handling of the powder samples transferred to the SEM sample holder, as shown earlier 16, the hollow shells were clearly formed during oxidation. No qualitative difference was observed between samples shown in Figures 6.4 (b) and (c).

For the partially oxidized mechanically alloyed powders, the changes in the surface morphology upon oxidation were more noticeable as shown in Figure 6.5 (compare to the as prepared powder, Figure 6.1 (b)). In addition to multiple fine crystallites formed on surface of particles shown in Figure 6.5, formation of hollow structures is also observed, qualitatively similar to those seen in Figures 6.4 (b) and (c).

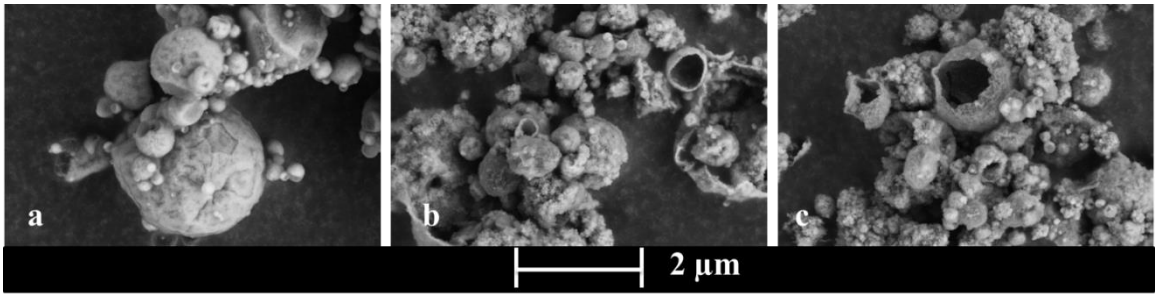

Figure 6.4 SEM images of partially oxidized atomized powder particles recovered from 450 °C (a), 520 °C (b) and 650 °C (c).

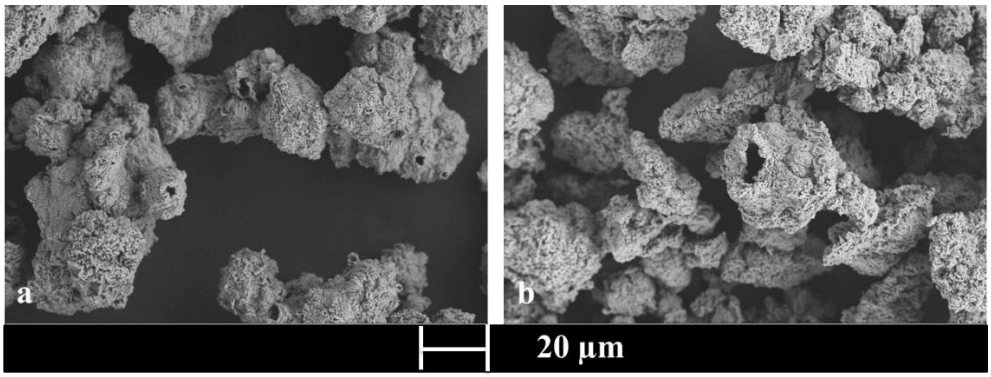

Figure 6.5 SEM images of partially oxidized mechanically alloyed powder particles recovered 520 °C (a) and 800 °C (b).

Results of the XRD analyses for partially oxidized samples of the atomized alloy are shown in Figure 6.6. At 450 °C, the sample mostly comprises of an $Al_{12}Mg_{17}$ intermetallic phase. Only small amounts of MgO are detectable. At 520 °C, strong peaks of both MgO and elemental Al appear. This clearly suggests a selective oxidation of Mg at low temperatures. At 650 °C, peaks of MgO remain nearly unchanged. Peaks of elemental Al become much weaker and strong peaks of the spinel group, $MgAl_2O_4$ appear.

XRD patterns for partially oxidized samples of the mechanically alloyed powder are shown in Figure 6.7. Note that the as prepared material was characterized by XRD earlier [36]. Unlike atomized powder, comprising the intermetallic Al12Mg17, the pattern

for the mechanically alloyed powder was dominated by the broadened peaks of elemental Al and Mg, with relatively minor peaks of the intermetallic. For the sample recovered at 520 °C, peaks of elemental Al and MgO become strong, similar to that observed in Figure 6.6 for the atomized powder. Also similar to the atomized powder, peaks of spinel, $MgAl_2O_4$ become well-visible for the sample recovered from 800 °C.

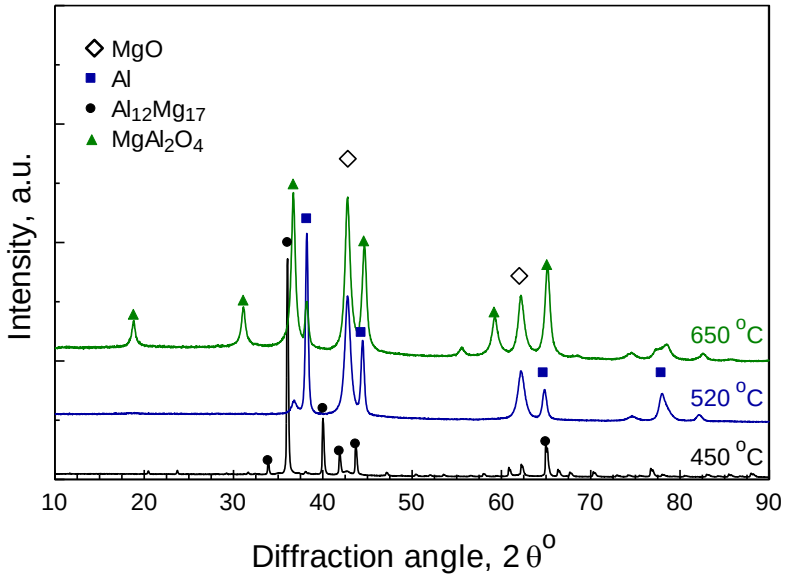

Figure 6.6 XRD pattern for the reaction products of spherical Al-Mg alloys powder quenched and recovered at 450 °C, 520 °C and 650 °C.

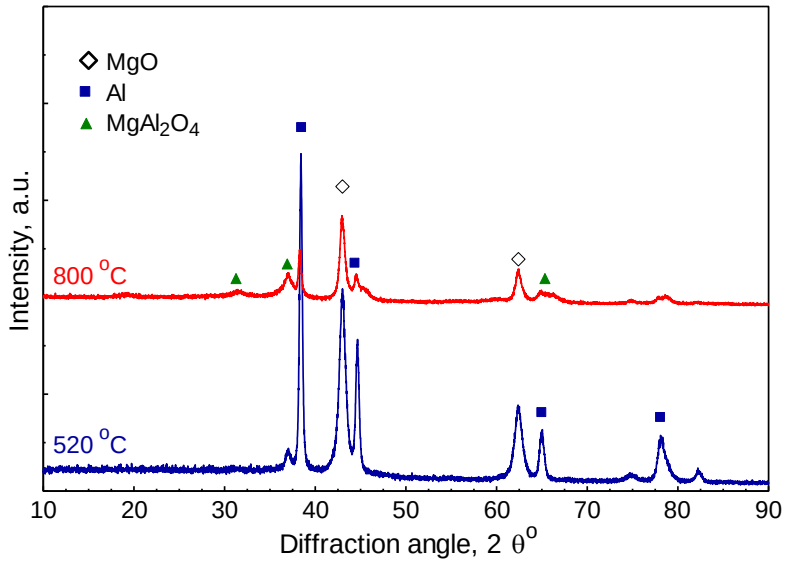

Figure 6.7 XRD pattern for the reaction products of mechanically alloyed Al-Mg powder quenched and recovered at 520 °C and 800 °C.

XRD results for both powders consistently indicate selective low-temperature oxidation of Mg, followed by oxidation of remaining aluminum, which causes formation of the ternary MgAl2O4 phase. A balanced global reaction (R1) for the alloy including 50/50 Al/Mg mass ratio is:

$$Al_{0.47}Mg_{0.53} + 0.6175 \cdot O_2 \rightarrow 0.295 \cdot MgO + 0.235 \cdot MgAl_2Mg_4 \qquad \text{(R1)}$$

Considering that selective oxidation of Mg occurs first, it is suggested to break the global reaction into two steps. The only oxide phase forming in the first step is MgO. In the second step, the product is MgAl2O4 with the MgO formed in the first step either remaining inert, or participating in the second step reaction. The two-step reaction can be expressed as:

$$Al_{0.47}Mg_{0.53} + aO_2 \rightarrow (0.53 - 0.235x)MgO + Al_{0.47}Mg_{0.235x} \quad \text{(R2)}$$

$$(0.53 - 0.235x)MgO + Al_{0.47}Mg_{0.235x} + bO_2 \rightarrow 0.295MgO + 0.235MgAl_2O_4 \quad \text{(R3)}$$

where $a=0.265-0.1175x$, $b=0.3525+0.1175x$, and x can vary between 0 and 1. If x=0, all magnesium present in the alloy oxidizes in the first step forming MgO. In the second step, a portion of the formed MgO reacts with aluminum and oxygen forming $MgAl_2O_4$. If x=1, it is assumed that all the MgO formed in the first step remains intact during the second reaction step, so that $MgAl_2O_4$ is produced by the reaction of unoxidized magnesium, aluminum, and oxygen. Any intermediate value of $0<x<1$ is possible. Even without knowing what the actual value of x is, breaking the global oxidation reaction into two steps is useful for interpreting the present results.

6.4.2 TG Data Processing and Location of the Heterogeneous Reaction Interface

Different reaction mechanisms (see Figure 6.8 and discussion below) were considered, assuming the reaction to occur at different interfaces, which change differently as a function of the reaction progress. Only measurements for spherical atomized powder were considered to simplify the interpretation of experiments. In all cases, a core-shell geometry is assumed for oxidation of spherical particles. In agreement with the XRD results shown in Figures 6.4 and 6.5, oxidation was assumed to proceed in two distinct steps: first selective oxidation of Mg was considered yielding MgO (Reaction (R2); top panels in Figure 6.8), followed by oxidation of both Al and remaining Mg yielding $MgAl_2O_4$

(Reaction (R3); bottom panels in Figure 6.8). To further streamline the analysis, only cases with x=0 or x=1 were considered.

Three possible reaction sequences were considered, referred to as Cases I, II, and III in Figure 6.8. For all scenarios, the particles include a metallic core with a void and an oxide shell. The reaction interface is shown by bold dashed line. For Case I, both Mg and Al oxidation occur at the internal core-shell interface between the metallic core and growing oxide shell. For Case II, selective oxidation of Mg occurs at the internal metal-oxide interface, while second step reaction takes place at the external interface of the oxide shell and gas. Finally, for Case III, both step 1 and 2 reactions occur at the external interface of the oxide shell and gas.

In other words, for Case I, it is assumed that both oxidation of Mg and Al are rate limited by the inward diffusion of the oxidizer (oxygen ions). For Case II, selective oxidation of Mg is rate limited by the inward diffusion of oxidizer, while formation of $MgAl_2O_4$ is limited by outward diffusion of metal ions. Finally, in Case III all reactions are assumed to be rate limited by outward diffusion of metal ions.

To identify which mechanism describes the results best, the approach developed earlier [92, 127, 146] was adapted here. The weight gain measured in a TG experiment as a function of time or temperature for the powder sample was split among powder particle size bins:

$$\frac{dM}{dT} = \sum_n \frac{dm_n}{dT} = \sum_n \frac{A_n j_n dt}{dT} = \frac{j}{\beta} \sum_n A_n \tag{6.1}$$

where M is the total powder mass, T is temperature, m is the mass of particles in an individual particle size bin, t is time, $\beta=dT/dt$, is the heating rate, A is the area of the reactive interface, and j is mass flux. Index n numbers particle size bins.

The change in the reactive surface area for each size bin, $A_n = 4N_n\pi r_{n,i}^2$, is determined for each of the cases illustrated in Figure 6.8 using the radius of the respective reactive interface, $r_{n,i}$, and its change during oxidation and accounting for number of particles in each bin, N_n (from the measured size distribution). A key assumption is that the mass flux j of the reaction rate limiting diffusing species at the reaction interface is the same for all particles. Solving diffusion equation for a spherical particle with a growing oxide shell (appropriate for any of the reaction scenarios shown in Figure 6.8), and assuming that mass fraction of the diffusing species changes from 1 to 0 across the oxide layer, one obtains:

$$\dot{m} = 4\pi r_i^2 j = \frac{4\pi\rho D}{\frac{1}{r_1} - \frac{1}{r_2}} \tag{6.2}$$

where r_1 and r_2 are inner and outer radii of the growing oxide layer, across which diffusion occurs; $\dot{m}$ is mass flow of the diffusing species; j is respective flux at the reactive interface; r_i, is the radius of the reaction interface, which is assumed to be equal to either at r_1 or r_2, depending on the specific mechanism shown in Figure 6.8; D is diffusion coefficient (generally defined by an Arrhenius kinetics), and ρ is density. Thus, for spherical particles, the flux depends on the radii r_1 and r_2 as:

$$j_{A,r=r_1} = \frac{r_1 r_2}{r_i^2} \frac{\rho D}{r_2 - r_1} \tag{6.3}$$

Note that index n marking an individual size bin is removed for brevity in Eg (3), although both flux values and radii are specific for a given particle size. Thus, the measured mass uptake for each assumed reaction model was distributed proportionally to the function $A_i \cdot \frac{r_1 r_2}{r_i^2} \frac{\rho D}{r_2 - r_1} \sim \frac{r_2 r_1}{r_2 - r_1}$ accounting for the effect of particle geometry on the mass flux.

TG measurements were performed for two size fractions of the same powder (cf. Figure 6.2). For each reaction mechanism, shown in Figure 6.8, the TG data were distributed among all particles as described above.

It is important that the size distributions of the two size fractions were not the same, but included an overlapping range of particle sizes. Oxidation processes, in terms of changing mass of individual particles or oxide thickness as a function of temperature, were compared to each other for particles within that overlapping particle size range for both powders. It was assumed that the oxidation mechanism resulting in the most similar oxidation behavior for such particles represented the experiment most accurately. Therefore, the location of the reaction interface was identified.

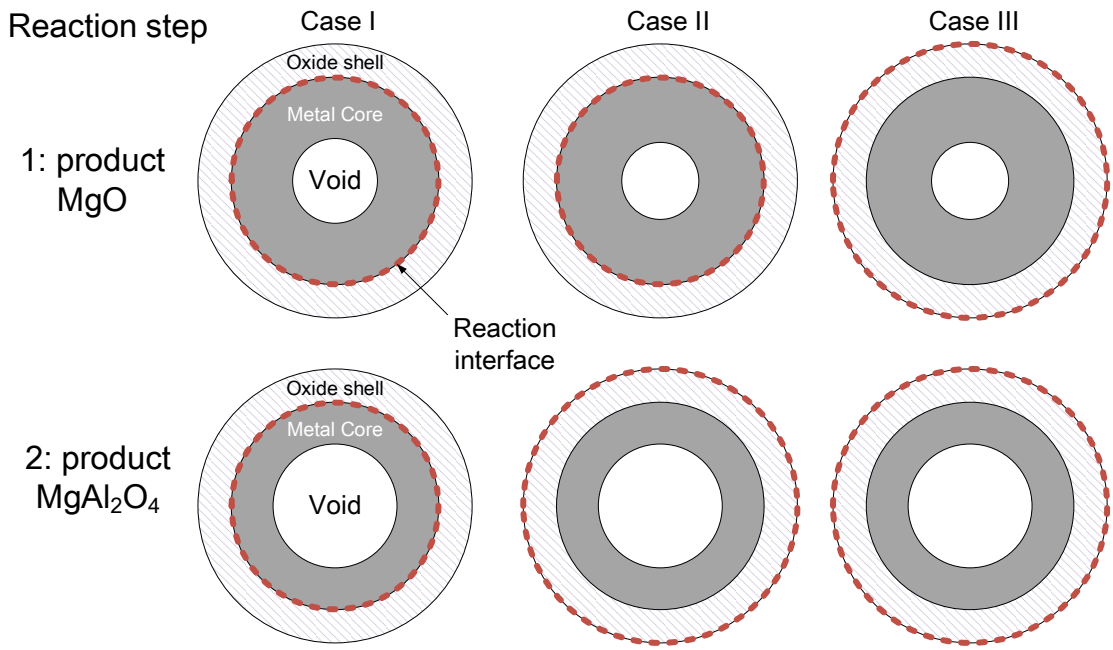

Figure 6.8 Schematic diagram illustrating different reaction mechanisms: Case I. Both Mg and Al oxidize at the interface between metallic core and oxide shell. Case II. Mg oxidizes at the interface of metallic core and oxide shell and Al oxidizes at the outward boundary of the oxide shell. Case III. Both Mg and Al oxidize at the outward boundary of the oxide shell.

For each reaction mechanism considered, the radii r_1 and r_2 are continuously tracked as a function of temperature for all particles and their values are used to distribute the measured weight gain among particles of different sizes. The measured TG traces used in this analysis for both coarse (as received) and fine (sieved) powder size fractions are shown in Figure 6.9. The inset in Figure 6.9 expands the temperature range, for which the most significant differences were observed between weight gains for different powder size fractions.

Using the particle size distributions shown in Figure 6.2 and accounting for different reaction mechanisms shown in Figure 6.8, the data shown in Figure 6.9 were processed to calculate mass changes for all particle sizes as a function of the reaction

progress, or as a function of temperature. For each individual particle size, different reaction mechanisms yielded different dependencies of mass on time (or temperature); these dependencies were also different for particles of the same initial size but belonging initially to coarse or fine size fractions of the oxidizing powder.

Comparing differences in the obtained mass as a function of time for the particles of the initially the same sizes present in both powders (i.e., belonging to the overlapping range of particle sizes), enabled us to identify the most likely oxidation mechanism.

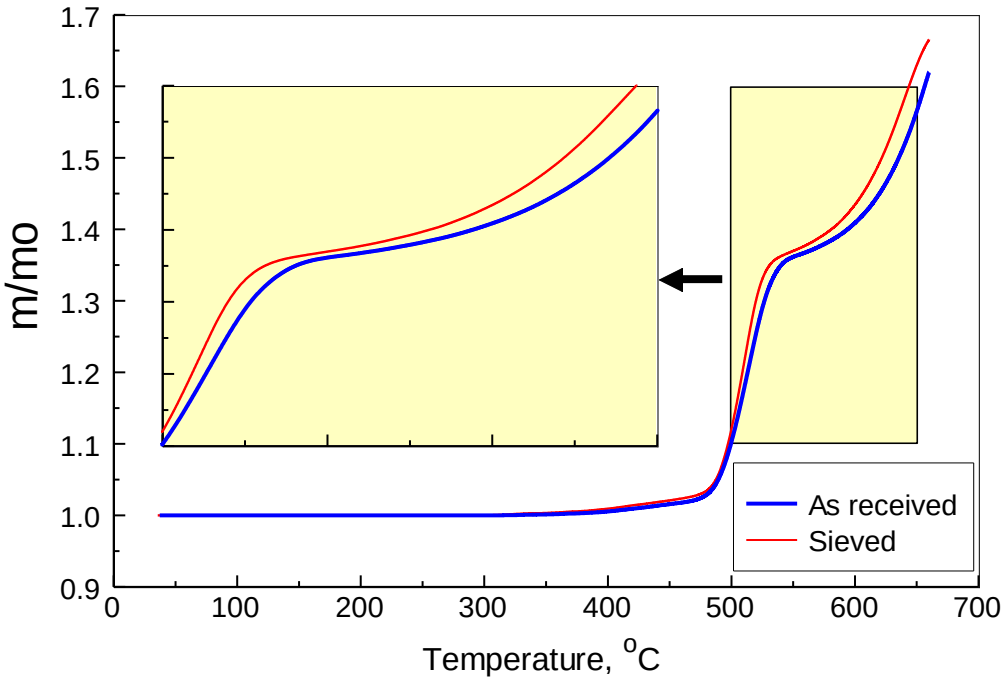

Figure 6.9 TG traces for two size fractions of the atomized spherical Al-Mg alloys powder oxidizing in oxygen; heating rate was 5 K/min.

Quantitatively, following previous work [92, 127, 146], functions of mass as a function of time for all overlapping particle sizes were compared to each other using parameter, Er_n, calculated for each particle size bin, n:

$$Er_n = \frac{1}{m_{n,0}} \sqrt{\frac{\sum_{k=1}^{K} \left(m_{n,\mathrm{k}}^{Coarse} - m_{n,\mathrm{k}}^{Fine} \right)^2}{K}} \tag{6.4}$$

where summation is done for all K time steps for the measurements shown in Figure 6.9, and $m_{n,\mathrm{k}}^{Coarse}$ and $m_{n,\mathrm{k}}^{Fine}$ are the weight changes for coarse and fine powder fractions respectively, corresponding to the k^{th} time step. Parameter Er_n quantifies discrepancy between oxidation scenarios for the particles of the same initial size; it should be minimized for the reaction model most likely describing actual oxidation processes. Values of Er_n implied by each model are plotted in Figure 6.10 for all the overlapping particle sizes for two powder fractions. Parameter Er_n is minimized for Case I, when both oxidation reactions are assumed to occur at the internal interface between metallic core and oxide shell. Thus, Case I describes the reaction best for the Al-Mg alloys and oxidation of both Mg and Al is governed by the inward diffusion of oxidizer for both reaction sequences. This is similar to the oxidation mechanism identified for pure Mg[146], but is different from the oxidation mechanism for pure Al [92].

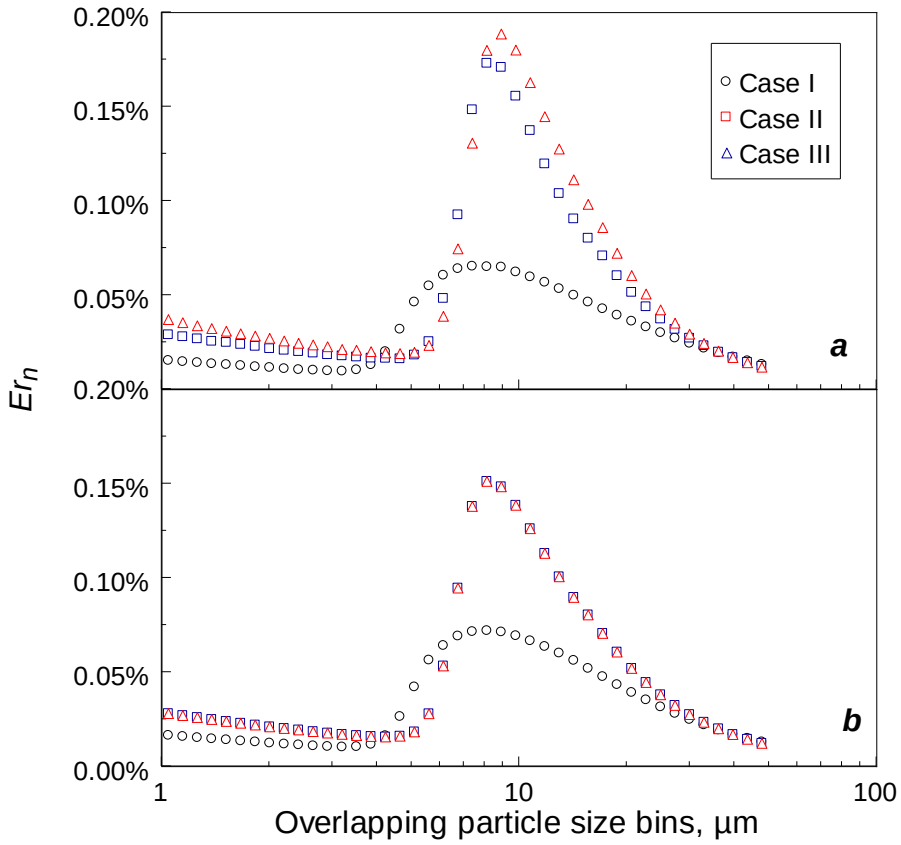

Figure 6.10 Cumulative discrepancy measure calculated using Equation (6.1) for data on oxidation of spherical Al-Mg alloys in oxygen processing using different reaction models: a. x=0 b. x=1.

6.4.3 Reaction Kinetics

TG measurements were repeated at different heating rates for the spherical atomized alloy powder, as shown in Figure 6.11. The traces shift consistently to higher temperatures at greater heating rates. These measurements were used to identify the apparent activation energy of oxidation as a function of the reaction progress [129-131].

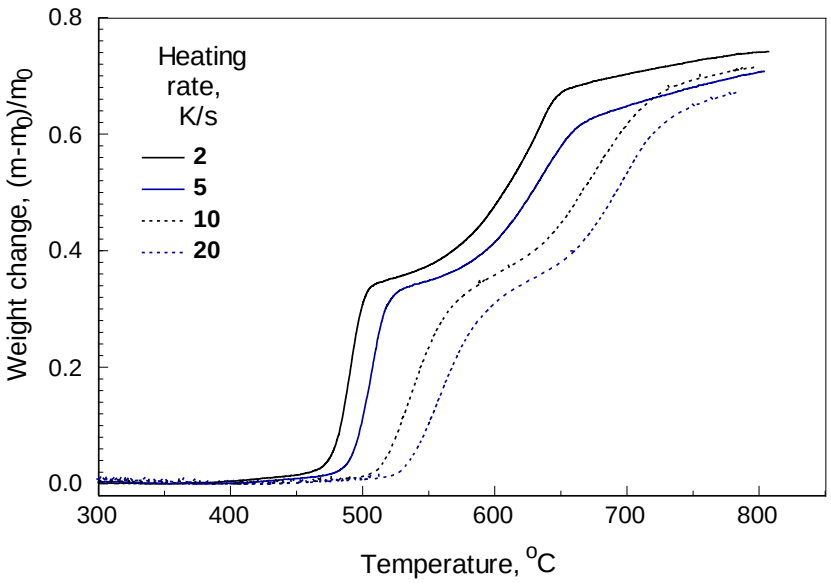

Figure 6.11 TG traces for atomized spherical alloys powder oxidized at different heating rates.

A model free isoconversion method [96, 97] was employed. Reaction rate was considered as a function of a kinetic triplet, including activation energy, *E*, pre-exponent, *C*, and a function of reaction progress, $f(\alpha)$:

$$\frac{d\alpha}{dt} = C \cdot \exp\left(-\frac{E}{R_{gas}T}\right) \cdot f(\alpha) \qquad (6.5)$$

At each given value of the reaction progress, α, the value of activation energy, E_α is determined from the slope of a plot of $\ln\left(\frac{d\alpha}{dt}\right)$ against inverse temperature, without specifying $f(\alpha)$. Each plot uses TG measurements performed at different heating rates, and

thus achieving different values of α at different temperatures. A specific processing algorithm described in Reference [97] was used.

First, measurements presented in Figure 6.11, and representing oxidation of the entire powder sample were used. The resulting activation energy is presented in Figure 6.12 as a function of the increasing mass of powder, considered here as an indicator of the reaction progress. For the first rapid mass increase step, observed in Figure 6.11 around 470 – 550 ºC for different heating rates, the relative mass increase changes approximately from 0.1 to 0.3, and the apparent activation energy decreases from above 200 to below 50 kJ/mol. As the reaction proceeds to the next oxidation stage, the activation energy in Figure 6.12 increases stepwise and remains approximately stable around 190 kJ/mol.

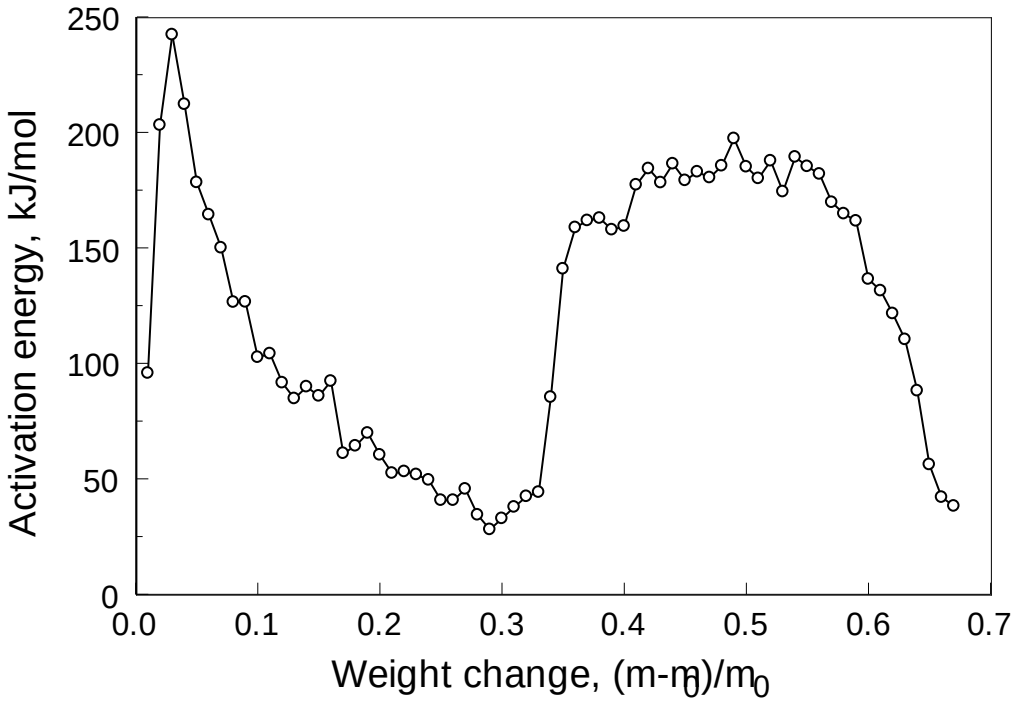

Figure 6.12 Apparent activation energy of oxidation for an Al-Mg alloy powder in oxygen as a function of reaction progress defined through the sample weight change.

To understand why the apparent activation energy decreases during the initial reaction stage consider a combination of the effect of different oxidation rates for particles of different sizes (unaccounted for by the present processing) and a sequence of selective oxidation processes for magnesium and aluminum. For finer particles, with a relatively large surface area available for oxidation, but small metal mass, all magnesium may be selectively oxidized at lower temperatures. Thus, oxidation of aluminum begins at a lower temperature as well. Therefore, in a range of temperatures, oxidation of aluminum for finer particles occurs simultaneously with selective oxidation of magnesium in coarser ones. This may result in a misleading value for the apparent activation energy. The above reasoning is supported by an estimate shown in Figure 6.13. One of the plots in Figure 6.13 is a measured TG trace. The second plot shows particle size bins, for which all Mg is selectively oxidized by a specific temperature. For simplicity, in this estimate it is assumed that x=0, i.e., all magnesium is oxidized in the first reaction step, Reaction (R2). For the smallest size considered, 1 μm, all Mg is consumed at a very low temperature, close to 470 ºC. Thus, aluminum oxidation begins for 1-μm particles just above 470 ºC. When the first rapid weight gain stage is finished, just above 500 ºC, magnesium is completely oxidized in all particles smaller than approximately 15 μm. Clearly, the apparent activation energy obtained for the entire powder shown in Figure 6.12 represents different processes for different particle size bins.

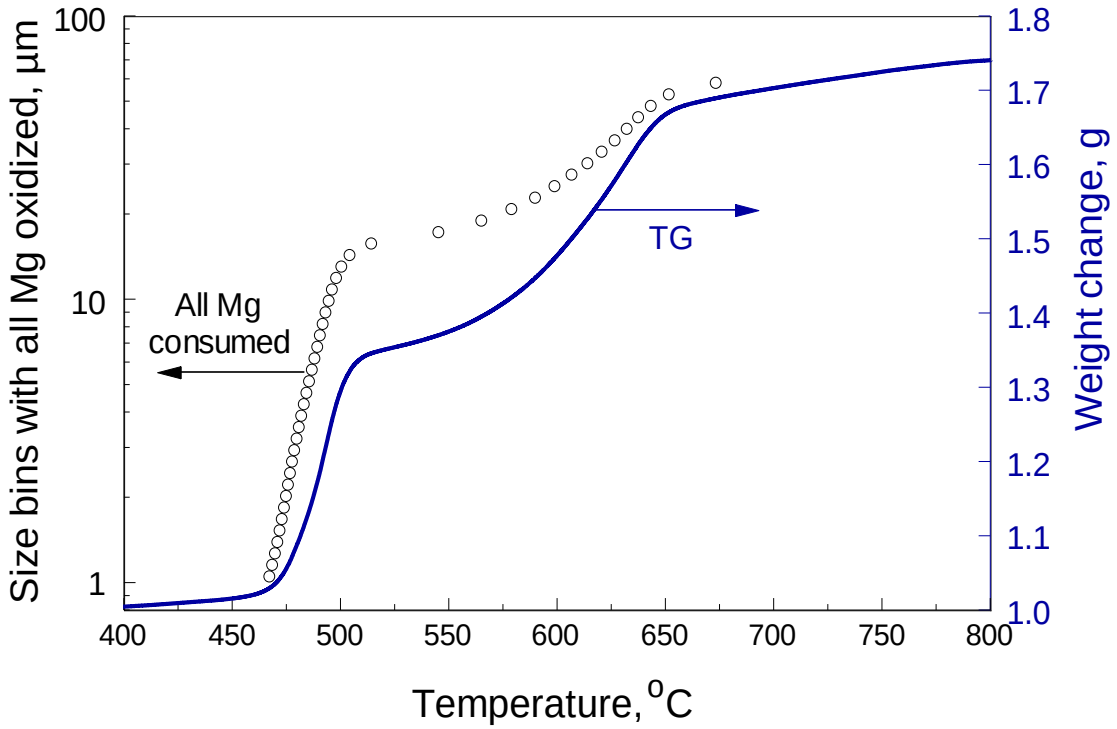

Figure 6.13 Size bins with all Mg selectively oxidized vs. respective temperature (x=0) and the corresponding TG trace for a spherical Al-Mg alloy in oxygen.

The processing of TG traces described above and involving re-distribution of the measured weight gain among individual particle size bins enables one to avoid interference between different oxidation reactions occurring simultaneously for particles of different sizes.

TG traces representing the oxidation of individual particle size bins were thus obtained considering the reaction mechanism shown as case I in Figure 6.8. For each size bin, the isoconversion processing was applied. First, following the approach used to obtain result shown in Figure 6.12, sample weight change was treated as reaction progress indicator. The activation energies obtained for different particle sizes are shown in Figure 6.14 for both reaction scenarios: a: x=0 (Mg is fully oxidized in Reaction (R2)) and b: x=1.

Qualitatively, it is still observed that the apparent activation energy sharply increases, suggesting a step-wise change in the oxidation mechanism. The step occurs at different values of weight change for different particle sizes, suggesting that weight may not be a convenient progress indicator for this reaction.

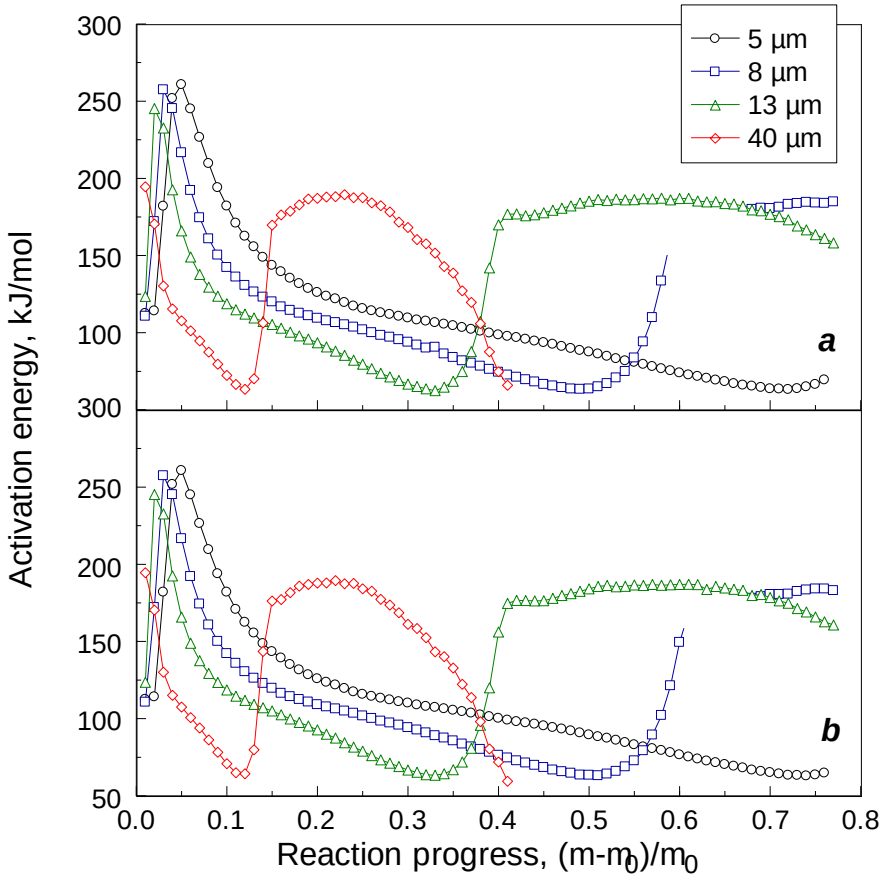

Figure 6.14 Apparent activation energy of oxidation for individual size bins of an Al-Mg alloy powder in oxygen as a function of reaction progress defined through the sample weight change. a: Selective oxidation of Mg is completed in Reaction (R2) (x=0); b: Minimized selective oxidation of Mg in Reaction (R2) (x=1).

Instead, the thickness of the grown oxide layer may serve as a more natural indicator of the reaction progress, assuming that the change in the oxidation mechanism occurs at a specific oxide thickness. The activation energies for several individual particle

size bins were thus obtained as a function of the oxide thickness as shown in Figure 6.15. Interestingly, all apparent activation energy trends merge together, suggesting a fairly narrow range of oxide thicknesses, for which the reaction mechanism changes. If all magnesium is assumed to be selectively oxidized in Reaction (R2), x=0, the jump in the activation energy occurs between thicknesses of 1.24 and 1.56 µm. For the scenario with x=1, the transition occurs for thicknesses between 1.20 and 1.52 µm.

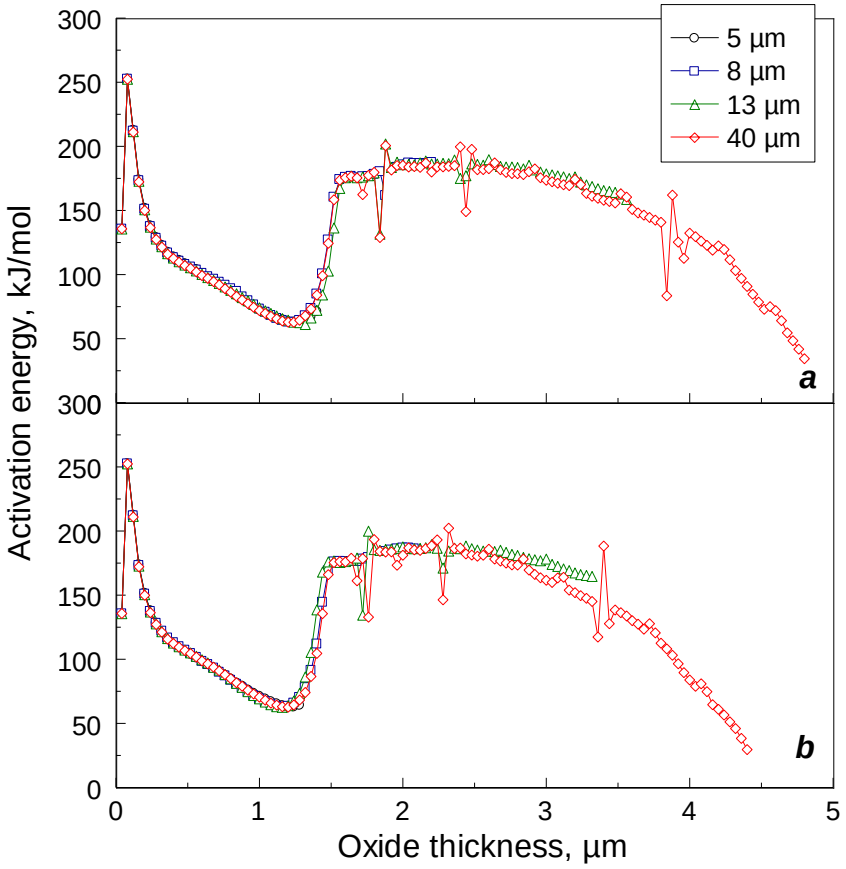

Figure 6.15 Apparent activation energy of oxidation for individual size bins of an Al-Mg alloy powder in oxygen as a function of reaction progress defined through the grown oxide thickness. a: Selective oxidation of Mg is completed in Reaction (R2) (x=0); b: Minimized selective oxidation of Mg in Reaction (R2) (x=1).

Although the result shown in Figure 6.15 does not enable one to readily distinguish between reaction scenarios with x=0 or x=1, it suggests rather clearly that the oxide thickness is, indeed a natural indicator of the reaction progress for oxidation of Al·Mg alloys. The abrupt change in the activation energy when thickness passes a range of 1.2 – 1.5 μm can be attributed to a switch over between Reaction (R2) and Reaction (R3). For Reaction (R2), activation energy falls rapidly at very thin initial oxide layer thickness. It continues to diminish at a lower rate when the thickness increases above approximately 0.24 μm. It is likely that the reduction in the apparent activation energy is associated with cracks and defects produced in the growing MgO layer.

For the second step, Reaction (R3), resulting in the formation of the spinel group MgAl2O4, the activation energy remains nearly constant around 180 kJ/mol, until the oxide layer thickness exceeds ca. 3 μm. At greater oxide thicknesses, the activation energy appears to decrease, probably also due to defects in the thicker oxide shell.

For both reaction steps, the apparent activation energy values characterize diffusion of oxygen ions through a thickening oxide shell.

6.5 Conclusion

The oxidation of both commercial spherical Al-Mg alloys and mechanically alloyed Al-Mg powder in oxygen was investigated using thermo-gravimetry. Two oxidation stages were observed for both powders. First, selective oxidation of magnesium resulting in formation of an MgO shell is observed. The second step reaction generates spinel, $MgAl_2O_4$. Both reactions occur at the interface between the metal alloy core and the oxide shell and thus are rate-limited by inward diffusion of oxygen ions. Voids are formed in the oxidized particles due to the re-distribution of material within the metal core.

The switch over between reaction steps occurs when the oxide shell grows above a certain thickness between 1.2 and 1.5 μm. The apparent activation energy of selective oxidation of Mg falls rapidly from 250 to 130 kJ/mol when the oxide thickness increases to ca. 0.24 μm. The activation energy continues to diminish down to approximately 65 kJ/mol as the oxide continues to thicken to 1.2 μm. For the second oxidation step, the activation energy remains nearly constant around 180 kJ/mol while the oxide shell grows up to approximately 3 μm. At greater oxide thicknesses, a slow decrease in the apparent activation energy is observed.

CHAPTER 7

OXIDATION OF NANO-SIZED ALUMINUM POWDER

7.1 Abstract

Oxidation of aluminum nanopowders obtained by electro-exploded wires is studied. Particle size distributions are obtained from transmission electron microscopy (TEM) images. Thermo-gravimetric (TG) experiments are complemented by TEM and XRD studies of partially oxidized particles. Qualitatively, oxidation follows the mechanism developed for coarser aluminum powder and resulting in formation of hollow oxide shells. Sintering of particles is also observed. The TG results are processed to account explicitly for the particle size distribution and spherical shapes, so that oxidation of particles of different sizes is characterized. The apparent activation energy is obtained as a function of the reaction progress using model-free isoconversion processing of experimental data. A complete phenomenological oxidation model is then proposed assuming a spherically symmetric geometry. The oxidation kinetics of aluminum powder is shown to be unaffected by particle sizes reduced down to tens of nm. The apparent activation energy describing growth of amorphous alumina is increasing at the very early stages of oxidation. The higher activation energy is likely associated with an increasing homogeneity in the growing amorphous oxide layer, initially containing multiple defects and imperfections. The trends describing changes in both activation energy and pre-exponent of the growing amorphous oxide are useful for predicting ignition delays of aluminum particles. The kinetic trends describing activation energies and pre-exponents in a broader range of the oxide thicknesses are useful for prediction of aging behavior of aluminum powders.

7.2 Introduction

Development of practical methods to prepare nano-sized aluminum powders [148-150] catalyzed research in new nano-energetic materials, including metal nanopowders, nano-thermites, and intermetallic systems [151-153]. Although many compositions have been prepared and characterized in the last two decades, nano-sized aluminum powder remains the main component for multiple energetic formulations of interest for propellants, explosives, and pyrotechnics [154-156]. For most such formulations, oxidation of nano-sized aluminum is the process affecting critically both aging and ignition phenomena. This explains an active and sustaining interest in understanding and quantitative characterization of reactions governing oxidation of nano-sized aluminum, e.g., see [26, 88, 102, 157-160]. In particular, oxidation similarities and differences between nano- and micron-sized powders need to be established. For example, widely discussed changes in the melting characteristics of nano-aluminum [151, 161] become significant for particles smaller than 10 nm and may not play an important role for most practical nano-powders with dimensions in the 100 nm range. However, it remains unclear whether mechanisms and kinetics developed for oxidation of coarse aluminum powders are directly transferrable for nano-sized particles.

Oxidation mechanism of micron-sized aluminum powders has been established relatively well [25, 31, 87]. It is generally agreed that the reaction is diffusion controlled. It is also agreed that the diffusion rates are heavily affected by the structure of the growing aluminum oxide film. The natural 2 – 4-nm thick oxide is amorphous; it transitions to γ-Al_2O_3 at elevated temperatures and growing oxide layer thickness [25, 31, 90, 162]. Further oxidation processes involve transformation of γ-Al_2O_3 to θ- and α-Al_2O_3 as

temperatures increase. It has been shown recently that the reaction occurs at the interface separating the growing alumina layer and gaseous oxidizer, and thus it is rate controlled by outward diffusion of aluminum ions [92, 127]. Detailed thermo-analytical measurements were reported and processed to establish kinetics of the respective oxidation processes [90, 162]. Reactions at early oxidation stages were addressed in particular, as most critical for modeling both ignition and aging phenomena [163]. A recent study [102] addressing oxidation of nano-sized aluminum mostly agrees with the above oxidation sequence. However, quantitative comparisons of oxidation rates and respective reaction kinetics are not available.

This work is aimed to characterize oxidation of aluminum nano-powders quantitatively. It is further desired to determine the kinetics of respective reactions and compare it directly to that reported for micron-sized aluminum powders.

7.3 Technical Approach

Oxidation of spherical aluminum nanopowders is characterized in thermo-analytical experiments, including differential thermal analysis (DTA) and thermo-gravimetry (TG). Partially oxidized particles are examined by transmission electron microscopy (TEM) and x-ray diffraction (XRD). The results of TG measurements are processed accounting for the particle size distribution obtained using TEM and taking into consideration location of the reaction interface at the outer surface of the growing alumina layer [92]. The model is illustrated in Figure 7.1. Aluminum is assumed to diffuse through the oxide shell, with new oxide growing at the outside of the existing shell. As the aluminum is consumed, a void is assumed to grow in the aluminum particle core. In other words, aluminum is assumed to adhere to the inner surface of the growing oxide shell. Clearly, the validity of

the present approach diminishes as the oxidizing particles sinter and/or change their shapes. However, this analysis is useful in the early stages of oxidation, which are particularly important for analysis of both ignition and aging processes.

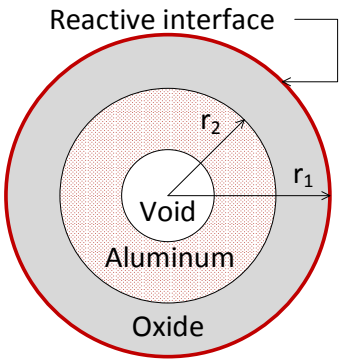

Figure 7.1 Schematic diagram of the geometry assumed by the oxidation model.

To process TG data, the weight gain measured as a function of time or temperature for the entire powder is split among powder particle size bins:

$$\frac{dM}{dt} = \sum_i \frac{dm_i}{dt} = \sum_i A_i j_i = j \sum_i A_i \qquad (7.1)$$

where M is the total powder mass, T is temperature, m is the mass of particles in an individual particle size bin, t is time, A is the area of the reactive interface, and j is mass flux. Index i numbers particle size bins. The change in the reactive surface area for each size bin, $A_i = 4N_i\pi r_i^2$, is determined accounting for number of particles in each bin, N_i (from the measured size distribution), radius of the respective reactive interface, r_i, and for its change during oxidation. For the present reaction model, r_i=r_1 (see Figure 7.1). The

measured change of mass for each bin is converted into change in its respective surface area of the reaction interface.

For micron-sized particles, for which oxide layer is much smaller than the particle radius, the effect of radius on the flux was neglected, so that the flux could be removed from under the summation sign in Equation (7.1). In that case, the mass uptake for each size bin is directly proportional to its reactive surface area, A_i.

In this work addressing oxidation of nano-sized particles, the effect of particle radius on the flux cannot be neglected. Consider the solution of diffusion equation for a spherical particle with a growing oxide shell, written assuming that pure Al and pure O_2 gas are on the inner and outer sides of the oxide layer, respectively:

$$\dot{m}_{Al} = 4\pi r_1^2 j_{Al,r=r_1} = \frac{4\pi\rho D}{\frac{1}{r_1} - \frac{1}{r_2}} \tag{7.2}$$

where $\dot{m}_{Al}$ is mass flow of aluminum; $j_{Al,r}$ is respective flux at a radial location, r; D is diffusion coefficient (generally defined by an Arrhenius kinetics), and ρ is density. Outer and inner radii of the oxide shell are labeled as r_1 and r_2, respectively (see Figure 7. 1). The flux, j, is taken for $r=r_1$, which is the radius of the reaction interface. Thus, for spherical particles, the flux depends on the radii r_1 and r_2 as:

$$j_{Al,r=r_1} = \frac{r_2}{r_1} \cdot \frac{\rho D}{r_2 - r_1} \tag{7.3}$$

With oxide layer thickness, r_2-r_1, comparable to the radii r_1 and r_2, the flux becomes dependent on the particle size. Thus, j_i can no longer be removed from under the summation sign, as was done in Equation (7.1). Note that index *i* marking an individual size bin was removed for clarity in Equation (7.3), although both flux values and radii are specific for a given particle size, or size bin *i*. Thus, instead of distributing the mass uptake among different size bins proportionally to their respective surface areas, A_i, here, the mass uptake is distributed proportionally to the function $A_i \cdot \frac{r_2}{r_1}\frac{1}{r_2-r_1} \sim \frac{r_2 r_1}{r_2-r_1}$, equivalent to the surface area of a particle with the geometric mean radius, divided by the oxide layer thickness, which accounts for the effect of particle geometry on the mass flux.

TG traces representing oxidation of particles of each given size bin are obtained for different heating rates and processed using a model-free isoconversion technique [97, 164] to obtain activation energy as a function of the reaction progress. This processing explicitly accounts for the effect of particle size distribution on the TG measurements. Once the activation energies are obtained, the reaction model represented by Figure 7.1 is considered to identify the pre-exponent and thus to fully quantify the rate of oxidation. The obtained reaction kinetics for aluminum nanopowders is finally compared to that reported earlier for coarser aluminum particles.

7.4 Experimental Details

Spherical aluminum nanopowders were prepared in argon using electro-exploded wires [148, 149]. The powder was held at a reduced oxygen pressure for 72 hours for passivation. Particles were examined using a JEOL JEM-100 CXII TEM. Partially oxidized powders were also examined by TEM; in addition, XRD (XRD-6000 by

Shimadzu using Cu K_α radiation) was used to determine the phases formed during oxidation. DTA and TG measurements performed in air at a fixed heating rate of 10 K/min used a Netzsch STA 449F3; additional TG measurements in an argon/oxygen gas mixture at varied heating rates were performed using a TA Instruments TA Q5000-IR. Surface area of the prepared powder was characterized using a BET-analyzer by Boreskov Institute of Catalysis, Siberian Branch, Russian Academy of Sciences. The amount of active aluminum was determined by reacting the powder with an aqueous solution of sodium hydroxide and measuring the volume of the released hydrogen gas [101].

7.5 Experimental Results

TEM images of as prepared nanoparticles are shown in Figure 7.2. The particles are mostly spherical, justifying use of the oxidation model shown in Figure 7.1. Particle sizes range from about 20 to 400 nm; a detailed particle size distribution obtained by processing multiple TEM images is shown in Figure 7.3. This distribution is used directly to process the TG measurements, as discussed above.

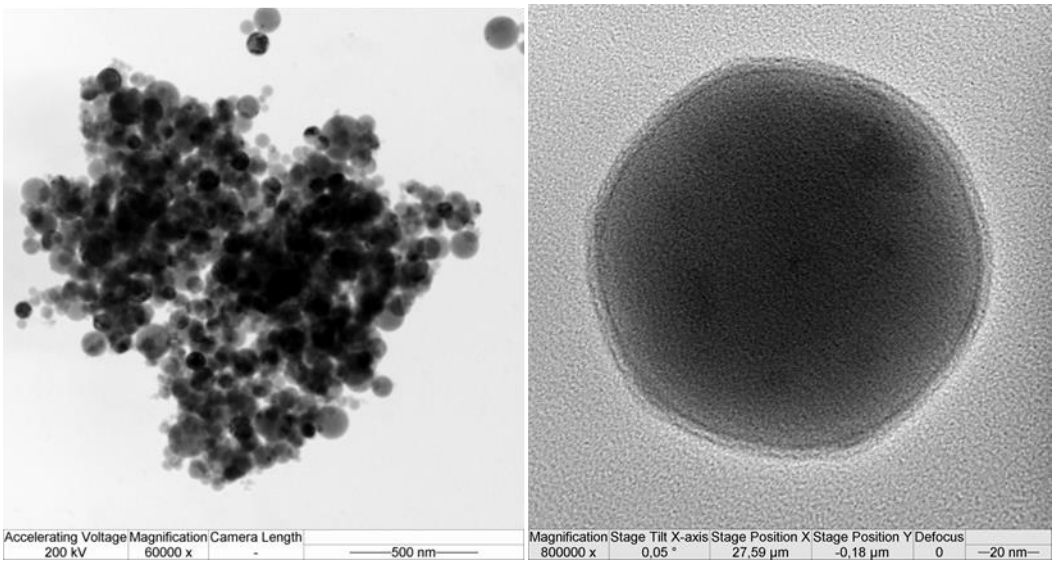

Figure 7.2 TEM images of the aluminum nanoparticles used in experiments.

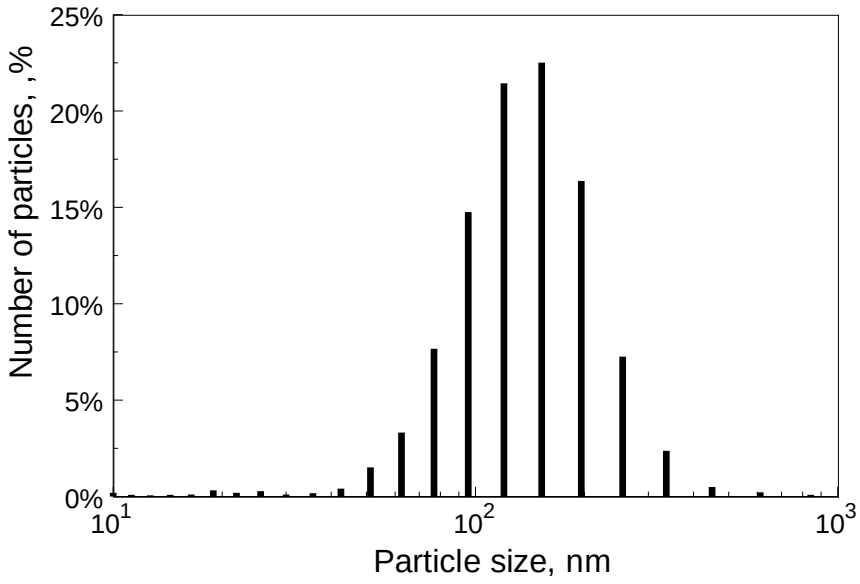

Figure 7.3 Particle size distribution obtained from TEM images.

Results of TG measurements are illustrated in Figure 7.4. An initial weight loss is observed, most likely associated with dehydration of the surface aluminum oxide. The

measurements are consistent with earlier reports on oxidation of micron- and nano-sized aluminum powders [25, 26, 102]. A rapid acceleration of the oxidation rate is observed around 800 K, prior to aluminum melting, when amorphous oxide transforms into γ-Al_2O_3. A DTA trace omitted here for brevity, shows an exothermic peak corresponding to the accelerated mass increase, followed by a small endothermic peak showing melting. At higher temperatures, reaction rate accelerates further, again in agreement with the earlier reports [25, 26, 102] assigning that acceleration to thermally activated growth of transition alumina polymorphs. The TG traces shift to higher temperatures at greater heating rates, as is expected for a thermally activated reaction.

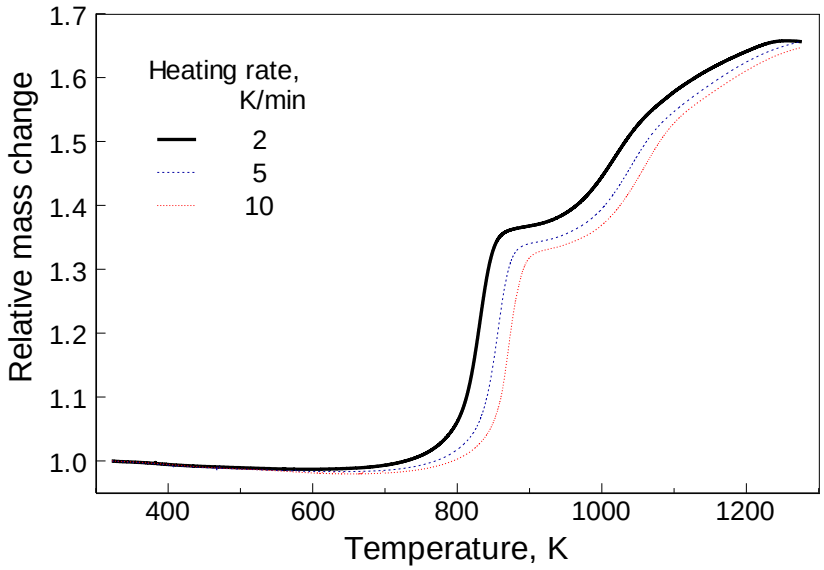

Figure 7.4 Mass gain for an oxidizing aluminum nanopowder heated at different heating rates in argon-oxygen gas mixture.

XRD patterns for different powders are shown in Figure 7.5. The as-prepared passivated powder contains various polymorphs of $Al(OH)_3$, indicating hydration of the natural alumina. The water is lost upon initial heating in TG experiments, resulting in the

observed small weight loss. The quenched samples were collected from experiments performed in air at the 10 K/min heating rate. Consistently with earlier results for coarser aluminum [25, 31], there are no well resolved peaks of alumina for the sample quenched at 823 K. Thus, only amorphous oxide is expected to be formed at lower temperatures. Again, consistently with earlier work, peaks of γ-Al_2O_3 and other transition alumina polymorphs are seen in the XRD pattern of the sample quenched at 923 K. Note that α-Al_2O_3 peaks are also observed, most likely indicating its formation during cooling of the partially oxidized powder. Finally, at 1183 K, the only oxide polymorph remaining is α-Al_2O_3. The XRD patterns generally confirm that oxidation of nano-sized aluminum particles results in the formation of the same sequence of alumina polymorphs as reported to form upon oxidation of coarser aluminum powders [25, 29, 31, 89, 90, 162].

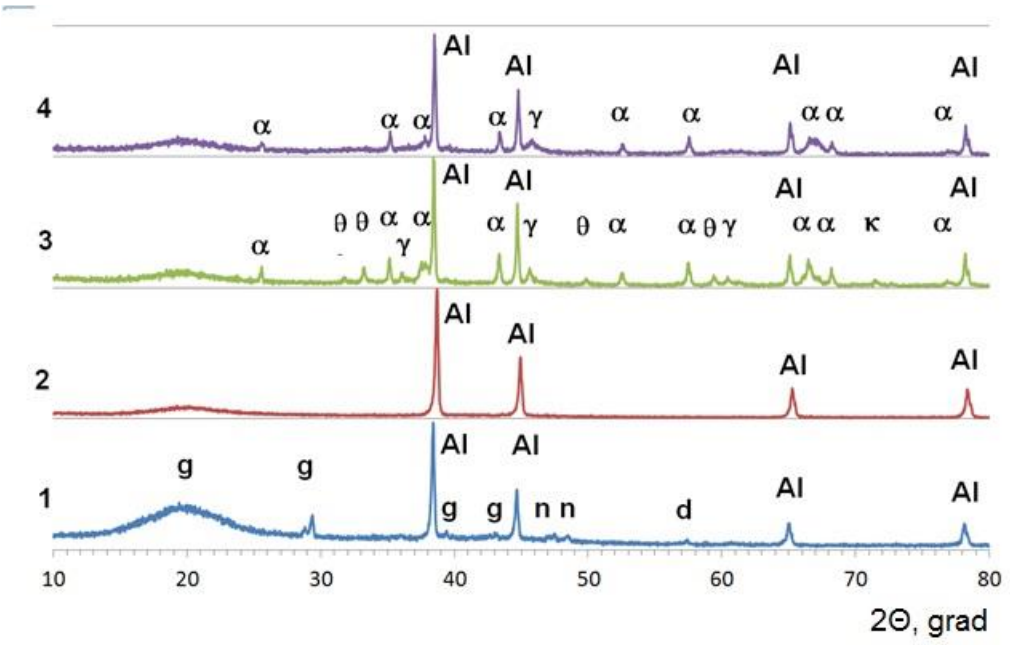

Figure 7.5 XRD patterns showing phases formed in partially oxidized aluminum powders recovered from different temperatures: 1: as prepared powder, 2: quenched at 823 K; 3: quenched at 923 K; 4: quenched at 1183 K. For pattern 1: letters *g*, *n*, and *d* show different polymorphs of $Al(OH)_3$. For patterns 2 – 4: Greek letters show respective polymorphs of Al_2O_3.

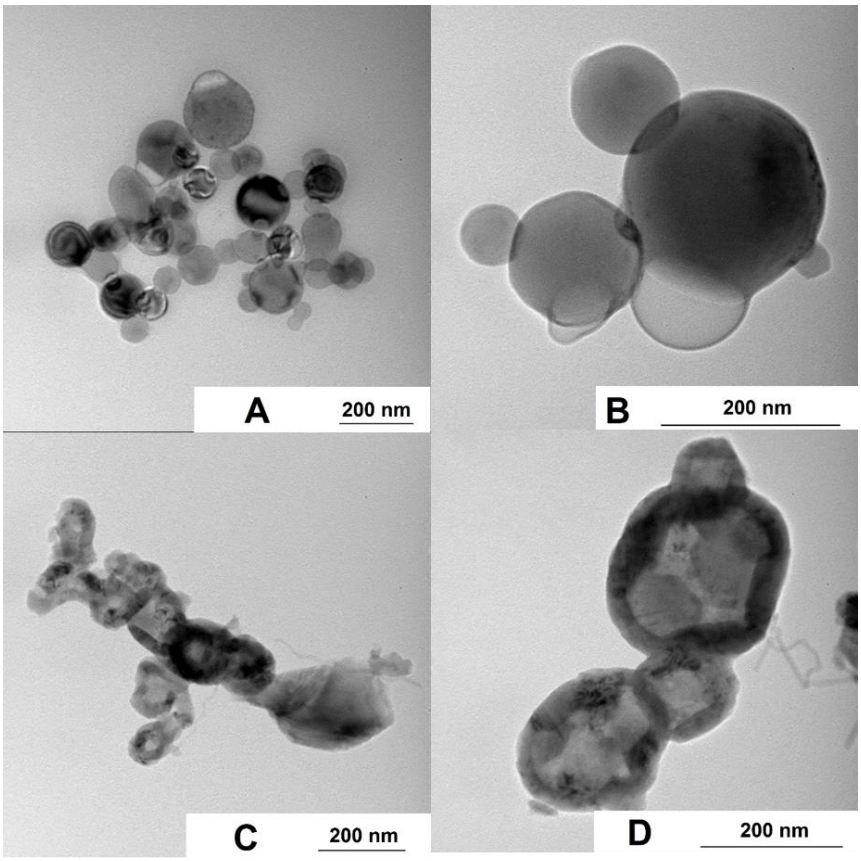

Figure 7.6 TEM images of partially oxidized aluminum particles quenched at different temperatures. Images A and B show particles quenched at 823 K; images C and D show particles quenched at 923 and 1183 K, respectively.

TEM images of partially oxidized particles are shown in Figure 7.6. As for XRD analyses, these particles were oxidized in air and heated at 10 K/min. At 823 K, the particles largely retain their spherical shapes. Some particles are observed to sinter forming inter-particle bridges. For some particles, distribution of aluminum changes causing formation of cavities. Several particles are observed to be attached to aluminum oxide caps; such caps most likely represent the oxide present in the starting metal wires used to prepare the nanopowder. The structure of particles quenched at 923 K changes substantially. All particles appear to contain a relatively thick oxide layer and a cavity.

The presence of cavities is supported by mapping aluminum concentration using energy-dispersive x-ray spectroscopy (details omitted for brevity). The formation of cavities is qualitatively consistent with the oxidation model adopted to process TG measurements and shown in Figure 7.1. Although particles mostly retain their spherical shapes, most particles are now fused together. Both oxide layer thickness and cavity size grow further for particles quenched at 1183 K.

Splitting the measured TG traces among different particle size bins shown in particle size distributions in Figure 7.3, enables one to predict how the oxide thickness increases with temperature for particles of different sizes. These predictions are illustrated in Figure 7.7. Finest, 10-nm particles are predicted to be fully oxidized at temperatures close to 730 K. The thickness of the grown oxide layer is close to one half of the initial particle diameter. Larger particles are fully oxidized at increasingly higher temperatures. Note that the oxide layer is predicted to grow at the outer surface of the existing shell; thus the size of the particle continuously increases, while a cavity is growing inside. In addition, the thermal expansion is taken into account for both metal core and the oxide shell. Because of an increase in the particle diameter as a function of temperature, the thickness of the oxide layer for the fully oxidized particles from larger bin sizes become substantially smaller than the half of the initial particle diameter.

A sudden reduction in the oxide thickness observed at 770 K represents re-adjustment of the calculated thickness as a result of polymorphic phase transition from amorphous to a higher density γ-Al_2O_3.

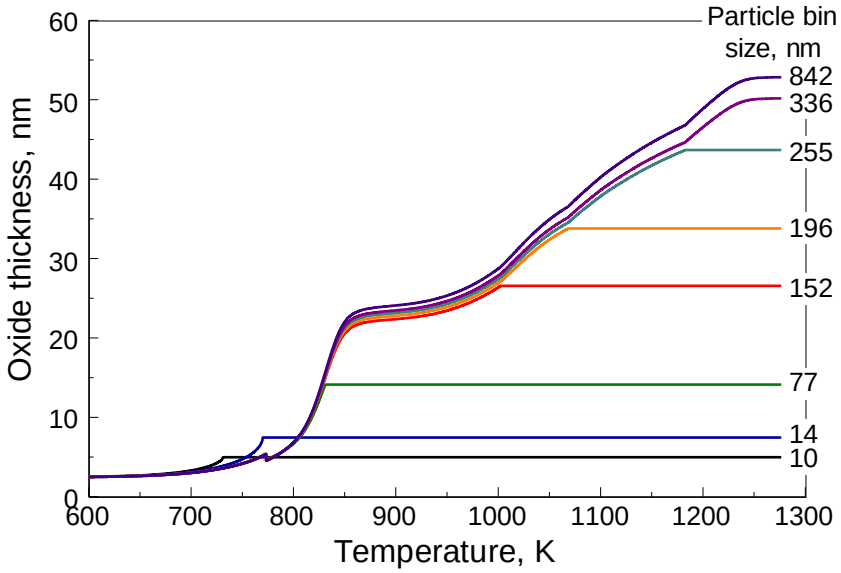

Figure 7.7 Thickness of the oxide layer grown on particles of different sizes as a function of temperature when the powder is heated at 10 K/min obtained as a result of splitting the measured TG trace among different powder size bins. Particle bin size represents the initial particle diameter.

Predicted oxide thickness as shown in Figure 7.7 was compared to that measured from the TEM images acquired for particles quenched at different temperatures. Diameters of quenched particles observed in TEM images were compared to the diameters expected to be produced at the respective temperatures for the partially oxidized particles belonging to different particle size bins. The bin, for which the diameters matched was then selected for each image, so that the thicknesses of the calculated and observed in TEM oxide layers could be compared to each other directly. Results of such comparisons are shown in Figure 7.8. The match between the TEM and processed TG data is excellent, supporting the validity of the adopted oxidation model used to convert the measured mass increase into the oxide thickness.

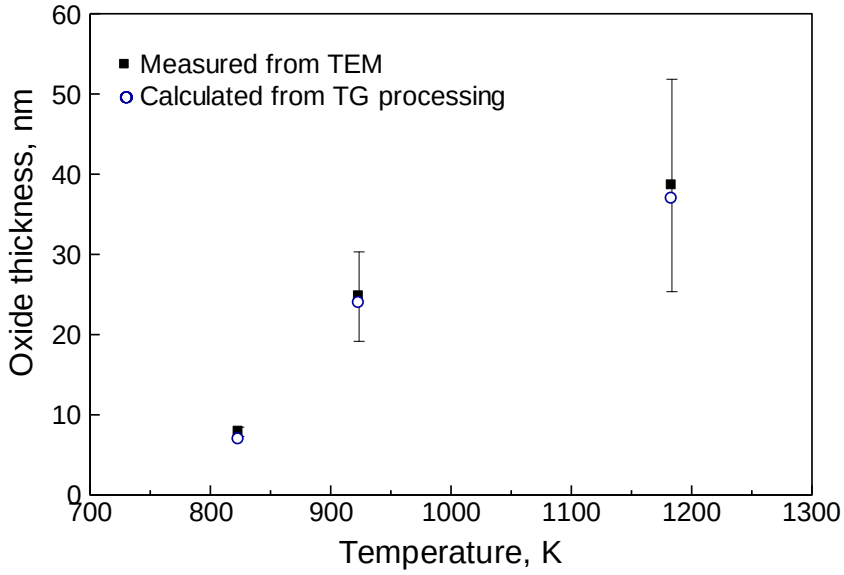

Figure 7.8 Thickness of the oxide layer for different partially oxidized particles measured from TEM images and respective thickness of the oxide layer calculated to form on particles of respective sizes using the oxidation model shown in Figure 7.1 and splitting the measured TG trace among different powder size bins.

7.6 Oxidation Kinetics for Nano-Sized Aluminum Particles

Thickness of the grown oxide layer was considered as a convenient indicator of the reaction progress. Unlike mass increase, oxide thickness can be used to gauge the degree of oxidation for particles of different sizes. Model-free isoconversion processing [97] was applied to TG curves assigned to individual particle size bins. Initial oxide thickness was assumed to be 2.5 nm [62, 95]. The processing was performed separately for the portions of the curves describing growth of amorphous alumina, at temperatures below 770 K, and growth of transition alumina polymorphs, principally, γ-Al_2O_3, above that temperature. The temperature, at which this transition occurs was fixed for simplicity in calculations using the oxidation model shown in Figure 7.1 and transforming the measured TG trace

into individual traces for different size bins. A more realistic model should account for both temperature and thickness of the grown oxide layer [25, 94, 165, 166] to describe this transition with a greater accuracy.

Apparent activation energy as a function of the oxide thickness for growth of amorphous oxide, E_{amorph}, is shown in Figure 7.9 for several individual particle size bins. The results for different size bins are consistent among themselves and show a rapid increase in the activation energy followed by its stabilization at about 155 kJ/mol. The change in the activation energy, in kJ/mol is well described by the following curve-fitting function:

$$E_{amorph} = 154.2 - \frac{1.8 \cdot 10^6}{h^{11.1}} \tag{7.4}$$

where h is oxide thickness in nm. The above expression is only valid for oxide thicknesses exceeding 2.5 nm, which is the thickness assumed to represent the initial natural oxide layer.

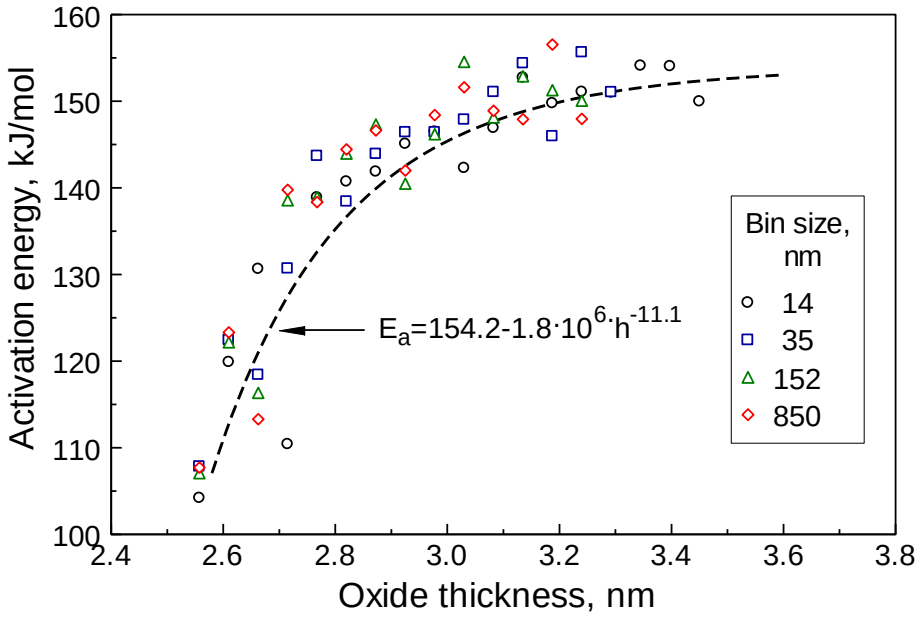

Figure 7.9 Apparent activation energy characterizing growth of amorphous alumina obtained from model-free isoconversion processing of experimental data and considering different particle sizes.

Once the activation energy, *E*, as a function of reaction progress is identified, an explicit oxidation model is used to determine the respective value of the pre-exponent. Considering oxidation of a spherical particle with an oxide shell, as given by Equation (7.2), and assuming that $\rho D = C \cdot exp\left(-\frac{E}{RT}\right)$, the values of pre-exponent characterizing growth of amorphous alumina, C_{amorph}, were obtained as shown in Figure 7.10. The pre-exponent was separately obtained for different heating rates and for different particle size bins. For clarity, shown in Figure 7.10 are only the pre-exponents obtained for two different size bins. The results were very consistent among themselves showing a trend that closely reflects the changes in the activation energy. As expected, the pre-exponent changes in a much broader range of values than activation energy. Its change (in $\frac{g}{m \cdot s}$) can

be described as a function of the oxide thickness using a curve-fitting expression analogous to that used for the activation energy:

$$\ln\left(C_{amorph}\right) = -5.01 - \frac{1.69 \cdot 10^{7}}{h^{15.4}} \tag{7.5}$$

Similarly to Equation (7.4), Equation (7.5) can be used for the oxide thicknesses exceeding 2.5 nm.

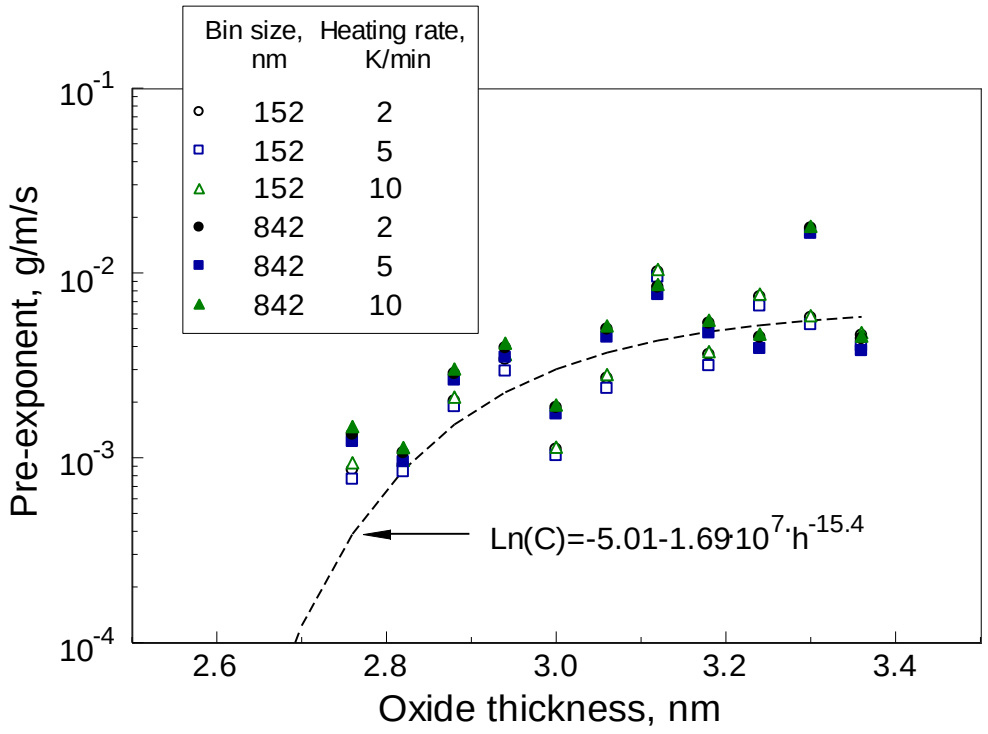

Figure 7.10 Pre-exponent characterizing growth of amorphous alumina calculated considering different particle sizes and different heating rates.

Results of isoconversion processing of the TG measurements temperatures above 770 K, describing growth of transition alumina polymorphs are illustrated in Figure 7.11.

Apparent activation energy is calculated for thicknesses above ca. 5.4 nm while the calculated values in Figure 7.9, for amorphous oxide, end around 3.5 nm. The gap between 3.5 and 5.4 nm is not described because the polymorphic phase transition was assumed to occur at a fixed temperature of 770 K. At different heating rates, different thickness of the amorphous oxide is predicted to grow by 770 K, varied from about 3.5 to 5.4 nm in present experiments. Respectively, the isoconversion processing, which uses data for all heating rates simultaneously, is limited to the data range with the same range of variation of the oxide thickness, selected as the reaction progress indicator.

The values of the apparent activation energies describing growth of γ-Al_2O_3 (Figure 7.11) obtained from processing TG data corresponding to different particle size bins are consistent with one another. The apparent activation energy increases from about 180 to approximately 230 kJ/mol as the oxide thickness grows up to ca. 12 nm. The activation energy then decreases to approximately 150 kJ/mol when oxide thickness reaches ca. 20 nm. Strong variations in the activation energy are observed at thicknesses around 22 – 24 nm, which occur in the vicinity of the aluminum melting point for the heating rates used in the TG measurements. Following the melting point, the activation energy is observed to increase, reaching very high values at the terminal thickness of about 60 nm.

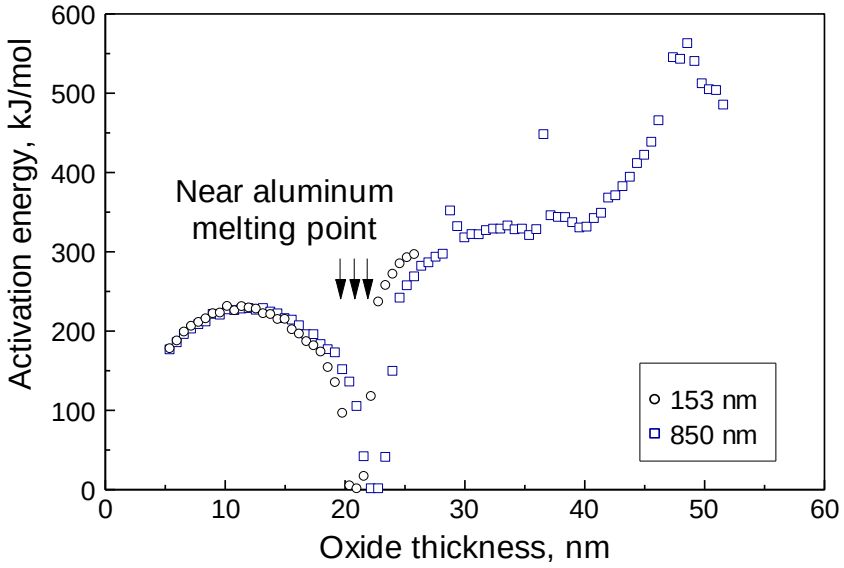

Figure 7.11 Apparent activation energy characterizing growth of transition alumina polymorphs obtained from model-free isoconversion processing of experimental data and considering different particle sizes.

Using the apparent activation energy as shown in Figure 7.11, and accounting for the specific oxidation model (Figure 7.1), the pre-exponent values characterizing growth of transition alumina can also be obtained, as shown in Figure 7.12. The pre-exponent was only calculated for oxidation up to about 20 nm, e.g., before the aluminum melting occurring in TG experiments. A rapid increase in the apparent activation energy following melting is probably associated with substantial changes in the morphology of the oxidizing sample as a result of particle agglomeration, e.g., loss in the surface area available for reaction. This increase is unlikely to characterize heterogeneous oxidation reactions of interest in this study.

For the pre-exponent, the results are somewhat different when different particle size bins and different heating rates are used. A possible reason for this discrepancy is that

in the present analysis, the polymorphic phase transition from amorphous to γ-Al_2O_3 was assumed to occur at a fixed temperature for simplicity. In reality, this transition is affected by both temperature and oxide thickness; it occurs at different temperatures for different oxide thicknesses, depending on the heating rate [94, 165, 166]. Neglecting the effect of oxide thickness would shift the starting point for the present analysis compared to the actual formation of γ-Al_2O_3. The shift would be different for different particle size bins and for different heating rates.

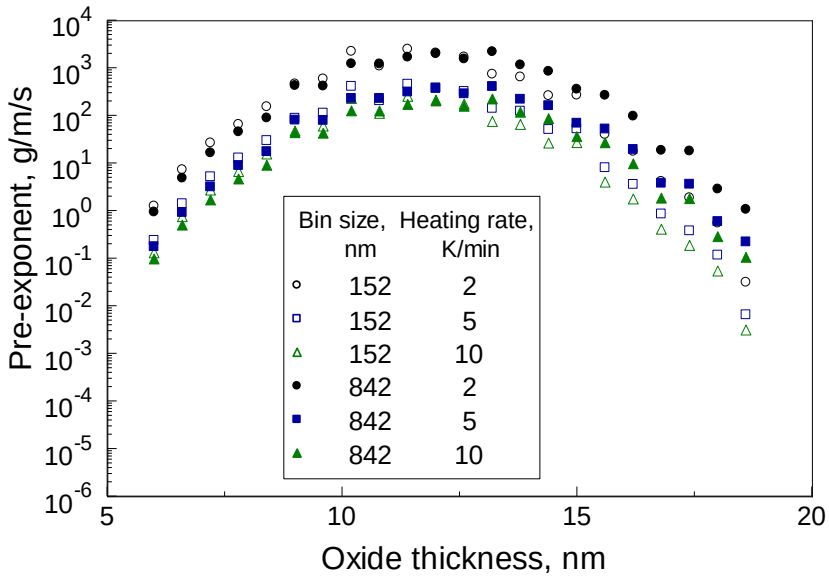

Figure 7.12 Pre-exponent characterizing growth of transition alumina calculated considering different particle sizes and different heating rates.

7.7 Discussion

In this section, results obtained here for oxidation for nano-sized aluminum powders are compared to those reported for micron-sized aluminum earlier [163]. Possible reasons for

the observed differences in the reaction kinetics for powders with different particle sizes are also discussed.

Apparent activation energy characterizing oxidation of aluminum is shown in Figure 7.13 as a function of the oxide thickness, where results for amorphous and transition alumina polymorphs shown in Figures 7.9 and 7.11 are combined with the activation energy obtained for a coarser aluminum powder [163]. The inset in Figure 7.13 shows a close-up to the range of small oxide thicknesses. Thin solid lines represent piecewise straight line fits proposed to describe the activation energy as a function of thickness in Reference [163]. It is remarkable that for both nano-sized and micron-sized powders, apparent activation energy describing growth of amorphous alumina is shown to increase substantially for very small thicknesses and at low temperatures. The straight line segments proposed to describe the activation energy as a function of the oxide layer thickness for coarse aluminum for practical applications offer a reasonable approximation for the present data. Using Equation (7.4) instead is advisable for greater accuracy of predicted oxidation rate; however, the difference between the values of activation energy is minor.

A fairly sharp increase in the apparent activation energy observed for thin amorphous alumina layers may be attributed to healing imperfections and defects present in natural alumina and described in earlier research using high-resolution TEM images [62, 95, 167].

The trend for the apparent activation energy describing growth of γ-Al_2O_3 diverges slightly from the trend implied by the current data for growth of the amorphous oxide. This small difference is not apparent from the data obtained for coarser powder in Reference

[163], where the entire range of oxide thicknesses was processed, without subdividing it into portions related to amorphous and crystalline alumina polymorphs.

Generally, there is good agreement between trends describing the apparent activation energy as a function of thickness of γ-Al_2O_3 for both nano- and micron-sized powders for the oxide thicknesses up to about 13 nm. The apparent activation energies diverge somewhat between different types of powders for greater alumina thicknesses, most likely as a result of changes in the powder morphologies, primarily, sintering between oxidizing particles.

The initial oxidation is expected to be better described using Equation (7.5) for the pre-exponent, while the piecewise straight line fits proposed in Reference [163] for coarser aluminum are also expected to predict the oxidation rate with an acceptable accuracy.

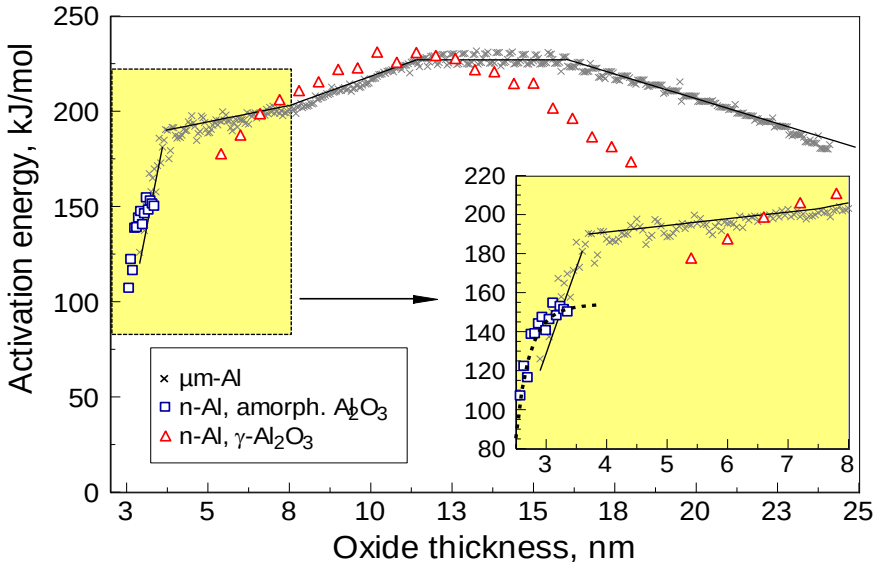

Figure 7.13 Activation energy as a function of thickness of the grown oxide layer. Results for both amorphous and transition alumina from the present measurements are combined with the activation energy obtained for micron-sized aluminum powders [163]. Thin solid lines show straight line fits proposed for the activation energy in Reference [163]. A dashed line in the inset is calculated using Equation (7.4).

Comparisons of pre-exponent values for different powders are illustrated in Figure 7.14. The inset shows a close-up to the range of small oxide thicknesses. As in Figure 7.13, thin solid lines represent piecewise straight line fits proposed to describe the pre-exponent as a function of thickness in Reference [163].

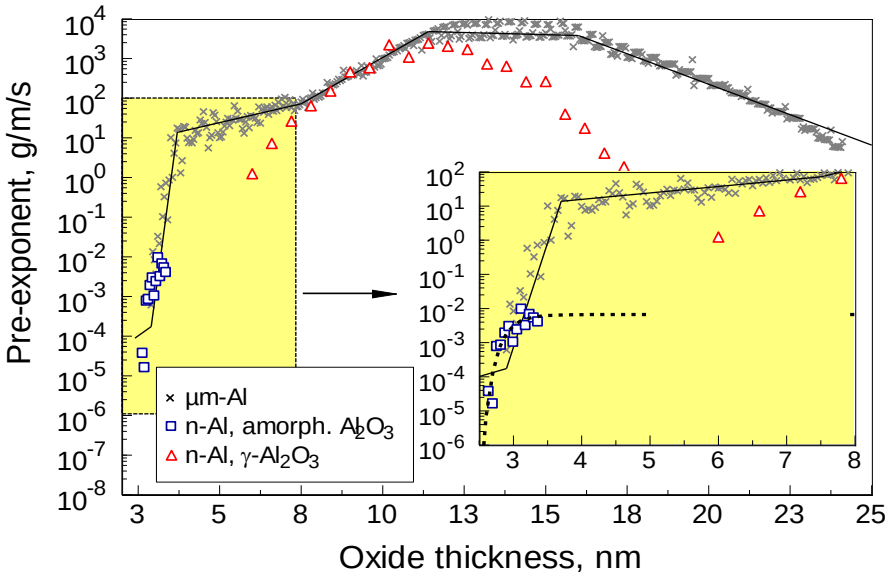

Figure 7.14 Pre-exponent as a function of thickness of the grown oxide layer. Results for both amorphous and transition aluminas from the present measurements are combined with the pre-exponent obtained for micron-sized aluminum powders [163]. Thin solid lines show straight line fits proposed for the pre-exponent in Reference [163]. A dashed line in the inset is calculated using Equation (7.5).

There are small but appreciable differences between the straight line fragments proposed to describe the pre-exponent as a function of the oxide thickness for coarse aluminum and the trends describing the pre-exponent for both amorphous and γ-Al_2O_3 based on the present measurements. The initial oxidation is expected to be better described using Equation (7.5) for the pre-exponent, using the present measurements, where the initial oxidation is resolved better. Description of growth of γ-Al_2O_3 is a bit more difficult

to quantify precisely because of an approximation used here to determine the instant of the polymorphic phase change leading to its formation.

Initial reactions starting from thin, natural oxide film are particularly important for descriptions of both ignition and aging of aluminum and related reactive materials. Therefore, oxidation kinetics identified in Reference [163] and validated here, with slightly amended expressions for activation energy and pre-exponent (Equation (7.4), (7.5)) should be used in the respective reaction models.

Aluminum ignition is most likely occurring soon after the polymorphic phase change transforming the natural amorphous alumina into a higher density γ-Al_2O_3 phase. The diffusion resistance of the oxide layer diminishes, reaction rate accelerates, causing ignition [25, 31, 90]. Predicting when the polymorphic transition between amorphous and γ-Al_2O_3 occur can thus be used to predict the ignition delay for an aluminum particle. Because the phase change depends on both temperature and the oxide thickness, calculating an increasing oxide thickness during the initial pre-ignition particle heating is important. Equations (7.4) and (7.5) obtained here as fits to the experimentally inferred apparent activation energy and respective pre-exponent can be used to perform such calculations for any aluminum particle heating scenarios. For example, to account for transitions between alumina polymorphs, the following equation was proposed in Reference [31]:

$$\frac{dh_\gamma}{dt} = F_\gamma T \left\{ 1 - e^{\left(-\frac{K_\gamma h}{RT} \right)} \right\} e^{\left(-\frac{E_\gamma}{RT} \right)} \tag{7.6}$$

where F_γ, K_γ, and E_γ are parameters describing a specific oxide polymorph. It is important that the rate of growth is affected by both temperature, as in usual thermally activated oxidation, and by the oxide thickness. Thus, to accurately predict when the rate of growth of γ-Al_2O_3 becomes significant (i.e., greater than the growth of amorphous alumina), one needs to simultaneously track both temperature and thickness of the oxide layer. Equations (7.4) and (7.5) enable one to track the thickness of the growing amorphous alumina, and thus enable one to predict when γ-Al_2O_3 will start to grow, or when the particle is expected to ignite. A main shortcoming of the present approach is an approximate nature of Equation (7.6), although it properly accounts for the effects of both temperature and oxide thickness on structure of the growing aluminum oxide.

For aging analysis, the effect of polymorphic phase change on the thickness of growing aluminum oxide layer can be neglected; thus the straight line fits proposed in Reference [163] are useful, which also describe the present results reasonably well. Conversely, fitting lines connecting trends for activation energies and pre-exponents for both amorphous and γ-Al_2O_3 using the present data can be obtained and used to predict the rate of aluminum oxidation in slow aging processes.

7.8 Conclusion

Thickness of the oxide layer growing on nano-sized aluminum powders exposed to elevated temperatures in oxygen-containing environments was obtained from both TEM images and processing of respective TG traces. The TG data processing accounted for the specific particle size distribution. The measured weight gain was split among different size bins of the powder, accounting for particle sizes and spherical shapes, and taking into

consideration that the reaction occurs at the outer interface of the growing oxide layer. The oxide layers observed in TEM images correlated well with those implied at different temperatures by the TG measurements.

Oxidation kinetics was characterized using isoconversion processing of the TG data. Separate trends for kinetic activation energies and pre-exponents as a function of the oxide thickness were obtained to describe growth of amorphous and γ-Al_2O_3 polymorphs. The present results are in good agreement with the earlier studies characterizing kinetics of oxidation of coarser aluminum powders. The present results confirm that the mechanism of aluminum oxidation does not change as a function of particle size down to tens of nm.

An increase in the apparent activation energy describing growth of amorphous alumina implied by earlier work is confirmed here. The higher activation energy is likely associated with an increasing homogeneity in the growing amorphous oxide layer, initially containing multiple defects and imperfections. The trends obtained here and describing changes in both activation energy and pre-exponent of the growing amorphous oxide are useful for prediction of ignition delays of aluminum particles. The ignition is expected to occur when γ-Al_2O_3 forms disrupting continuity of the oxide layer covering aluminum surface. Formation of γ-Al_2O_3 is affected by both temperature and thickness of the oxide layer. The thickness of the oxide grown during pre-ignition processes can be predicted using the kinetics of growth of amorphous alumina obtained here. The kinetic trends describing activation energies and pre-exponents in a broader range of the oxide thicknesses are useful for prediction of aging behavior of aluminum powders.

CHAPTER 8

CONCLUSION AND FUTURE WORK

8.1 Conclusion

Reaction of aluminum with liquid water characterized by microcalorimetry includes several parts: induction time, two stages of relatively rapid reaction, and termination. The only reaction product formed at 303 and 313 K is bayerite. The significance of the first of the two rapid reaction stages increased in experiments at 313 K. Generally, finer powders were observed to react faster and to a greater completion. Effects of powder load and mass of water are found to be negligible. Reaction characteristics were poorly reproducible despite well maintained reaction temperatures. It is hypothesized that minor differences in powder packing and trapped gases could substantially affect reaction rates for the processes occurring directly on the particle surfaces, as expected for the alumina hydration occurring during the induction period. Processing the present experimental data using a simplified kinetic model available in the literature showed that the calculated diffusion coefficient for the rate-limiting process is affected by the reaction temperature, particle sizes, and reaction time. While the first effect is expected, the observed effects of particle size and reaction time likely indicate that the model is inadequate for describing the present experiments. Porosity of the growing bayerite, defining the rate of diffusion and thus the reaction rate, changes as a function of the reaction completeness. It is also affected by experimental conditions, including reaction temperature and powder particle size distribution.

Location of the reaction interface for aluminum with water is identified for both liquid water and steam. For liquid water, processing flow calorimetry data for two spherical aluminum powders with different but overlapping particle size distributions suggests that the reaction occurs at the surface of the shrinking aluminum core, inside the growing aluminum hydroxide layer. For reaction of aluminum with steam at elevated temperatures, the results are less conclusive, but indicate that the reaction is most likely occurring at the outer surface of the growing alumina shell. The results also indicate that the growing alumina shell is rigid and fractures multiple times during growth. After a shell is fractured, a new shell begins to grow around the oxidizing aluminum core. The current results are best explained when it is assumed that the alumina shells fracture when they become thicker than 0.5 μm; however, the detailed fracturing mechanism will depends on particle size and temperature.

Thermo-gravimetric measurements with large amounts of fine aluminum powders are useful in obtaining detailed information on their oxidation kinetics at low temperatures. However, restricted access of oxidizer to the powder for increased powder load can also cause misleading TG measurements, during which different portions of the sample react with different rates. Constant heating rate measurements were most useful in establishing reaction kinetics for aluminum powders at low temperatures and reduced oxide thickness. The activation energy as a function of reaction progress was obtained using a model-free isoconversion processing of experimental data. Once the activation energy was obtained, an explicit oxidation model assuming reaction occurring at the outside of a rigid spherical layer was considered to determine the pre-exponent as a function of the reaction progress. Therefore, both activation energy and pre-exponent were obtained as functions of the

reaction progress expressed, for convenience, through the oxide layer thickness. The oxidation model was compared with the present and previously reported data on oxidation of fine aluminum powders; the match between experiments and calculations is satisfactory. For nano-powders, agglomeration is accounted for, and the results illustrate that this is essential for accurate calculation of oxidation rate. The oxidation model was combined with description of heat transfer for an aluminum particle exposed to a heated oxidizing environment. Thus, a model describing particle ignition was obtained and compared to earlier predictions and recent experiments. The model predicts a sharp rise in the ignition temperature from 850 to 2260 K for particles with sizes increasing respectively from 0.3 to 1.2 μm. The specific results are affected by the assumed initial oxide thickness (2.5 nm) and thermal accommodation coefficient (taken as 1). The experiments show an increase in the ignition temperature; however, this increase may be more gradual than predicted in the model. The discrepancy between predictions and measurements is most likely due to a relatively broad particle size distribution for the powders used in experiments and a difficulty to identify which size sub-range of the heated particles ignites at the threshold temperature.

Reactions of heterogeneous magnesium oxidation occurring in a broad range of temperatures in both dry and wet environments producing either MgO or Mg(OH)2 take place at the interface between magnesium metal and the growing oxidized product layer. This suggests that the reactions are rate limited by diffusion of oxidizer through the growing magnesium oxide or magnesium hydroxide layers. All oxidation reactions for magnesium powders can be described reasonably well using a model assuming that the reaction is limited by thermally activated diffusion of oxidizer through a growing shell of

the product. Activation energy of magnesium oxidation in humid environments at low temperatures is close to 60 kJ/mol. The pre-exponent varies in a range of 10-3-10-2g/m/s, depending on a specific environment and humidity. The identified low-temperature reaction kinetics enables one to describe aging of Mg powders stored at different temperatures and humidities.

Reaction kinetics at elevated temperatures, which is relevant for modeling ignition of magnesium and its alloys, is also quantified. Activation energy for oxidation of magnesium in oxygen is 148 kJ/mol. To adequately describe the observed reaction, the pre-exponent should increase as a function of the growing oxide layer, reaching ca. 350 g/m/s for 1-μm thick oxide. For oxidation of magnesium in steam at elevated temperatures, the activation energy increases linearly from approximately 130 to 360 kJ/mol, while the forming oxide layer thickens up to 2.4 μm. The pre-exponent, C, increases simultaneously with the activation energy; $ln(C)$ in g/m/s reaches 16.2 when the oxide thickness reaches 2.4 μm.

The oxidation of both commercial spherical Al-Mg alloys and mechanically alloyed Al-Mg powder in oxygen was investigated using thermo-gravimetry. Two oxidation stages were observed for both powders. First, selective oxidation of magnesium resulting in formation of an MgO shell is observed. The second step reaction generates spinel, $MgAl_2O_4$. Both reactions occur at the interface between the metal alloy core and the oxide shell and thus are rate-limited by inward diffusion of oxygen ions. Voids are formed in the oxidized particles due to the re-distribution of material within the metal core. The switch over between reaction steps occurs when the oxide shell grows above a certain thickness between 1.2 and 1.5 μm. The apparent activation energy of selective oxidation

of Mg falls rapidly from 250 to 130 kJ/mol when the oxide thickness increases to ca. 0.24 μm. The activation energy continues to diminish down to approximately 65 kJ/mol as the oxide continues to thicken to 1.2 μm. For the second oxidation step, the activation energy remains nearly constant around 180 kJ/mol while the oxide shell grows up to approximately 3 μm. At greater oxide thicknesses, a slow decrease in the apparent activation energy is observed.

Thickness of the oxide layer growing on nano-sized aluminum powders exposed to elevated temperatures in oxygen-containing environments was obtained from both TEM images and processing of respective TG traces. The TG data processing accounted for the specific particle size distribution. The measured weight gain was split among different size bins of the powder, accounting for particle sizes and spherical shapes, and taking into consideration that the reaction occurs at the outer interface of the growing oxide layer. The oxide layers observed in TEM images correlated well with those implied at different temperatures by the TG measurements.

Oxidation kinetics was characterized using isoconversion processing of the TG data. Separate trends for kinetic activation energies and pre-exponents as a function of the oxide thickness were obtained to describe growth of amorphous and γ-Al_2O_3 polymorphs. The present results are in good agreement with the earlier studies characterizing kinetics of oxidation of coarser aluminum powders. The present results confirm that the mechanism of aluminum oxidation does not change as a function of particle size down to tens of nm.

An increase in the apparent activation energy describing growth of amorphous alumina implied by earlier work is confirmed here. The higher activation energy is likely associated with an increasing homogeneity in the growing amorphous oxide layer, initially

containing multiple defects and imperfections. The trends obtained here and describing changes in both activation energy and pre-exponent of the growing amorphous oxide are useful for prediction of ignition delays of aluminum particles. The ignition is expected to occur when γ-Al_2O_3 forms disrupting continuity of the oxide layer covering aluminum surface. Formation of γ-Al_2O_3 is affected by both temperature and thickness of the oxide layer. The thickness of the oxide grown during pre-ignition processes can be predicted using the kinetics of growth of amorphous alumina obtained here. The kinetic trends describing activation energies and pre-exponents in a broader range of the oxide thicknesses are useful for prediction of aging behavior of aluminum powders.

8.2 Future Work

Reactions of aluminum and magnesium in oxygen, steam and liquid water are quantitatively described using thermal-analytical technique. Respective oxidation model is developed accounting for particle size distributions and reaction interfaces identified differently for various oxidizing environments. The ignition model was modified using an updated reaction kinetics describing the growth of amorphous alumina layers of aluminum particles in micro-size scale. In the future work, ignition model for magnesium powder can be developed applying the reaction kinetics of magnesium in oxygen obtained at high temperatures. For aluminum-magnesium alloys powder, different oxidizers are also of interest to be investigated; for example reaction mechanisms and kinetics of such alloys with steam and liquid water can be developed. Most importantly, the approach developed in the present dissertation, enables one to interpret thermo-analytical measurements for spherical powders of any materials first identifying the location of interface of

heterogeneous reaction and then describing its kinetics while accounting explicitly for the effect of particle size distributions. Ignition and aging of many metal powders, such as Ti, Zr, Ni, and others, oxidizing heterogeneously can be readily characterized. Furthermore, the approach can be expanded to characterize reactions in porous materials, such as carbon.

REFERENCES

[1] E.W. Price, Combustion of aluminum in solid propellant flames, AGARD Conference Proceedings (1979) 14. 11-14. 15.

[2] M.W. Beckstead, Correlating aluminum burning times, Combustion, Explosion and Shock Waves 41 (2005) 533-546.

[3] E.I. Gusachenko, L.N. Stesik, V.P. Fursov, V.I. Shevtsov, Condensed products of combustion of magnesium powders. II. Dependence on the particle size, Fizika Goreniya Vzryva 10 (1974) 669-676.

[4] V.I. Shevtsov, V.P. Fursov, L.N. Stesik, Combustion mechanism of single magnesium particles, Fizika Goreniya Vzryva 12 (1976) 859-856.

[5] E.Y. Shafirovich, U.I. Goldshleger, The superheat phenomenon in the combustion of magnesium particles, Combustion and Flame 88 (1992) 425-432.

[6] E.L. Dreizin, V.K. Hoffmann, Experiments on magnesium aerosol combustion in microgravity, Combustion and Flame 122 (2000) 20-29.

[7] N.I. Poletaev, Electrical oscillations in combustion of magnesium particles in a constant electric field, Combustion, Explosion and Shock Waves 48 (2012) 151-162.

[8] V.G. Poyarkov, Combustibility of aluminum-magnesium powdered alloys, Izvestiya Vysshikh Uchebnykh Zavedenii, 10 (1967) 149-153.

[9] A.L. Breiter, L.Y. Kashporov, V.M. Mal'tsev, P.F. Pokhil, E.I. Popov, V.I. Pepekin, A.G. Stasenko, Combustion of single particles of aluminum-magnesium alloys in the flame of an oxidizing agent-fuel mixture, Fizika Goreniya Vzryva 7 (1971) 222-227.

[10] E.I. Popov, L.Y. Kashporov, V.M. Mal'tsev, A.L. Breiter, Mechanism of combustion of aluminum-magnesium alloy particles, Fizika Goreniya Vzryva 9 (1973) 240-246.

[11] S. Yuasa, T. Takeno, Ignition and combustion of magnesium-aluminum alloy particle clouds in a hot gas stream, Symposium (International) on Combustion, [Proceeding] 19th (1982) 741-748.

[12] T.A. Roberts, R.L. Burton, H. Krier, Ignition and combustion of aluminum/magnesium alloy particles in oxygen at high pressures, Combustion and Flame 92 (1993) 125-143.

[13] D.G. Keil, E.D. Dreizin, H.F. Calcote, W. Felder, V.K. Hoffman, Magnesium coating effects in boron combustion, Chemical Physics of Pyrolysis, Combustion and Oxidation (1995) 329-332.

[14] J.Z. Liu, J.F. Xi, W.J. Yang, Y.R. Hu, Y.W. Zhang, Y. Wang, J.H. Zhou, Effect of magnesium on the burning characteristics of boron particles, Acta Astronautica 96 (2014) 89-96.

[15] M.A. Machado, D.A. Rodriguez, Y. Aly, M. Schoenitz, E.L. Dreizin, E. Shafirovich, Nanocomposite and mechanically alloyed reactive materials as energetic additives in chemical oxygen generators, Combustion and Flame 161 (2014) 2708-2716.

[16] D.A. Rodriguez, E.L. Dreizin, E. Shafirovich, Hydrogen generation from ammonia borane and water through combustion reactions with mechanically alloyed Al·Mg powder, Combustion and Flame 162 (2015) 1498-1506.

[17] A. Corcoran, S. Mercati, H. Nie, M. Milani, L. Montorsi, E.L. Dreizin, Combustion of fine aluminum and magnesium powders in water, Combustion and Flame 160 (2013) 2242-2250.

[18] A.C.D. Chaklader, T. Troczynski, V. Bapooji, V. Chaskar, Hydrogen generation through aluminum-assisted water split reaction, Canadian Institute of Mining, Metallurgy and Petroleum, 2003, pp. 201-206.

[19] G. Ma, D. Zhuang, H. Dai, P. Wang, Controlled hydrogen generation by reaction of aluminum with water, Progress in Chemistry 24 (2012) 650-658.

[20] M.S. Vlaskin, E.I. Shkolnikov, A.V. Bersh, A.Z. Zhuk, A.V. Lisicyn, A.I. Sorokovikov, Y.V. Pankina, An experimental aluminum-fueled power plant, Journal of Power Sources 196 (2011) 8828-8835.

[21] F. Franzoni, M. Milani, L. Montorsi, V. Golovitchev, Combined hydrogen production and power generation from aluminum combustion with water: Analysis of the concept, International Journal of Hydrogen Energy 35 (2010) 1548-1559.

[22] F. Franzoni, S. Mercati, M. Milani, L. Montorsi, Operating maps of a combined hydrogen production and power generation system based on aluminum combustion with water, International Journal of Hydrogen Energy 36 (2011) 2803-2816.

[23] S. Mercati, M. Milani, L. Montorsi, F. Paltrinieri, Design of the steam generator in an energy conversion system based on the aluminum combustion with water, Applied Energy 97 (2012) 686-694.

[24] D.F. Waters, C.P. Cadou, W.E. Eagle, Quantifying unmanned undersea vehicle range improvement enabled by aluminum-water power system, Journal of Propulsion and Power 29 (2013) 675-685.

[25] M.A. Trunov, M. Schoenitz, X. Zhu, E.L. Dreizin, Effect of polymorphic phase transformations in Al2O3 film on oxidation kinetics of aluminum powders, Combustion and Flame 140 (2005) 310-318.

[26] M.A. Trunov, S.M. Umbrajkar, M. Schoenitz, J.T. Mang, E.L. Dreizin, Oxidation and melting of aluminum nanopowders, Journal of Physical Chemistry B 110 (2006) 13094-13099.

[27] M. Schoenitz, M.A. Trunov, C.M. Chen, E.L. Dreizin, Experimental investigation of aluminum oxidation in water, AIChE Meeting, Salt Lake City, UT, 2007.

[28] M. Schoenitz, S. Mohan, C.M. Chen, E.L. Dreizin, Oxidation and ignition of aluminum particles in the presence of water vapor, AIAA Conference, Hartford, CT, 2008.

[29] M. Schoenitz, C.M. Chen, E.L. Dreizin, Oxidation of aluminum particles in the presence of water, Journal of Physical Chemistry B 113 (2009) 5136-5140.

[30] M. Schoenitz, B. Patel, O. Agboh, E.L. Dreizin, Oxidation of aluminum powders at high heating rates, AIAA Conference, Denver, CO, 2009.

[31] M.A. Trunov, M. Schoenitz, E.L. Dreizin, Effect of polymorphic phase transformations in alumina layer on ignition of aluminium particles, Combustion Theory and Modelling 10 (2006) 603-623.

[32] J. Callaway, N. Davies, Ageing of magnesium coated with viton, Proceedings of the International Pyrotechnics Seminar 35th (2008) 39-56.

[33] S.M. Pourmortazavi, S. Babaee, Z. Marashianpour, I. Kohsari, Stabilizing of magnesium powder by microencapsulation with azidodeoxy cellulose nitrate, Progress in Organic Coating 81 (2015) 107-115.

[34] S.U. Bayca, M.F. Cansizoglu, A.S. Biris, F. Watanabe, T. Karabacak, Enhanced oxidation resistance of magnesium nanorods grown by glancing angle deposition, International Journal of Hydrogen Energy 36 (2011) 5998-6004.

[35] D.L. Zhang, T.B. Massalski, M.R. Paruchuri, Formation of metastable and equilibrium phases during mechanical alloying of Al and Mg powders, Metallurgical and Materials Transactions A: Physical Metallurgy and Materials Science 25 A (1994) 73-79.

[36] Y. Aly, M. Schoenitz, E.L. Dreizin, Ignition and combustion of mechanically alloyed Al-Mg powders with customized particle sizes, Combustion and Flame 160 (2013) 835-842.

[37] S.M. Umbrajkar, M. Schoenitz, S.R. Jones, E.L. Dreizin, Effect of temperature on synthesis and properties of aluminum-magnesium mechanical alloys, Journal of Alloys and Compounds 402 (2005) 70-77.

[38] S. Umbrajkar, M.A. Trunov, M. Schoenitz, E.L. Dreizin, R. Broad, Arrested reactive milling synthesis and characterization of sodium-nitrate based reactive composites, Propellants, Explosives, Pyrotechnics 32 (2007) 32-41.

[39] J. Medved, P. Mrvar, High-temperature oxidation of Mg alloys, Livarski Vestn. 53 (2006) 98-111.

[40] J. Medved, P. Mrvar, M. Voncina, Oxidation resistance of AM60, AMS0, AE42 and AZ91 magnesium alloys, InTech, 2011, pp. 15-28.

[41] M. Schoenitz, E.L. Dreizin, Structure and properties of Al-Mg mechanical alloys, Journal of Materials Research 18 (2003) 1827-1836.

[42] G.W. Crabtree, M.S. Dresselhaus, M.V. Buchanan, The hydrogen economy, Physics Today 57 (2004) 39-44.

[43] L. Barreto, A. Makihira, K. Riahi, The hydrogen economy in the 21st century: A sustainable development scenario, International Journal of Hydrogen Energy 28 (2003) 267-284.

[44] S. Dunn, Hydrogen futures: Toward a sustainable energy system, International Journal of Hydrogen Energy 27 (2002) 235-264.

[45] R. Dufo-López, J.L. Bernal-Agustín, J. Contreras, Optimization of control strategies for stand-alone renewable energy systems with hydrogen storage, Renewable Energy 32 (2007) 1102-1126.

[46] W. El-Khattam, M.M.A. Salama, Distributed generation technologies, definitions and benefits, Electric Power Systems Research 71 (2004) 119-128.

[47] G.A. Richards, M.M. McMillian, R.S. Gemmen, W.A. Rogers, S.R. Cully, Issues for low-emission, fuel-flexible power systems, Progress in Energy and Combustion Science 27 (2001) 141-169.

[48] W. Wang, X.M. Zhao, D.M. Chen, K. Yang, Insight into the reactivity of Al-Ga-In-Sn alloy with water, International Journal of Hydrogen Energy 37 (2012) 2187-2194.

[49] H.W. Wang, H.W. Chung, H.T. Teng, G. Cao, Generation of hydrogen from aluminum and water - Effect of metal oxide nanocrystals and water quality, International Journal of Hydrogen Energy 36 (2011) 15136-15144.

[50] Z.Y. Deng, Y.B. Tang, L.L. Zhu, Y. Sakka, J. Ye, Effect of different modification agents on hydrogen-generation by the reaction of Al with water, International Journal of Hydrogen Energy 35 (2010) 9561-9568.

[51] E. Czech, T. Troczynski, Hydrogen generation through massive corrosion of deformed aluminum in water, International Journal of Hydrogen Energy 35 (2010) 1029-1037.

[52] C.E. Bunker, M.J. Smith, K.A. Shiral Fernando, B.A. Harruff, W.K. Lewis, J.R. Gord, E.A. Guliants, D.K. Phelps, Spontaneous hydrogen generation from organic-capped al nanoparticles and water, ACS Applied Materials and Interfaces 2 (2010) 11-14.

[53] Z.Y. Deng, J.M.F. Ferreira, Y. Sakka, Hydrogen-generation materials for portable applications, Journal of the American Ceramic Society 91 (2008) 3825-3834.

[54] O.V. Kravchenko, K.N. Semenenko, B.M. Bulychev, K.B. Kalmykov, Activation of aluminum metal and its reaction with water, Journal of Alloys and Compounds 397 (2005) 58-62.

[55] J.T. Ziebarth, J.M. Woodall, R.A. Kramer, G. Choi, Liquid phase-enabled reaction of Al-Ga and Al-Ga-In-Sn alloys with water, International Journal of Hydrogen Energy 36 (2011) 5271-5279.

[56] P. Dupiano, D. Stamatis, E.L. Dreizin, Hydrogen production by reacting water with mechanically milled composite aluminum-metal oxide powders, International Journal of Hydrogen Energy 36 (2011) 4781-4791.

[57] W.Z. Gai, Z.Y. Deng, Y.B. Zhang, Y. Sakka, J. Ye, Z.W. Ou, Dynamics difference between the reactions of γ-Al2o 3 modified al powder and pure Al powder with water, Journal of New Materials for Electrochemical Systems 13 (2010) 345-348.

[58] Z.Y. Deng, L.L. Zhu, Y.B. Tang, Y. Sakka, J. Ye, R.J. Xie, Role of particle sizes in hydrogen generation by the reaction of Al with water, Journal of the American Ceramic Society 93 (2010) 2998-3001.

[59] Z.Y. Deng, J.M.F. Ferreira, Y. Tanaka, J. Ye, Physicochemical mechanism for the continuous reaction of γ-Al 2O3-modified aluminum powder with water, Journal of the American Ceramic Society 90 (2007) 1521-1526.

[60] R.A. Robie, B.S. Hemingway, Thermodynamic properties of minerals and related substances at 298.15 K and 1 bar (105 Pascals) pressure and at higher temperatures, US Geological Survey Bulletin 2131 (1995).

[61] A. J.A., N. J.M., J. C.-H., Thermochemical properties of gibbsite, bayerite, boehmite, diaspore, and the aluminate ion between 0 and 350 °C., University of California Lawrence Berkeley Report, 1988.

[62] V.Y. Gertsman, Q.S.M. Kwok, TEM investigation of nanophase aluminum powder, Microscopy and Microanalysis 11 (2005) 410-420.

[63] A. Violante, P.M. Huang, Formation mechanism of aluminum hydroxide polymorphs, Clays & Clay Minerals 41 (1993) 590-597.

[64] W. Mišta, J. Wrzyszcz, Rehydration of transition aluminas obtained by flash calcination of gibbsite, Thermochimica Acta 331 (1999) 67-72.

[65] A.I. Rat'ko, V.E. Romanenkov, E.V. Bolotnikova, Z.V. Krupen'kina, Hydrothermal Synthesis of Porous Al2O3/Al Metal Ceramics: II. Mechanism of Formation of a Porous Al(OH)3/Al Composite, Kinetics and Catalysis 45 (2004) 149-155.

[66] H.Z. Wang, D.Y.C. Leung, M.K.H. Leung, M. Ni, A review on hydrogen production using aluminum and aluminum alloys, Renewable and Sustainable Energy Reviews 13 (2009) 845-853.

[67] X. Huang, T. Gao, X. Pan, D. Wei, C. Lv, L. Qin, Y. Huang, A review: Feasibility of hydrogen generation from the reaction between aluminum and water for fuel cell applications, Journal of Power Sources 229 (2013) 133-140.

[68] E.I. Shkolnikov, A.Z. Zhuk, M.S. Vlaskin, Aluminum as energy carrier: Feasibility analysis and current technologies overview, Renewable and Sustainable Energy Reviews 15 (2011) 4611-4623.

[69] J. Foote, B. Thompson, J. Lineberry, Combustion of Aluminum with Steam for Underwater Propulsion, Advances in Chemical Propulsion, CRC Press 2001.

[70] D.F. Waters, C.P. Cadou, Modeling a hybrid Rankine-cycle/fuel-cell underwater propulsion system based on aluminum-water combustion, Journal of Power Sources 221 (2013) 272-283.

[71] A.I. Rat'ko, T.F. Kuznetsova, V.E. Romanenkov, D.I. Klevchenya, Kinetics of bayerite microstructure formation from powdered aluminum, Colloid Journal 70 (2008) 210-214.

[72] A.A. Vostrikov, O.N. Fedyaeva, Mechanism and kinetics of Al2O3 nanoparticles formation by reaction of bulk Al with H2O and CO2 at sub- and supercritical conditions, Journal of Supercritical Fluids 55 (2010) 307-315.

[73] Z.-Y. Deng, Y.-B. Tang, L.-L. Zhu, Y. Sakka, J. Ye, Effect of different modification agents on hydrogen-generation by the reaction of Al with water, International Journal of Hydrogen Energy 35 (2010) 9561-9568.

[74] J.T. Ziebarth, J.M. Woodall, R.A. Kramer, G. Choi, Liquid phase-enabled reaction of Al–Ga and Al–Ga–In–Sn alloys with water, International Journal of Hydrogen Energy 36 (2011) 5271-5279.

[75] D.Z. Gai WZ, Zhang YB, Sakka Y, Ye J, Ou ZW, Dynamics difference between the reactions of γ-Al2O3 modified al powder and pure Al powder with water, Journal of New Materials for Electrochemical Systems (2010) 13:345-348.

[76] Z.-Y. Deng, L.-L. Zhu, Y.-B. Tang, Y. Sakka, J. Ye, R.-J. Xie, Role of particle sizes in hydrogen generation by the reaction of Al with water, Journal of the American Ceramic Society 93 (2010) 2998-3001.

[77] Z.-Y. Deng, J.M.F. Ferreira, Y. Sakka, Hydrogen-generation materials for portable applications, Journal of the American Ceramic Society 91 (2008) 3825-3834.

[78] Z.-Y. Deng, J.M.F. Ferreira, Y. Tanaka, J. Ye, Physicochemical mechanism for the continuous reaction of γ-Al2O3-modified aluminum powder with water, Journal of the American Ceramic Society 90 (2007) 1521-1526.

[79] J.P.a.G. Thomas, Reaction of aluminum with water to produce hydrogen, Consultants to the DOE Hydrogen Program Version 1.0 - 2008 Page 2003 of 2026.

[80] H. Nie, M. Schoenitz, E.L. Dreizin, Calorimetric investigation of the aluminum-water reaction, International Journal of Hydrogen Energy 37 (2012) 11035-11045.

[81] H. Dong, S. Zhumei, Study of the fast reaction characteristics of aluminized PETN explosive powders, Combustion and Flame 105 (1996) 428-430.

[82] M.K. King, Aluminum combustion in a solid rocket motor environment, Proceedings of the Combustion Institute 32 II (2009) 2107-2114.

[83] S.H. Ba, Q.J. Jiao, H. Ren, Effect of particle sizes of aluminum powder on radiation intensity of flash pyrotechnic composites, Hanneng Cailiao/Chinese Journal of Energetic Materials 16 (2008) 219-221.

[84] E.W. Price, Combustion of metallized propellants, AIAA Conference, New York, 1984.

[85] S.R. Chakravarthy, J.M. Freeman, E.W. Price, R.K. Sigman, Combustion of propellants with ammonium dinitramide, Propellants, Explosives, Pyrotechnics 29 (2004) 220-230.

[86] M.A. Trunov, M. Schoenitz, E.L. Dreizin, Ignition of aluminum powders under different experimental conditions, Propellants, Explosives, Pyrotechnics 30 (2005) 36-43.

[87] N. Eisenreich, H. Fietzek, M. Del Mar Juez-Lorenzo, V. Kolarik, A. Koleczko, V. Weiser, On the mechanism of low temperature oxidation for aluminum particles down to the nano-scale, Propellants, Explosives, Pyrotechnics 29 (2004) 137-145.

[88] K. Park, D. Lee, A. Rai, D. Mukherjee, M.R. Zachariah, Size-resolved kinetic measurements of aluminum nanoparticle oxidation with single particle mass spectrometry, Journal of Physical Chemistry B 109 (2005) 7290-7299.

[89] X. Zhu, M. Schoenitz, E.L. Dreizin, Aluminum powder oxidation in CO2 and mixed CO2/O 2 environments, Journal of Physical Chemistry C 113 (2009) 6768-6773.

[90] M. Schoenitz, B. Patel, O. Agboh, E.L. Dreizin, Oxidation of aluminum powders at high heating rates, Thermochimica Acta 507-508 (2010) 115-122.

[91] S. Zhang, E.L. Dreizin, Reaction interface for heterogeneous oxidation of aluminum powders, The Journal of Physical Chemistry C 117 (2013) 14025-14031.

[92] S. Zhang, E.L. Dreizin, Reaction interface for heterogeneous oxidation of aluminum powders, Journal of Physical Chemistry C 117 (2013) 14025-14031.

[93] M.T.A. Saif, S. Zhang, A. Haque, K.J. Hsia, Effect of native Al2O3 on the elastic response of nanoscale Al films, Acta Materialia 50 (2002) 2779-2786.

[94] L.P.H. Jeurgens, W.G. Sloof, F.D. Tichelaar, E.J. Mittemeijer, Structure and morphology of aluminium-oxide films formed by thermal oxidation of aluminium, Thin Solid Films 418 (2002) 89-101.

[95] A.L. Ramaswamy, P. Kaste, A "Nanovision" of the physiochemical phenomena occurring in nanoparticles of aluminum, Journal of Energetic Materials 23 (2005) 1-25.

[96] S. Vyazovkin, A.K. Burnham, J.M. Criado, L.A. Pérez-Maqueda, C. Popescu, N. Sbirrazzuoli, ICTAC Kinetics Committee recommendations for performing kinetic computations on thermal analysis data, Thermochimica Acta 520 (2011) 1-19.

[97] S. Vyazovkin, Modification of the integral isoconversional method to account for variation in the activation energy, Journal of Computational Chemistry 22 (2001) 178-183.

[98] C.E. Aumann, G.L. Skofronick, J.A. Martin, Oxidation behavior of aluminum nanopowders, Journal of Vacuum Science & Technology B 13 (1995) 1178-1183.

[99] M.A. Trunov, S.M. Umbrajkar, M. Schoenitz, J.T. Mang, E.L. Dreizin, Oxidation and melting of aluminum nanopowders, The Journal of Physical Chemistry B 110 (2006) 13094-13099.

[100] C. Kong, Q. Yao, D. Yu, S. Li, Combustion characteristics of well-dispersed aluminum nanoparticle streams in post flame environment, Proceedings of the Combustion Institute 35 (2015) 2479-2486.

[101] L. Chen, W. Song, J. Lv, X. Chen, C. Xie, Research on the methods to determine metallic aluminum content in aluminum nanoparticles, Materials Chemistry and Physics 120 (2010) 670-675.

[102] M.V. Coulet, B. Rufino, P.H. Esposito, T. Neisius, O. Isnard, R. Denoyel, Oxidation mechanism of aluminum nanopowders, Journal of Physical Chemistry C 119 (2015) 25063-25070.

[103] W. Yao, G. Guangsheng, W. Fei, W. Jun, Fluidization and agglomerate structure of SiO2 nanoparticles, Powder Technology 124 (2002) 152-159.

[104] I. Danilenko, T. Konstantinova, N. Pilipenko, G. Volkova, V. Glasunova, Estimation of agglomeration degree and nanoparticles shape of zirconia nanopowders, Particle & Particle Systems Characterization 28 (2011) 13-18.

[105] D. To, R. Dave, X. Yin, S. Sundaresan, Deagglomeration of nanoparticle aggregates via rapid expansion of supercritical or high-pressure suspensions, AIChE Journal 55 (2009) 2807-2826.

[106] X. Liu, Q. Zhang, Influence of turbulent flow on the explosion parameters of micro- and nano-aluminum powder-air mixtures, J. Hazardous Materials 299 (2015) 603-617.

[107] H. Wang, M.R. Zachariah, L. Xie, G. Rao, Ignition and combustion characterization of nano-Al-AP and nano-Al-CuO-AP micro-sized composites produced by electrospray technique, Energy Procedia, 2015, pp. 109-112.

[108] M. Staiger, P. Bowen, J. Ketterer, J. Bohonek, Particle size distribution measurement and assessment of agglomeration of commercial nanosized ceramic particles, Journal of Dispersion Science and Technology 23 (2002) 619-630.

[109] S. Mohan, M.A. Trunov, E.L. Dreizin, Heating and ignition of metal particles in the transition heat transfer regime, Journal of Heat Transfer 130 (2008).

[110] F. Liu, K.J. Daun, D.R. Snelling, G.J. Smallwood, Heat conduction from a spherical nano-particle: status of modeling heat conduction in laser-induced incandescence, Journal of Applied Physics B 83 (2006) 355-382.

[111] T. Bazyn, P. Lynch, H. Krier, N. Glumac, Combustion measurements of fuel-rich aluminum and molybdenum oxide nanocomposite mixtures, Propellants Explosives Pyrotechnics (2010).

[112] D. Allen, H. Krier, N. Glumac, Heat transfer effects in nano-aluminum combustion at high temperatures, Combustion and Flame 161 (2014) 295-302.

[113] I.S. Altman, D. Lee, J. Song, M. Choi, Experimental estimate of energy accommodation coefficient at high temperatures, Physical Review E - Statistical, Nonlinear, and Soft Matter Physics 64 (2001) 052202/052201-052202/052204.

[114] J.J. Sabatini, A.V. Nagori, E.A. Latalladi, J.C. Poret, G. Chen, R. Damavarapu, T.M. Klapotke, Applications of high-nitrogen energetics in pyrotechnics: development of perchlorate-free red star M126A1 hand-held signal formulations with superior luminous intensities and burn times, Propellants, Explosives, Pyrotechnics 36 (2011) 373-378.

[115] L. Fan, G.-p. Pan, D.-h. Ouyang, X. Chen, G.-f. Pang, Application of genetic algorithm-support vector machine in formula optimization of

magnesium/polytetrafluoroethylene fuel rich propellant, Tuijin Jishu 33 (2012) 620-624.

[116] B.B. Dally, Z.T. Alwahabi, L.V. Krishnamoorthy, L.D. Redman, F.C. Christo, Measurements of particles evolution in the near combustion field of MTV formulation using Mie scattering technique, Proceedings of the International Pyrotechnics Seminar 28th (2001) 219-226.

[117] V. Fournier, P. Marcus, I. Olefjord, Oxidation of magnesium, Surface and Interface Analysis 34 (2002) 494-497.

[118] C. Fotea, J. Callaway, M.R. Alexander, Characterisation of the surface chemistry of magnesium exposed to the ambient atmosphere, Surface and Interface Analysis 38 (2006) 1363-1371.

[119] R.I. Razouk, R.S. Mikhail, The hydration of magnesium oxide from the vapor phase, Journal of Physical Chemistry 62 (1958) 920-925.

[120] Y. Kato, N. Yamashita, K. Kobayashi, Y. Yoshizawa, Kinetic study of the hydration of magnesium oxide for a chemical heat pump, Applied Thermal Engineering 16 (1996) 853-862.

[121] M. Taheri, R.C. Phillips, J.R. Kish, G.A. Botton, Analysis of the surface film formed on Mg by exposure to water using a FIB cross-section and STEM-EDS, Corrosion Science 59 (2012) 222-228.

[122] M. Taheri, M. Danaie, J.R. Kisha, TEM examination of the film formed on corroding Mg prior to breakdown, Journal of The Electrochemical Society 161 (2014) C89-C94.

[123] Y. Ding, G. Zhang, H. Wu, B. Hai, L. Wang, Y. Qian, Nanoscale magnesium hydroxide and magnesium oxide powders: control over size, shape, and structure via hydrothermal synthesis, Chemistry of Materials 13 (2001) 435-440.

[124] M.S. Mastuli, N. Kamarulzaman, M.A. Nawawi, A.M. Mahat, R. Rusdi, N. Kamarudin, Growth mechanisms of MgO nanocrystals via a sol-gel synthesis using different complexing agents, Nanoscale Research Letters 9 (2014) 134-134.

[125] Y. Aly, V.K. Hoffman, M. Schoenitz, E.L. Dreizin, Reactive, mechanically alloyed Al · Mg powders with customized particle sizes and compositions, Journal of Propulsion and Power 30 (2014) 96-104.

[126] M.A. Machado, D.A. Rodriguez, Y. Aly, M. Schoenitz, E.L. Dreizin, E. Shafirovich, Nanocomposite and mechanically alloyed reactive materials as

energetic additives in chemical oxygen generators, Combustion and Flame (2014).

[127] H. Nie, S. Zhang, M. Schoenitz, E.L. Dreizin, Reaction interface between aluminum and water, International Journal of Hydrogen Energy 38 (2013) 11222-11232.

[128] S. Wang, A.L. Corcoran, E.L. Dreizin, Combustion of magnesium powders in products of an air/acetylene flame, Combustion and Flame 162 (2015) 1316-1325.

[129] P. Šimon, Isoconversional methods: Fundamentals, meaning and application, Journal of Thermal Analysis and Calorimetry 76 (2004) 123-132.

[130] A. Khawam, D.R. Flanagan, Role of isoconversional methods in varying activation energies of solid-state kinetics: II. Nonisothermal kinetic studies, Thermochimica Acta 436 (2005) 101-112.

[131] J.D. Peterson, S. Vyazovkin, C.A. Wight, Kinetics of the thermal and thermo-oxidative degradation of polystyrene, polyethylene and poly(propylene), Macromolecular Chemistry and Physics 202 (2001) 775-784.

[132] G.S. Cole, A.M. Sherman, Light weight materials for automotive applications, Materials Characterization 35 (1995) 3-9.

[133] S. Toros, F. Ozturk, I. Kacar, Review of warm forming of aluminum-magnesium alloys, Journal of Materials Processing Technology 207 (2008) 1-12.

[134] A. Züttel, Hydrogen storage methods, Naturwissenschaften 91 (2004) 157-172.

[135] T.A. Roberts, R.L. Burton, H. Krier, Ignition and combustion of aluminum-magnesium alloy particles in O2 at high pressures, Combustion and Flame 92.

[136] X.G. Wu, Q.L. Yan, X. Guo, X.F. Qi, X.J. Li, K.Q. Wang, Combustion efficiency and pyrochemical properties of micron-sized metal particles as the components of modified double-base propellant, Acta Astronautica 68 (2011) 1098-1112.

[137] E. Farbar, J. Louwers, T. Kaya, Investigation of metallized and nonmetallized hydroxyl terminated polybutadiene/hydrogen peroxide hybrid rockets, Journal of Propulsion and Power 23 (2007) 476-486.

[138] M.H. Zayan, O.M. Jamjoom, N.A. Razik, High-temperature oxidation of Al-Mg alloys, Oxidation of Metals 34 (1990) 323-333.

[139] P. Krizik, M. Balog, E. Illekova, P. Svec Sr, I. Matko, M. Stepanek, M. Nosko, F. Simancik, The oxidation behavior of gas-atomized Al and Al alloy powder green compacts during heating before hot extrusion and the suggested heating process, Journal of Materials Processing Technology 214 (2014) 1165-1172.

[140] C. Lea, J. Ball, The oxidation of rolled and heat treated Al-Mg alloys, Applications of Surface Science 17 (1984) 344-362.

[141] J.D. Moretti, J.J. Sabatini, G. Chen, Periodate salts as pyrotechnic oxidizers: development of barium- and perchlorate-free incendiary formulations, Angewandte Chemie, International Edition 51 (2012) 6981-6983.

[142] H. Habu, Application of magnalium to solid rocket propellant, Keikinzoku 58 (2008) 162-166.

[143] H. Habu, K. Hori, The burning rate characteristics of magnalium (Mg/Al)-AP based solid propellant, Science and Technology of Energetic Materials 67 (2006) 187-192.

[144] H. Murata, Y. Azuma, T. Tohara, M. Simoda, T. Yamaya, K. Hori, T. Saito, Effect of magnalium (Mg-Al alloy) on combustion characteristics of ammonium nitrate-based solid propellant, Kayaku Gakkaishi/Journal of the Japan Explosives Society 61 (2000) 58-66.

[145] M.N. De Noirfontaine, G. Baldinozzi, M.G. Barthés-Labrousse, J. Kusinski, G. Boëmare, M. Herinx, M. Feuerbacher, High temperature oxidation of the Al 3Mg 2 complex metallic alloy, Oxidation of Metals 73 (2010) 219-232.

[146] H. Nie, M. Schoenitz, E.L. Dreizin, Oxidation of magnesium: implication for aging and ignition, Journal of Physical Chemistry C 120 (2016) 974-983.

[147] Y. Aly, V.K. Hoffman, M. Schoenitz, E.L. Dreizin, Preparation, ignition, and combustion of mechanically alloyed Al-Mg powders with customized particle sizes, Materials Research Society Symposium Proceedings, 2013, pp. 43-48.

[148] F. Tepper, Electro-explosion of wire produces nanosize metals, Metal Powder Report 53 (1998) 31-33.

[149] F. Tepper, Metallic nanopowders produced by the electro-exploding wire process, International Journal of Powder Metallurgy (Princeton, New Jersey) 35 (1999) 39-44.

[150] W. Jiang, K. Yatsui, Pulsed wire discharge for Nanosize powder synthesis, IEEE Transitions on Plasma Science 26 (1998) 1498-1501.

[151] R.A. Yetter, G.A. Risha, S.F. Son, Metal particle combustion and nanotechnology, Proceedings of the Combustion Institute 32 II (2009) 1819-1838.

[152] E.L. Dreizin, Metal-based reactive nanomaterials, Progress in Energy and Combustion Science 35 (2009) 141-167.

[153] A. Gromov, L.T. DeLuca, A.P. Il'in, U. Teipel, A. Petrova, D. Prokopiev, Nanometals in energetic systems: achievements and future, International Journal of Energetic Materials and Chemical Propulsion 13 (2014) 399-419.

[154] L. Meda, G. Marra, L. Galfetti, F. Severini, L. De Luca, Nano-aluminum as energetic material for rocket propellants, Materials Science and Engineering C 27 (2007) 1393-1396.

[155] K.T. Higa, Energetic nanocomposite lead-free electric primers, Journal of Propulsion and Power 23 (2007) 722-727.

[156] A.N. Pivkina, Y.V. Frolov, D.A. Ivanov, Nanosized components of energetic systems: structure, thermal behavior, and combustion, Combustion, Explosion and Shock Waves 43 (2007) 51-55.

[157] B.J. Henz, T. Hawa, M.R. Zachariah, Atomistic simulation of the aluminum nanoparticle oxidation mechanism, AIAA Conference, Orlando, FL, 2010.

[158] A. Rai, D. Lee, K. Park, M.R. Zachariah, Importance of phase change of aluminum in oxidation of aluminum nanoparticles, Journal of Physical Chemistry B 108 (2004) 14793-14795.

[159] A. Rai, K. Park, L. Zhou, M.R. Zachariah, Understanding the mechanism of aluminium nanoparticle oxidation, Combustion Theory and Modelling 10 (2006) 843-859.

[160] B. Rufino, F. Boulc'h, M.V. Coulet, G. Lacroix, R. Denoyel, Influence of particles size on thermal properties of aluminium powder, Acta Materialia 55 (2007) 2815-2827.

[161] P. Puri, V. Yang, Effect of particle size on melting of aluminum at nano scales, Journal of Physical Chemistry C 111 (2007) 11776-11783.

[162] X. Zhu, M. Schoenitz, E.L. Dreizin, Oxidation of aluminum particles in mixed CO2/H2O atmospheres, Journal of Physical Chemistry C 114 (2010) 18925-18930.

[163] H. Nie, M. Schoenitz, E.L. Dreizin, Initial stages of oxidation of aluminum powder in oxygen Journal of Thermal Analysis and Calorimetry, in press (2016).

[164] S. Vyazovkin, Model-free kinetics: Staying free of multiplying entities without necessity, Journal of Thermal Analysis and Calorimetry 83 (2006) 45-51.

[165] F. Reichel, L.P.H. Jeurgens, G. Richter, E.J. Mittemeijer, Amorphous versus crystalline state for ultrathin Al2O3 overgrowths on Al substrates, Journal of Applied Physics 103 (2008) 093515/093511-093515/093510.

[166] L.P.H. Jeurgens, W.G. Sloof, F.D. Tichelaar, E.J. Mittemeijer, Growth kinetics and mechanisms of aluminum-oxide films formed by thermal oxidation of aluminum, Journal of Applied Physics 92 (2002) 1649.

[167] B. Rufino, M.V. Coulet, R. Bouchet, O. Isnard, R. Denoyel, Structural changes and thermal properties of aluminium micro- and nano-powders, Acta Materialia 58 (2010) 4224-4232.